

**DIGITAL IMAGE PROCESSING OF SATELLITE DATA
FOR STRUCTURAL MAPPING
IN SINGRAULI COALFIELD, INDIA**

A Thesis Submitted
in Partial Fulfilment of the Requirements
for the Degree of

DOCTOR OF PHILOSOPHY

by

NITIN KUMAR TRIPATHI

to the
**DEPARTMENT OF CIVIL ENGINEERING
INDIAN INSTITUTE OF TECHNOLOGY KANPUR**
April, 1994

CERTIFICATE

15/4/94

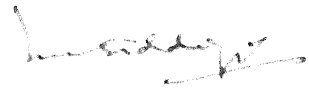
It is certified that the work contained in the thesis entitled "**Digital Image Processing of Satellite Data for Structural Mapping in Singrauli Coalfield, India**" by **Nitin Kumar Tripathi**, has been carried out under our supervision and that this work has not been submitted elsewhere for a degree.

April¹⁵, 1994



Dr. K. V. G. K. Gokhale
Professor

Department. of Civil Engineering
Indian Institute of Technology
Kanpur, India



Dr. M. U. Siddiqui
Professor

Department of Electrical Engineering
Indian Institute of Technology
Kanpur, India

22 JUL 1996
CENTRAL LIBRARY
I. I. T., KANPUR

Inv. No. A. 121906

121906



A121906

CE-1994-D-TRI-DIG

To my
Parents,
Akash, Susmit
and
Archana

SYNOPSIS

Name of student : Nitin Kumar Tripathi Roll No. : 8920362
Degree for which : Ph.D. Department : Civil Engineering
submitted
Thesis Title : Digital Image Processing of Satellite Data for Structural
Mapping in Singrauli Coalfield, India
Thesis supervisors : Prof. K.V.G.K. Gokhale and Prof. M.U. Siddiqui
Month and year : April, 1994
of submission

Structural features in a coalfield play an important role in the location of coal seams. In India, with the recent emphasis on power generation through thermal power plants, coalfields have been the centres of intense activity. Singrauli coalfield is taken as a case study as it has the unique distinction of having the thickest coal seam in India. This region has five super thermal power stations which act as nuclei for industrial development. The present work deals with digital image processing techniques for extracting the structural features in the coalfield. In addition to several image processing techniques involving image smoothing, filtering and edge linking, a relatively new concept of image transformation based on mathematical morphology has also been detailed. A comparison of the performance of these techniques has been attempted and a final scheme of image processing for lineament detection is proposed. Results obtained have indicated a distinct improvement

over the available published work on the structural details within this coalfield. The methodology and the sequence of operations proposed are applicable to other coalfields as well. The softwares used at different stages of work have been developed by the author during the course of this study.

The work contained in the thesis has been organized into seven chapters.

In Chapter 1, the topic has been introduced and an overview of the geology of the Singrauli coalfield is presented. The scope of the present work has also been indicated. In the north-eastern part of the coalfield taken up for study, the boundary between Lower Gondwana formations and the Precambrian metamorphic rocks is faulted. The Gondwana sequence is composed of the basal Talchir Formations (Lower Permian) followed by the Barakars, Barren Measures and Raniganj Formations. The formations are essentially sandstones and shales. Coal seams in the area are associated with the Barakar and the Raniganj Formations. Several faults and lineaments are present in all these formations. Geological details along with the field features of all these formations are presented in this chapter.

Description of data used and details of the preprocessing techniques adopted are presented in Chapter 2. Remotely sensed data from two different satellites (IRS 1B-LISS II and LANDSAT-TM) have been used. Preprocessing of satellite data has been carried out to establish compatibility as the spatial resolution, sensing geometry and system configuration differ. To reduce the problem associated with dimensionality of data, the information distributed in number of bands has been compressed into fewer number of components using Karhunen-Loeve transformation. A base map of the study area is prepared using the satellite data as well as the available geological maps.

Using the preprocessed IRS data, two false colour composites (FCC) have been prepared with combinations of bands 1 to 4. On the basis of these composites, the

lithological demarcation is carried out. Geomorphic features of the area are mapped on the basis of a FCC prepared using the principal components computed earlier (Chapter 2). A land use / land cover map of the study area has also been prepared which has brought out clearly the environmental impact of open cast coal mining. The details of all these aspects are presented in Chapter 3.

Chapter 4 deals with digital enhancement of structural features. Image smoothing techniques have been applied to reduce noise in the satellite imagery. It has been realized that pseudomedian filtering offered desirable results. Edge enhancement has been carried out using derivative filtering of the first and second order, in addition to the entropy based filtering. Under the first order derivative filtering, orthogonal and directional filtering are employed while Laplacian filtering is adopted under the second order filtering. Of all the operators used for edge detection, Frei-Chen operator of the orthogonal derivative filtering has yielded best results. This image is thresholded and the output image is processed using edge linking operation to render the final edge image.

In Chapter 5, an edge detection approach based on mathematical morphology is discussed. Image smoothing using neighborhood criterion has been performed for noise suppression. Transformations developed are dedicated to edge detection and involve the fundamental morphological operations such as dilation, erosion, opening and closing. Top hat transformations are developed based on opening, closing and image differencing to enhance the edges in various directions. In the present work, it is seen that the top hat transformation used along with image superimposition technique provides a better edge image for the interpretation of lineaments. In the above transformations, several structuring elements of different shapes and sizes have been tested and the one yielding best result has been chosen.

Chapter 6 deals with the lineament mapping and analysis. Based on the image

processing tools employed (Chapter 4 and 5) two lineament detection schemes - designated in the present work as *Digitedge* and *Morphedge Schemes* are utilized in preparing the lineament map. A statistical study of the characteristics of the lineaments has also been undertaken. The statistical analysis of lineaments involved tests for randomness, trend and specific orientation. Based on the qualitative and statistical analysis, the *Morphedge Scheme* is considered more appropriate for lineament mapping compared to the *Digitedge Scheme*. For delineation of faults, a scheme based on the morphological transformations has yielded encouraging results. Structural map of the area has been prepared using output obtained from this scheme. Several faults and lineaments not reported earlier could be delineated which were confirmed through limited field checks.

Chapter 7 contains an overall summary of the present work. Based on the results obtained, suitability of various image processing techniques for structural mapping has been discussed.

ACKNOWLEDGEMENT

I express my profound sense of gratitude and reverence to Prof. K. V. G. K. Gokhale and Prof. M. U. Siddiqui for their prudent guidance and incessant encouragement. During the course of research they always provided me their fullest cooperation and guided me on the right path to achieve the objective.

I wish my sincerest gratitude to my colleague Dr. Onkar Dikshit for his valuable suggestions and everhelping attitude. I express my sincerest regards to my colleagues of Dept. of Civil Engineering for their kind assistance and good wishes for successful completion of this research work.

I am thankful to Sri G. P. Mishra for his cooperative attitude. I am also thankful to Sri Ramkishan for his services.

The active and untiring support rendered by Sri Anand Sirohi and Sri Praveen Dwivedi during the course of preparation of this manuscript is gratefully acknowledged.

I express my heartfelt thanks to Sri R. Venugopal for his timely help.

The cooperation extended by the staff of Central Mining Planning and Design Institute, Jayant, M.P. during my field visit for this work is acknowledged.

This work could not have been completed without the blessings of my parents and good wishes of my family members. I feel words can not express my real feelings of gratitude towards them.

Nitin Kumar Tripathi

CONTENTS

SYNOPSIS

LIST OF TABLES

LIST OF FIGURES

LIST OF SYMBOLS

CHAPTER	PAGE NO.
1. INTRODUCTION	1
1.1 General	1
1.2 Singrauli Coal Basin - An Overview	2
1.3 Scope and Objectives of the Present Study	15
1.4 Organization of the Work	16
2. PREPROCESSING OF DATA	18
2.1 Introduction	18
2.2 Data Acquisition	18
2.3 Data Retrieval from CCT	23
2.4 Preprocessing of Satellite Digital Data	25
2.4.1 Geometric rectification	29
2.4.2 Image resampling	31
2.5 Data Compression	33
3. GEOLOGICAL AND LAND USE MAPPING USING SATELLITE DATA	42
3.1 Introduction	42
3.2 Lithological and Structural Mapping	42
3.3 Geomorphological Mapping	45
3.4 Land Use Mapping	48
4. DIGITAL ENHANCEMENT OF LINEAMENTS	56
4.1 Introduction	55
4.2 Image Smoothing	56

4.2.1	Moving average filtering	57
4.2.2	Sigma filtering	58
4.2.3	Median filtering	62
4.2.4	Pseudomedian filtering	69
4.3	Edge Detection	76
4.3.1	Derivative filtering	78
4.3.2	Edge detection based on image entropy	100
4.4	Edge Linking	104
4.5	Results and Discussion	107

5. MORPHOLOGICAL IMAGE TRANSFORMATIONS FOR ENHANCEMENT OF LINEAMENTS

5.1	Introduction	110
5.2	Mathematical Morphology	111
5.3	Greyscale Morphological Image Processing	116
5.3.1	Dilation	118
5.3.2	Erosion	119
5.3.3	Opening	119
5.3.4	Closing	119
5.4	Morphological Image Smoothing	120
5.4.1	Morphological image smoothing using erosion	120
5.4.2	Morphological image smoothing using neighbourhood criterion	121
5.5	Morphological Edge Detection	122
5.5.1	Edge detection using different structural elements	122
5.5.2	Edge detection using top hat transformation	125
5.5.3	Edge detection using top hat transformation and image superimposition	130
5.6	Results and Discussion	140

6. LINEAMENT MAPPING AND ANALYSIS 142

6.1	Introduction	142
6.2	Lineament Mapping	142
6.3	Lineament Analysis	146
6.4	Geological Map from Digitally Processed Satellite Data	158
6.5	Accuracy Estimation of the Geostructural Map	161

7. SUMMARY AND CONCLUSION	163
REFERENCES	167
BIBLIOGRAPHY	173
APPENDIX - A	178

LIST OF FIGURES

No.	Title	Page No.
1.1	Location of major coalfields of India	3
1.2	Geological map of N-E Singrauli coalfield	5
1.3	Pegmatite in gneissic terrain (5 km north of Morwa)	6
1.4	Disturbances in brecciated gneiss in the fault zone	6
1.5	Steeple dipping phyllites near Khirba	7
1.6	Disturbed trends in foliations of phyllites in the faulted zones	7
1.7 (a)	Pebble horizon in Talchir sandstone near Dheki	9
1.7 (b)	Pebbles in Talchir diamictite horizon near Jaitpur	9
1.8	Loosely cemented Barakar sandstones near Jayant block	11
1.9	Barakar sandstones with ferruginous cement (2 km north of Singrauli)	11
1.10	Barakar sandstones exhibiting slumping of beds and cross bedding near Dudhichua	12
1.11	Gray arenaceous shales overlying Barakar sandstone near Khadia	12
1.12	Coal seam underlying Barakar sandstone in Dhudhichua mines	13
1.13	Formation of jhama due to burning of coal (Dhudhichua)	13
1.14	Fine grained compact Raniganj sandstone with underlying coal seam (Jingurdah Mines)	14
2.1	Layout of user CCT of BIL format	24
2.2	IRS-1B LISS-II image of the study area, Band 1	26
2.3	IRS-1B LISS-II image of the study area, Band 2	26
2.4	IRS-1B LISS-II image of the study area, Band 3	27
2.5	IRS-1B LISS-II image of the study area, Band 4	27
2.6	LANDSAT-TM image of the study area, Band 7	28
2.7	Nearest neighbourhood process for resampling	32
2.8	Geometrically corrected and registered LANDSAT-TM image of the study area	34
2.9	Graphic illustration of data transformation using Principal Component Analysis	36
2.10	Principal Component-1 image of the study area	41
2.11	Principal Component-4 image of the study area	41
3.1	False colour composite of IRS (Band 1, 3, and 4)	43
3.2	False colour composite of IRS (Band 1, 2, and 4)	44

3.3.	Lithological and fault demarcation based on false colour composites and LANDSAT-TM image of Band-7	46
3.4	FCC generated using principal component 1, 2 and 4	47
3.5	Geomorphological map of the study area prepared from false colour composite generated using principal components	49
3.6	Structural ridges in slates and phyllites near Khirba	50
3.7	Structural ridges in gneissic terrain near Bijul river (North of Singrauli)	50
3.8	Typical pediplain in the Barakar terrain near Merhauili	51
3.9	A typical mesa in Barakar terrain near Nigahi	51
3.10	Butte in Barakar terrain near Shaktinagar	52
3.11	Land use map of the study area prepared from FCC generated using principal components (Fig. 3.4)	53
3.12	A mine dump in the Jayant block	54
3.13	Ballia nala polluted with mine drainage prior to its confluence with G. B. Pant reservoir	54
4.1	(a) Edge plus noise signal (b) After median filtering (c) After moving average filtering	64
4.2	Configuration of filter windows for median filtering	66
4.3	Moving average and median filtering on various test signals	68
4.4	Various window configurations utilized in performing pseudomedian filtering	72
4.5	Original test region (a) and its smoothened output for moving average filtering (b); sigma filtering (c); median filtering (d) and pseudomedian filtering (e)	73
4.6	Smoothened image using a 3x3 plus shaped pseudomedian filtering	75
4.7	One-dimensional ideal and real edge signals	77
4.8	Flow diagram of derivative filtering for edge detection	81
4.9	Impulse response operators used in orthogonal derivative gradient edge detection	85
4.10	Edge detection output using first order orthogonal derivative filtering on an image subregion of the area	87
4.11	Edge detection using orthogonal derivative filtering by Frei-Chen operator	88
4.12	Directional gradient templates for Prewitt compass gradient method	92
4.13	Directional gradient templates for Kirsch gradient method	93
4.14	Directional gradient templates for Robinson 3-level gradient method	94

4.15	Directional gradient templates for Robinson 5-level gradient method	95
4.16	Edge detected image using Kirsch gradient	96
4.17	Edge detected image using Robinson 5-level directional filtering	96
4.18	Edge detected image using Laplacian eight neighbour	103
4.19	Edge detection using non-linear entropy 3x3 operator	103
4.20	Edge detected image after edge linking (Frei-Chen image is used for edge linking)	106
5.1	An illustration of basic morphological operations	114
5.2	Illustration of the concept of homotopy in morphological image algebra	117
5.3	Morphological image smoothing of IRS Band 3 image of study area	123
5.4	Structuring elements for edge detection	126
5.5	Edge image using morphological edge detection (using DILATION operation)	127
5.6	Edge image using morphological edge detection (using EROSION operation)	127
5.7	(a) OPEN operation on one-dimensional signal, (b) CLOSE operation on one-dimensional signal, (c) Difference($f - f^B$), (d) Difference ($f - f^B$)	129
5.8	Hexagonal structuring elements chosen for directional top hat transform	132
5.9	Top hat transformation at 60° using hexagonal structuring element	133
5.10	Top hat transformation at 120° using hexagonal structuring element	133
5.11	Top hat transformation at 30° using hexagonal structuring element	134
5.12	Top hat transformation at 90° using hexagonal structuring element	134
5.13	Top hat transformation at 150° using hexagonal structuring element	135
5.14	Edge image using top hat transformation and image superimposition	136
5.15	Structural elements used for top hat transformation and image superimposition	137
5.16	Top hat transformation and image superimposition using 3x3 plus structuring element	138
5.17	Top hat transformation and image superimposition using 3x3 45° structuring element	139
5.18	Top hat transformation and image superimposition using 3x3 135° structuring element	139
6.1	Digitedge scheme for lineament enhancement and mapping	144
6.2	Lineament map of study area prepared using Digitedge Scheme	145
6.3	Morphedge scheme for lineament enhancement and mapping	147

6.4	Lineament map of study area prepared using Morphedge Scheme	148
6.5	Various zones demarcated based on visual interpretation for further analysis of lineaments	149
6.6	Lineament density in various zones using Morphedge and Digitedge scheme	153
6.7	Image processing scheme to map structural features	159
6.8	Geostructural details of the study area using morphologically processed satellite images	160

LIST OF TABLES

No.	Title	Page No.
1.1	Geological sequence of the Singrauli basin	8
2.1	LANDSAT-TM spectral bands and principal applications	20
2.2	IRS spectral bands and principal applications	21
2.3	SPOT-MI.A spectral bands and principal applications	22
2.4	Ground control points selected from LANDSAT-TM and IRS-1B image of the study area	30
2.5	Coefficient of quadratic mapping for geometric correction	31
2.6	Variance-Covariance matrix and Correlation matrix of original dataset	39
2.7	Percentage variance,eigen values,eigen vectors and factor loadings of the dataset	40
4.1	Results of image smoothing techniques on a selected region of the image	107
4.2	Results of edge detection techniques on a selected region of the image	109
6.1	Statistical parameters for lineament analysis (Morphedge scheme)	151
6.2	Statistical parameters for lineament analysis (Digitedge scheme)	151
6.3	Critical orientation interval encomposing lineament directions	155
6.40	Estimation of accuracy of the final geostructural map	162

LIST OF SYMBOLS

$f(x, y)$	Digital two-dimensional image
\mathcal{Z}	Set of integers
\mathcal{R}	Set of real numbers
$i \in \mathcal{Z}$	i is a member of \mathcal{Z}
B	Binary structuring element
X, A	Binary image (set of points)
a	Grey level image
X_B	X opened with B
X^B	X closed with B
Φ	Null set
\subset	Subset
$A \cup B$	Set union
$A \cap B$	Set intersection
$\Psi(x)$	Morphological transformation
$A \oplus B$	Set addition of A and B
$A \ominus B$	Set subtraction of B from A
\mathcal{T}	Transformation
T	Threshold
\odot	Convolution

Chapter 1

INTRODUCTION

1.1 General

Among the three means of power generation, namely : the nuclear, hydro and thermal, in India the emphasis has largely been placed, of late, on the thermal power generation. In this context, Singrauli coalfield has gained prominence and presently occupies unique place in the coal map of India. It has the unique distinction of having the thickest coal seam known as the Jingurdah seam with a thickness of 132 m. Coal is mined through open cast mining and the production is substantial (around 30 MT). This basin has also the unique distinction of having five Super Thermal Power Stations and a host of industrial establishments being located with these power plants as the nuclei. Thus, the entire scenario in regard to the economic development of this region in India has gone through a sea change. In the last three decades geological mapping has been in progress and extensive drilling has enabled the delineation of several coal seams including the Jingurdah coal seam. For detailed exploration, this coal field was divided into eleven mining blocks and over the years, assistance from international agencies has also been availed for developing the coal mines. While conventional geological mapping and drilling have been the tools for the exploration, enough scope exists to examine the region using satellite data. Till date, except for scattered reports on visual interpretation of imagery, no work has been reported dealing with the digital analysis of satellite data for this coalfield. The study of remote sensing data facilitates an understanding of the regional picture. With the application of proper digital image processing techniques, the geological and structural details can be selectively enhanced. With this idea in view the

present work was undertaken. Satellite data as obtained through IRS-1B (LISS-II) and LANDSAT-TM pertaining to the year 1992 has been processed in the present work. The relevant software involved in the image processing and enhancement at different stages has been developed by the author.

1.2 Singrauli Coal Basin - An Overview

The Gondwana coal basins in Peninsular India occur as isolated intracontinental rift basins in the Precambrian terrain. These basins are irregular, elongate and oval with differing dimensions. They bear several similarities. Cyclic disposition in these basins is very characteristic. During deposition, basin subsidence has been the general feature. The basins are marked by prominent high angle normal faults that limit their boundaries (Basu and Srivastava, 1980). In Peninsular India, these basins occur along two preferred orientations namely EW and SE-NW (Fig. 1.1). Singrauli coal basin is an important member of this group.

The basin has an area of 2200 sq. km of which approximately 4 percent is located in Sonbhadra district of U.P. with the rest extending into Sidhi and Sahdol districts of M.P. The basin is divided into two sub-basins, known as the Moher sub-basin in the East and the Main sub-basin in the West, the dividing line approximately conforming to the longitude $82^{\circ} 30' \text{ E}$. In the Moher sub-basin, mining is in progress in the NE part. The coal field stands out as a prominent plateau in contrast to the adjacent plains. The coal field is well connected through transportation network with several places as Satna (307 km) in M.P. as well as with Pipri (40 km) , Renukoot (50 km), Mirzapur (193 km) and Varanasi (210 km) in U. P. It has railway links with Mirzapur and Katni. The climate is of tropical monsoon type with severe winter and extreme summer temperatures. Annual rainfall varies between 130 and 150 cm.

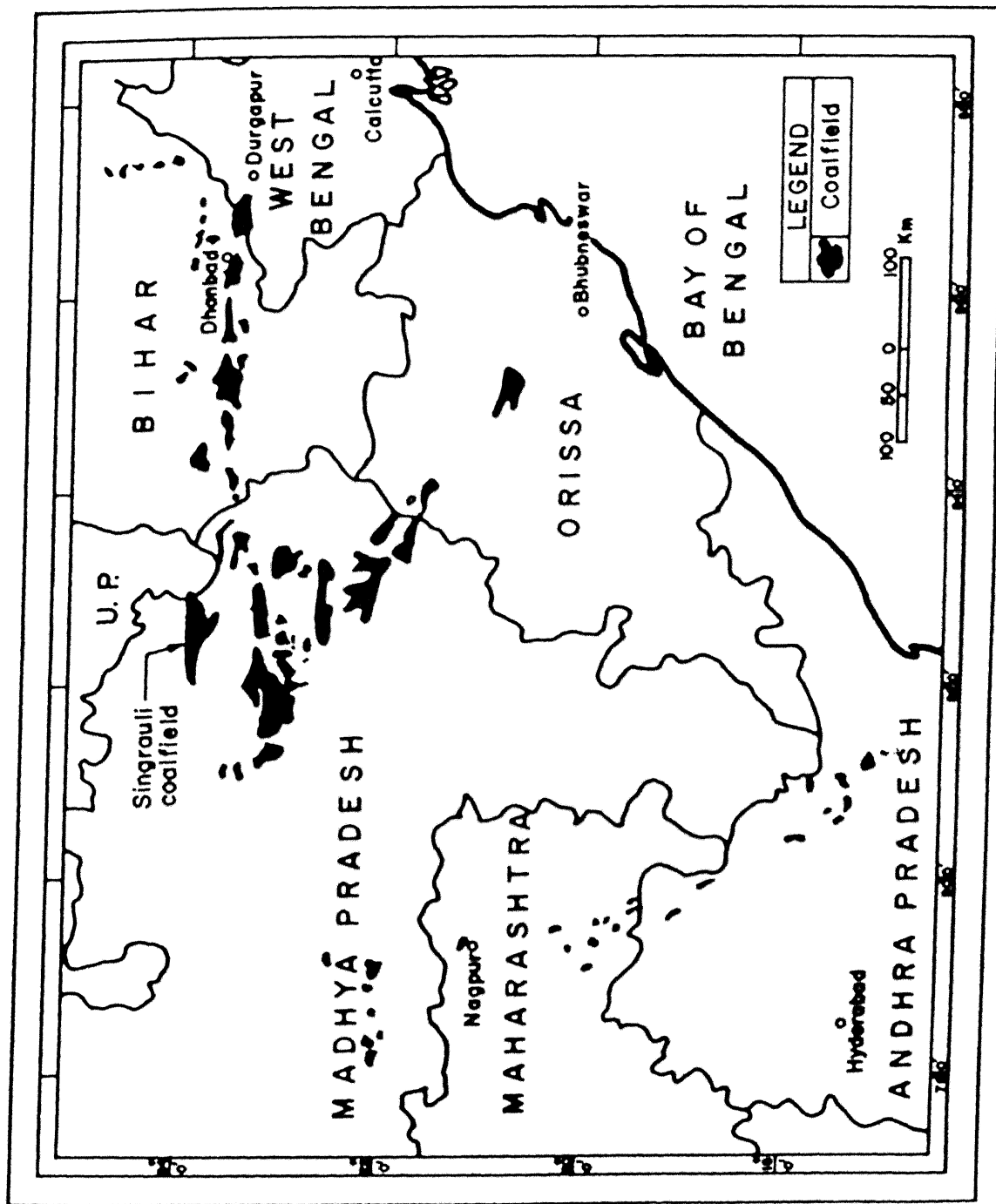


Fig. I.1: Location of major Coalfields of India (Source: CMPDI, 1984)

Geology of the study area

As indicated in Fig. 1.2, the NE part of the basin is chosen as the study area. The sequence within the coal field in this region is essentially of Lower Gondwana (Upper Carboniferous - Permian) formations. An EW trending fault located in the northern part of the area limits the extension of these formations and marks the boundary with the Precambrian metamorphic rocks. The Precambrian formations are composed of gneisses, slates and phyllites.

Within the gneissic terrain, patches of granite and pegmatite (Fig. 1.3) are also evidenced. In the area adjacent to the Bijul river (north of Singrauli Railway station), disturbance in the foliation has been evidenced (Fig. 1.4). In the vicinity of the boundary, the metamorphics outcrop in a series of parallel and elongate ridges. The general trend of foliation is along $N 85^{\circ}$ with high dip angles towards South (Fig. 1.5). Within the slates and phyllites, faulting has resulted in the dislocation of foliation trends and crushing of the rocks (Fig. 1.6).

The generalized sequence (after Joshi and Pant, 1971) of the lower Gondwana formations in the study area is indicated in Table 1.1. Continued subsidence of the sediments along the boundary fault appears to have increased the tilt which has resulted in these formations dipping towards the fault. Accumulation of greater thickness of sediments close to the boundary faults in the Gondwana basins has been attributed to subsidence (Basu and Srivastava, 1980).

LEGEND

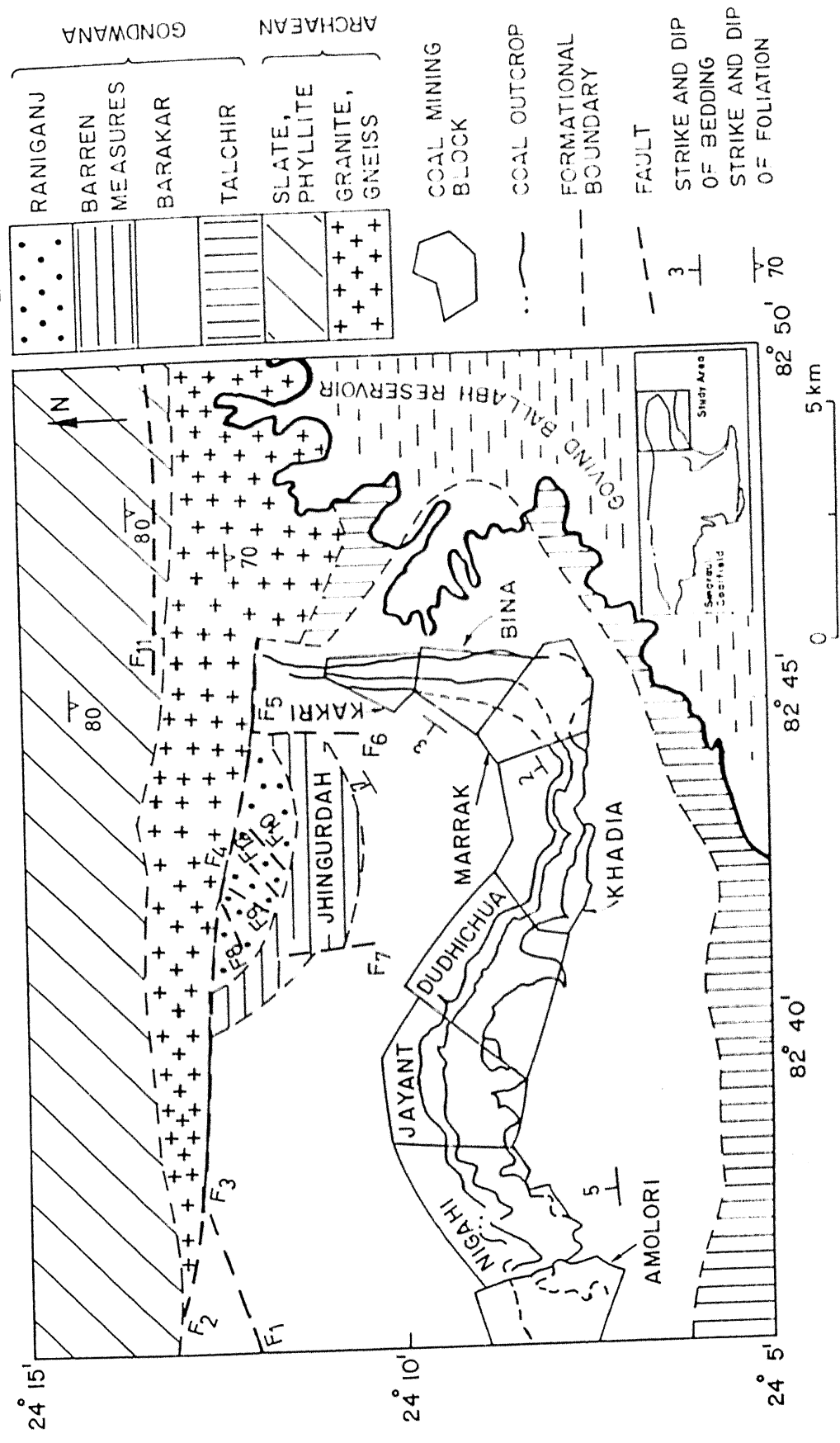


Fig.1.2: Geological map of N-E Singrauli Coalfield (Source: Sinha, et al., 1982)



Fig. 1.3 Pegmatite in gneissic terrain (5 km north of Morwa).

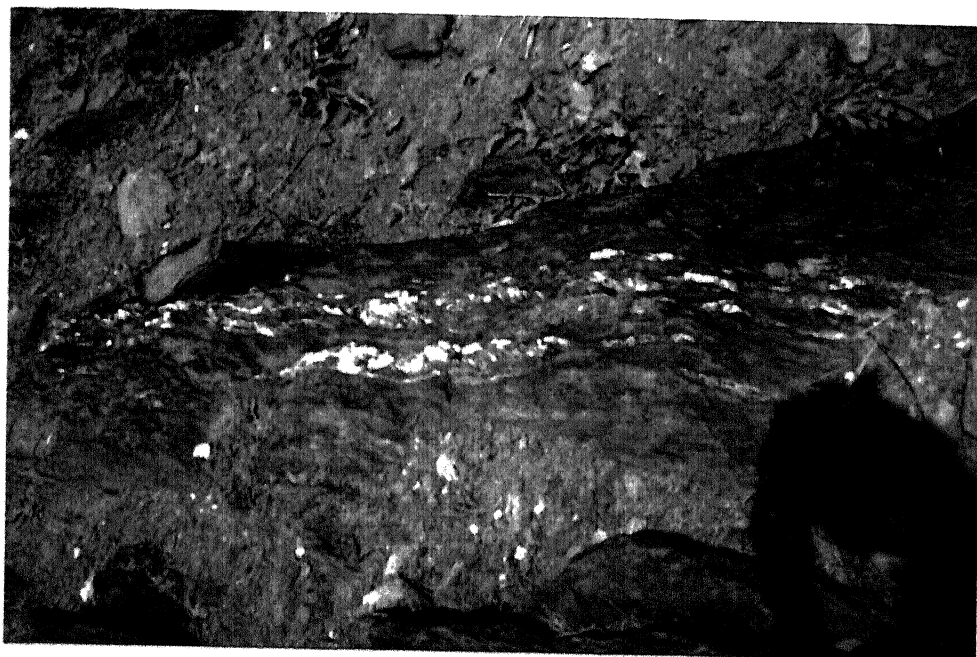


Fig. 1.4 Brecciated gneiss in the fault zone.



Fig. 1.5 Steeply dipping phyllites near Khirba.

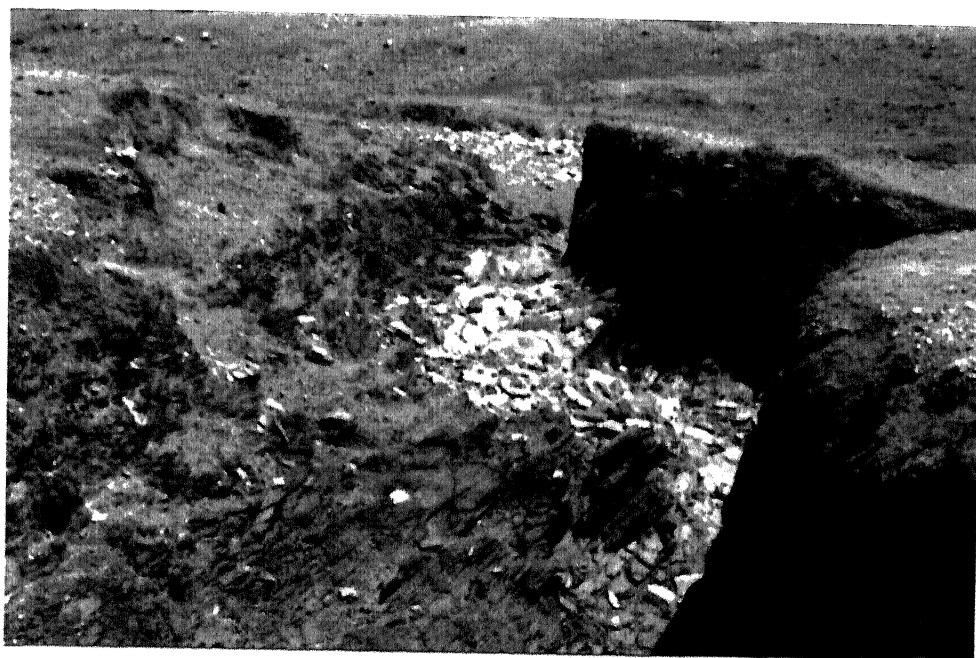


Fig. 1.6 Disturbed trends in foliations of phyllites in the faulted zones.

Table 1.1 : Geological sequence of the Singrauli basin (after Joshi and Pant, 1971)

Age	Formation	Lithology	Thickness (m)
Permian	Raniganj	Sandstone, Shale and Coal Seams	380
	Barren Measures	Coarse Sandstone	
		Purewa Top Seam	8-12
		Sandstone	0-60
	Barakar	Purewa Bottom Seam	10-14
		Sandstone and Shale	45-75
		Kota Seams	1-3
Upper Carboniferous	Talchir	Sandstone and Shale	150-250
		Shale and Sandstone	not proved

Talchir formations

These are exposed mostly in the eastern and the south-eastern part of the study area. The Talchir sequence has a basal diamictite horizon composed of striated pebbles of sandstone, jasper, gneisses and basic rocks (Murthy, 1957). The pebbles are of varying sizes and, at places boulders with striations indicating the glacial origin have also been reported (Pant and Shome, 1963). A thin horizon of diamictite evidenced in the southern part of the study area has elongated and rounded pebbles of differing sizes (Fig. 1.7). The Talchir sandstone is cross-bedded with current directions to NW (Raja Rao, 1983). The slate horizon in Talchir sequence is very thin.

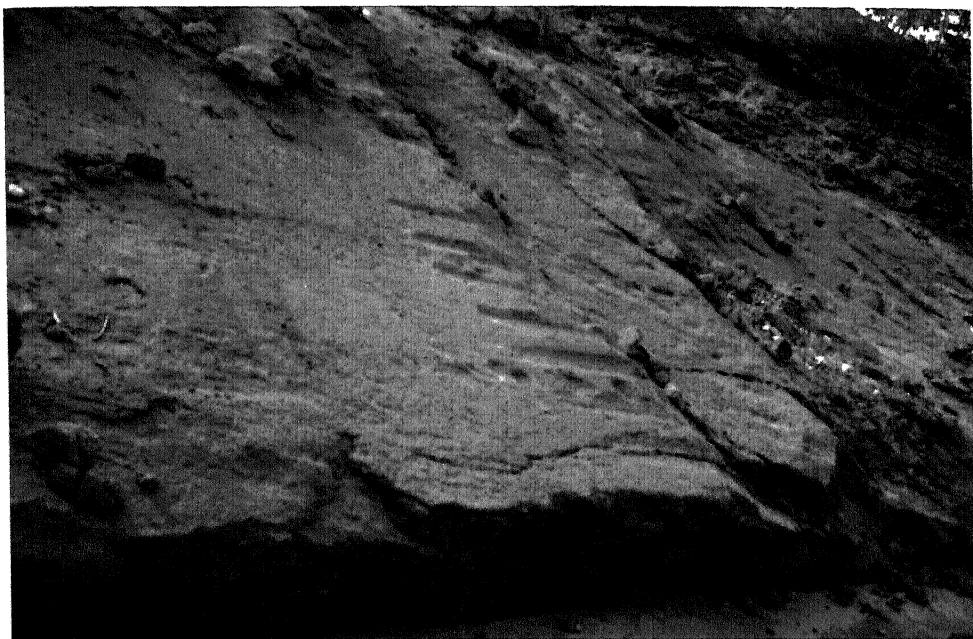


Fig. 1.7(a) Pebble horizon in Talchir sandstone near Dheki.



Fig. 1.7(b) Pebbles in Talchir diamictite horizon near Jaitpur.

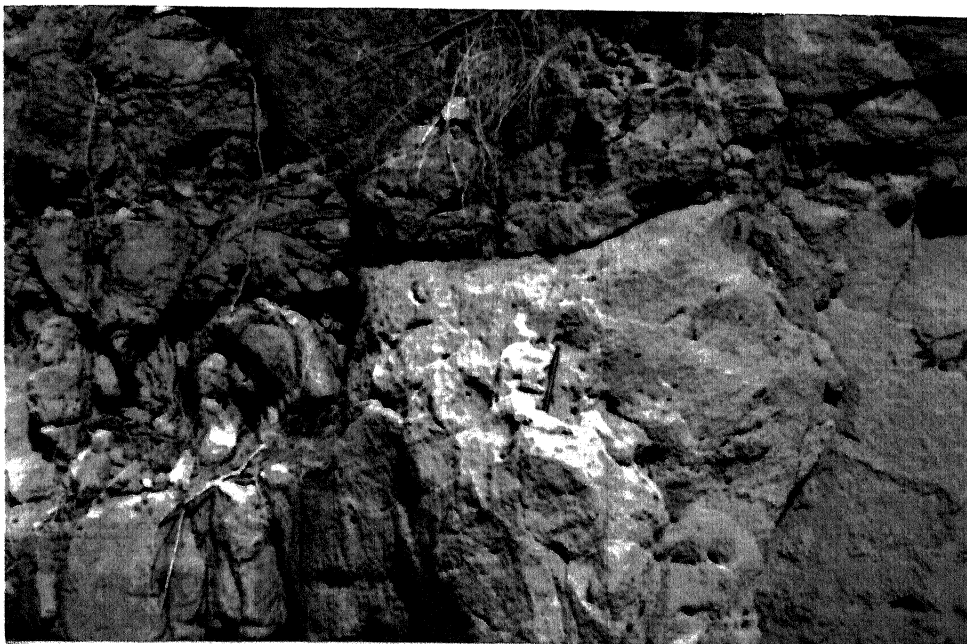


Fig. 1.8 Loosely cemented Barakar sandstones near Jayant block.

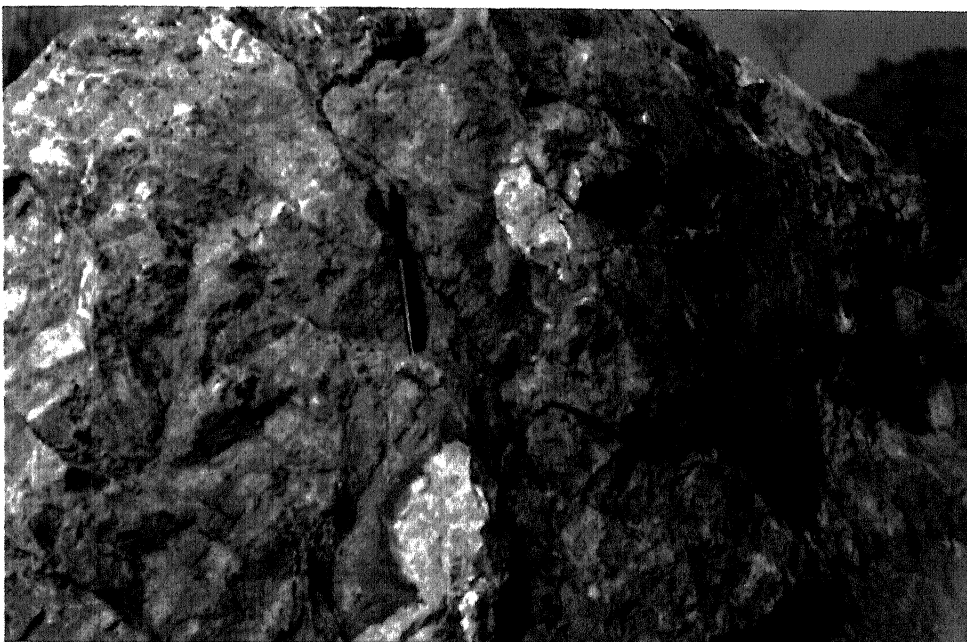


Fig. 1.9 Barakar sandstones with ferruginous cement (2 km north of Singrauli).

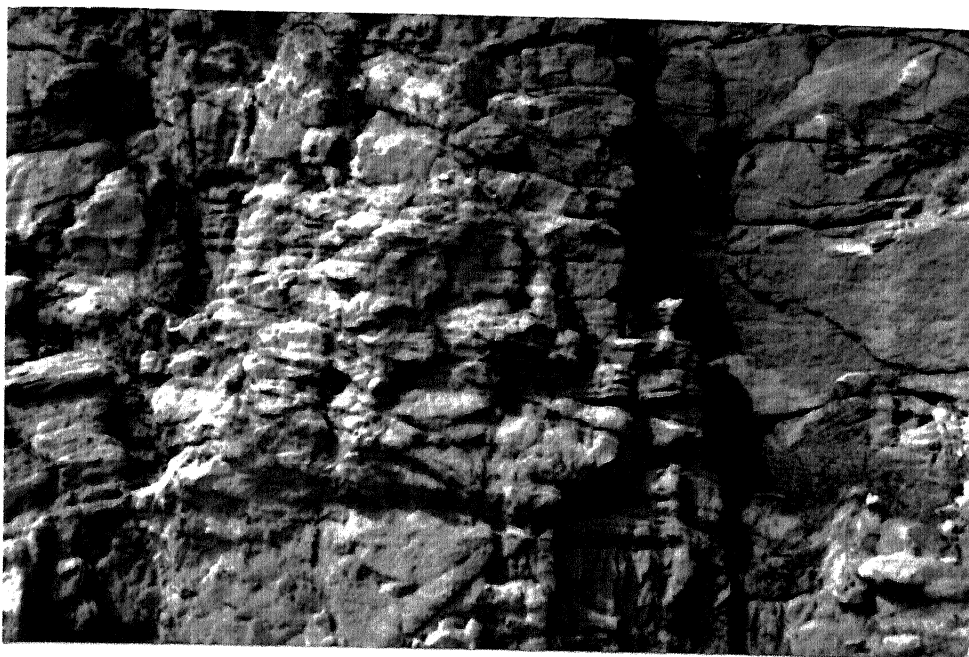


Fig. 1.10 Sandstones exhibiting slumping of beds and cross – bedding near Dudhichua.



Fig. 1.11 Gray arenaceous shales overlying Barakar sandstones near Khadia.

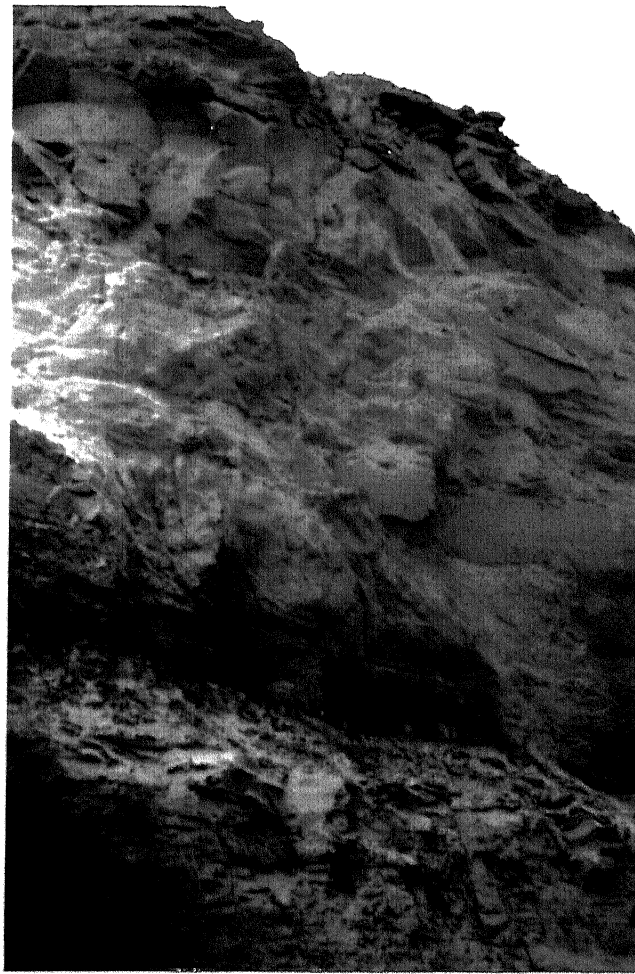


Fig. 1.12 Coal seam underlying Barakar sandstones in Dudhichua mines.

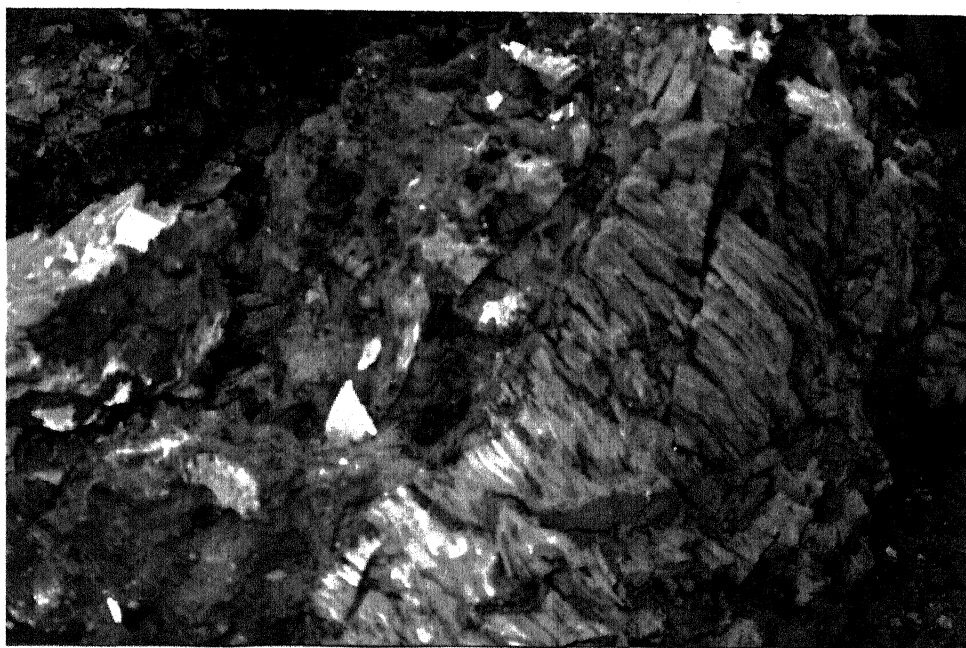


Fig. 1.13 Formation of jhama due to burning of coal (Dudhichua).

Raniganj formations

In the Jingurdah area, these formations have an arcuate disposition and attain a maximum thickness of 400 m as reported by earlier workers. The sequence essentially is of sandstones associated with clays and carbonaceous shale. The sandstone, in general, is fine grained and has a massive appearance (Fig. 1.14).

In the Jingurdah area, two coal seams occur within the Raniganj formations. The Lower seam, known as the Jingurdah bottom seam is reported to be of thickness upto 15 m while the upper seam designated as the Jingurdah top seam has a thickness of the order of 135 m. This is the single thickest coal seam reported so far in the coalfields of peninsular India. These two coal seams have a semi-elliptical garland shape and are offset by several cross cutting radial faults.



Fig. 1.14 Fine grained comapct Raniganj sandstone with underlying coal seam (Jingurdah Mines).

For the development of the coal in the area, the Singrauli coal field has been divided into eleven mining blocks - designated as the Jingurdah, Gorbi, Kakri, Bina, Marrak, Khadia, Dudhichua, Jayant, Nigahi, Amlohri and Moher blocks. The reserves of coal in this coalfield are reported to be around 10851 MT (CMPDI, 1984). The present study area encompasses nine out of these eleven blocks with the exclusion of Gorbi and Moher blocks.

1.3 Scope and Objectives of the Present Study

As already indicated, no published reports are available dealing with digital processing of satellite data for this coal basin. The study area offers excellent scope for investigations in this direction. The area exhibits distinct geomorphological features. The coal field area occurs as a plateau with scarp faces extending to the south of the area reflecting different stages of peneplanation. Erosional features like mesa and butte are evidenced at several places in Barakar formations. The Precambrian metamorphic formations stand out as prominent linear ridges in the northern part of the area. In addition to the EW boundary fault, several faults are present in the Gondwana formations. Some of them, as in the Jingurdah coal mines are radial in nature and offset the coal seams. The lineaments characteristic within the coal field area are different compared to the adjoining metamorphic terrain. Selective enhancement techniques are thus called for to delineate all these features and to prepare a detailed structural map. With this in view, the following aspects are taken up for detailed study leading to structural mapping of coal field area:

1. Evaluation of different image smoothing, edge detection and edge lining techniques for enhancement of structural features and to finally evolve a scheme of operation.

2. Application of mathematical morphology based image processing techniques involving fundamental operations of dilation, erosion, opening and closing for delineation of lineaments.
3. To evaluate the above two image processing schemes in terms of their better detection of structural features and computational efficiency.
4. Preparation of a structural map of the study area using the edge image received from these schemes.

In the present work, structural mapping is confined to lineaments including faults.

1.4 Organization of the Work

The material contained in the thesis is organized and presented under seven chapters. Chapter 1 deals with the introduction. Details of the Singrauli coal basin and study area are given. The scope and objectives of the study are defined. In Chapter 2, the data used and the preprocessing techniques adopted are presented.

Based on the false coloured composites created with different band combinations and principal components, geological and geomorphological as well as land use maps are prepared. The details of the same are presented in Chapter 3. Chapter 4 deals with digital enhancement of structural features using image smoothing, edge detection and edge linking techniques.

In Chapter 5, an edge detection approach, based on mathematical morphology is presented. An evaluation of different operations involved, is attempted. Based on the techniques developed in the previous chapters, two schemes of image processing for lineament mapping are proposed and output images have been used for preparation of maps. A statistical analysis of lineament has been carried out for

the area. The details are presented in Chapter 6. The findings of the present work are summarized in Chapter 7.

Chapter 2

PREPROCESSING OF DATA

2.1 Introduction

During the last two decades, launching of several unmanned satellites into the orbit around the Earth has resulted in obtaining the satellite data dealing with features on Earth's surface. Information is now available from several sensor platforms such as LANDSAT – TM, SPOT, ERS and IRS – 1B. In the present work, multi-band and multiresolution data have been selected from two sensor systems namely the LANDSAT – TM and IRS – 1B. These data vary in their spectral ranges and spatial resolution. The orbital path and elevation of the platform is also different in each case. In addition, the data have been recorded on two different dates. Hence to integrate this dataset for further processing, geometric rectification and image resampling were performed.

To take care of the dimensionality of multichannel dataset, a transformation based on *principal component analysis* has also been performed. This transformation has reduced the number of spectral bands and provided the maximum details of the Earth cover types. All these preprocessing techniques adopted in the present work are detailed in this chapter.

2.2 Data Acquisition

Satellite data

In the present work, data from LANDSAT – 5 and IRS – 1B were used. The LANDSAT-5 launched on March 1, 1984 and moving in a Sun synchronous orbit

at an altitude of 705 kms with 16 days repetitive coverage having a field view of 14.93° carries a four – channel multispectral scanner and a thematic mapper (TM). The TM is a scanning optical – mechanical sensor system that records reflected and emitted energy in the visible, reflective–infrared, middle–infrared and thermal–infrared regions of the electromagnetic spectrum and the spatial resolution is 30 m for Bands 1 to 5 and 7 while for Band 6 it is 120 m. The data collected has higher spatial, spectral and radiometric resolution than the one from MSS. Details regarding LANDSAT – TM spectral bands and their applications are presented in Table 2.1.

On the coverage index map, the study area is located by a path number - row number 142 – 043 and the data pertains to April 21, 1992.

Indian Remote Sensing Satellite (IRS – 1B) was launched on August 29, 1991 in a Sun synchronous orbit at an altitude of 904 kms. This satellite carried one pushbroom camera (LISS – I) of 72.5 m resolution and two cameras (LISS – II) of 36.25 m resolution and images obtained are of four spectral bands in the visible and near IR region. The spectral characteristics of IRS – 1B and SPOT are presented in Tables 2.2 and 2.3.

The study area is covered on IRS – 1B index map by path number-row number 23 – 51 and the data pertains to April 25, 1992. The data from IRS – 1B covers essentially the same spectral range as that from SPOT. Although the resolution of SPOT – MLA data is better compared to IRS – 1B LISS – II, the data from SPOT is either of one band (SPOT – PLA) or of three bands (SPOT – MLA) while that from IRS – 1B is of four bands covering the same spectral range. Thus IRS – 1B has an advantage in providing more details.

Table 2.1 LANDSAT - TM spectral bands and principal applications

(Jensen, 1986)

BANDS	SPECTRAL RANGE (micron)	SPECTRAL LOCATION	PRINCIPAL APPLICATION
1	0.45 - 0.52	BLUE	Sensitivity to sedimentation studies, coastal water mapping. soil / vegetation discrimination, forest type mapping.
2	0.52 - 0.60	GREEN	Green reflectance of healthy vegetation, vigor assessment in vegetation.
3	0.63 - 0.69	RED	Sensitivity to chlorophyll absorption by vegetation, differentiation of soil and geological boundaries.
4	0.76 - 0.90	NEAR INFRARED	Sensitivity to green biomass and moisture in vegetation delineating the water bodies and soil moisture mapping.
5	1.55 - 1.75	MID - INFRARED	Useful for vegetation moisture content and soil moisture , discrimination of snow from cloud.
6	10.4 - 12.5	THERMAL INFRARED	Useful in vegetation moisture analysis, soil moisture discrimination, and thermal mapping applications.
7	2.08 - 2.35	MID - INFRARED	Useful for discrimination of minerals and rock types. Also sensitive to vegetation moisture content.

Table 2.2 IRS spectral bands and principal applications (Dept. of Space, India, 1989)

BANDS	SPECTRAL RANGE (microns)	SPECTRAL LOCATION	PRINCIPAL APPLICATION
1	0.45 - 0.52	BLUE	Sensitivity to sedimentation, deciduous / coniferous forest cover discrimination.
2	0.52 - 0.59	GREEN	Green reflectance of healthy vegetation.
3	0.62 - 0.68	RED	Sensitivity to chlorophyll absorption by vegetation, differentiation of soil and geological boundaries.
4	0.77 - 0.86	NEAR- INFRARED	Sensitivity to green biomass and moisture in vegetation

Table 2.3 SPOT - MLA spectral bands and principal applications

(Barret and Curtis, 1992)

BANDS	SPECTRAL RANGE (μm)	SPECTRAL LOCATION	PRINCIPAL APPLICATION
1	0.50-0.59	GREEN	Sensitivity to sedimentation, deciduous / coniferous forest cover discrimination.
2	0.61-0.68	RED	Reflectance of healthy vegetation.
3	0.70-0.89	REFLECTED -INFRARED	Sensitivity to chlorophyll absorption by vegetation, differentiation of soil and geological boundaries.

Table 2.2 IRS spectral bands and principal applications (Dept. of Space, India, 1989)

BANDS	SPECTRAL RANGE (microns)	SPECTRAL LOCATION	PRINCIPAL APPLICATION
1	0.45 - 0.52	BLUE	Sensitivity to sedimentation, deciduous / coniferous forest cover discrimination.
2	0.52 - 0.59	GREEN	Green reflectance of healthy vegetation.
3	0.62 - 0.68	RED	Sensitivity to chlorophyll absorption by vegetation, differentiation of soil and geological boundaries.
4	0.77 - 0.86	NEAR- INFRARED	Sensitivity to green biomass and moisture in vegetation

2.3 Data Retrieval from CCT

The data from NRSA was supplied on the computer compatible tapes (CCT). It was read using a computer software on MICRO VAX System. Since the data on CCT is written in a particular standard format (Ramkrishnan, 1988), a computer software in VMS FORTRAN has been prepared by the author based on the specified format. There are five files on the CCT organized in a superstructure format as described below:

- Volume Directory
- Leader
- Image Data
- Trailer
- Null Volume

The *volume directory file* contains information relating to the tape data. It is composed of volume description record, a series of file pointer records and a text record. The *leader file* constitutes file description record and three types of data record. The data types are header, ancillary and annotation. The *image file* consisting of file description record and actual image data record is followed by a trailer record which finally ends with a *NULL volume* directory file.

The data in the image file is written in two formats either band interleaved by line (BIL) or band sequential (BSQ). In present case the data was procured in BIL format. The first record on the image data file is the file description record of 2520 bytes. In addition, there are 10,000 image data records each of 2520 bytes. The main data on each of these image records are contained in bytes 33 to 2382. A layout of user CCT is shown in the Fig. 2.1.

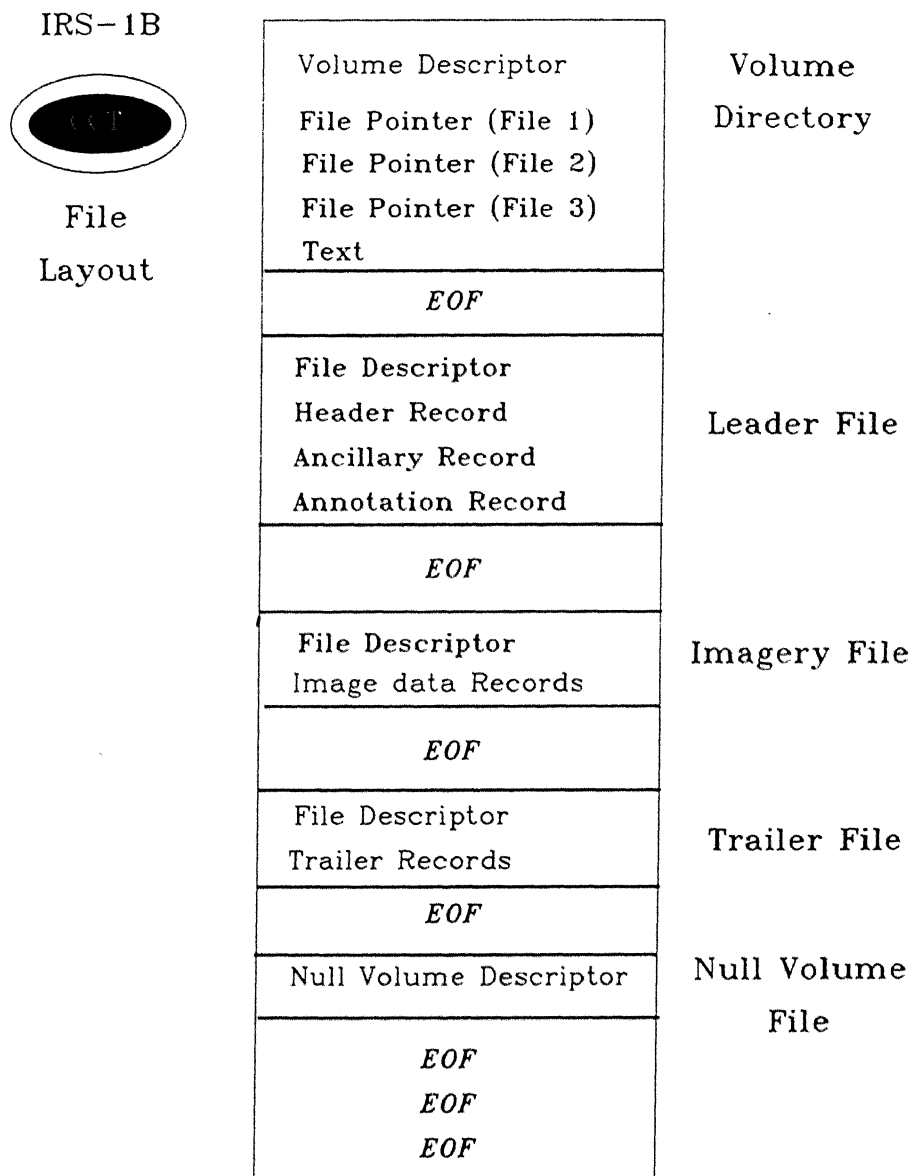


Figure 2.1 : Layout of user CCT of BIL format

A computer software to retrieve the data of different bands of a specified area or subscene as written by the author is presented in the Appendix – A. With the help of this software, data on CCT has been accessed and the exact portion covering the study area has been windowed and the data read and recorded on to the floppies for further processing on a personal computer. The computer system used is of PC 386 with super VGA card and a 19" colour monitor.

The satellite data of the study area comprising of four bands of IRS and one Band of LANDSAT – TM used for digital image processing and analysis are shown in the Figs. 2.2 to 2.6 .

2.4 Preprocessing of Satellite Digital Data

Data supplied to a user is rectified with respect to systematic and non – systematic errors. These errors are rectified before the data being supplied to the user. However, the data used belongs to two satellites, the present problem is to eliminate the systematic and non – systematic incompatibility. The systematic incompatibility is attributed to platform velocity, Earth rotation, scanning system, spatial resolution and spectral resolution. The non – systematic incompatibility is due to altitude, attitude and atmospheric factors.

As already stated that satellite data being used two sensor systems is having different spatial resolution. The data from these sensors are of different dates. The platforms of these sensors are placed at different altitudes and orbits thus involving atmospheric variability. The data can be integrated only after performing corrections to reduce the incompatibility. For this purpose *geometric rectification* and *image resampling* have been performed.

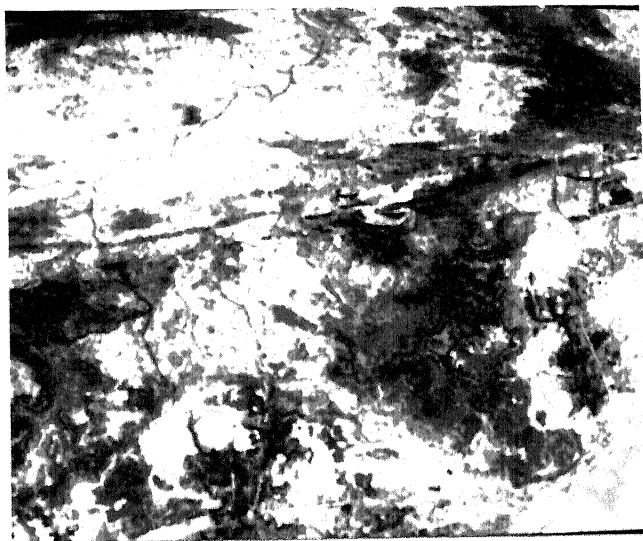


Fig. 2.2 IRS 1B LISS II image of study area, Band 1.

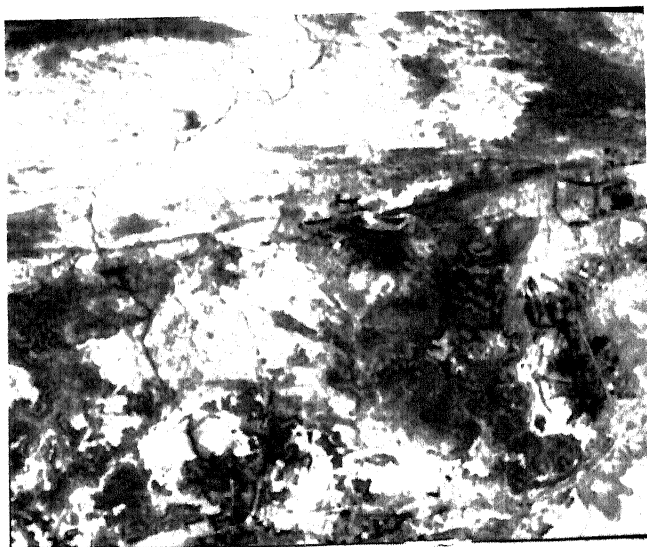


Fig. 2.3 IRS 1B LISS II image of study area, Band 2.

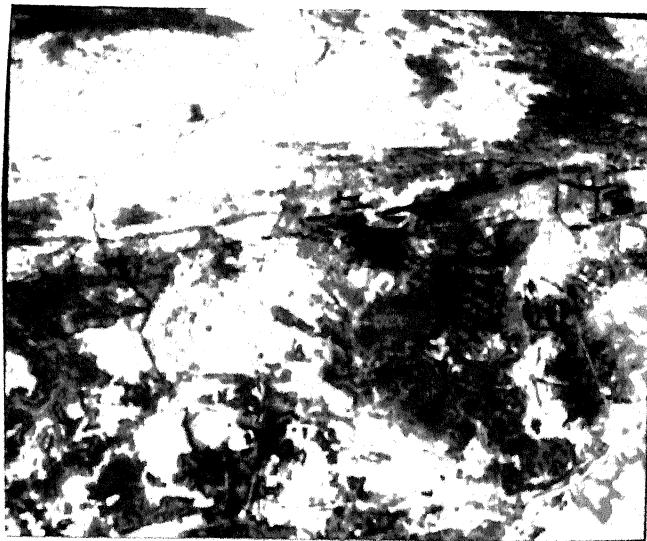


Fig. 2.4 IRS 1B LISS II image of study area, Band 3.

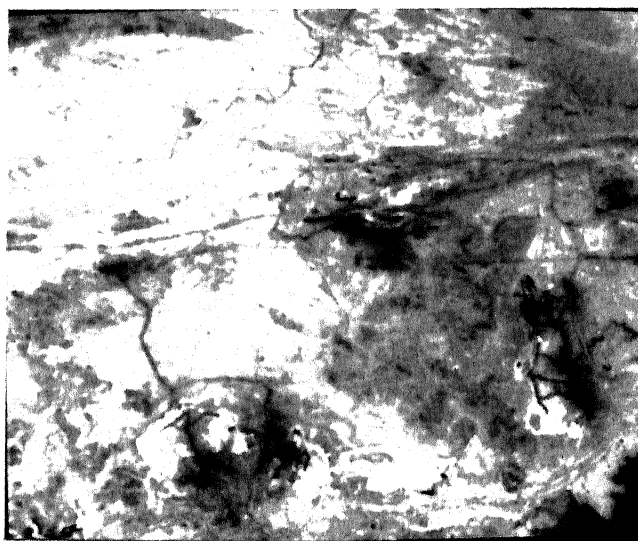


Fig. 2.5 IRS 1B LISS II image of study area, Band 4.

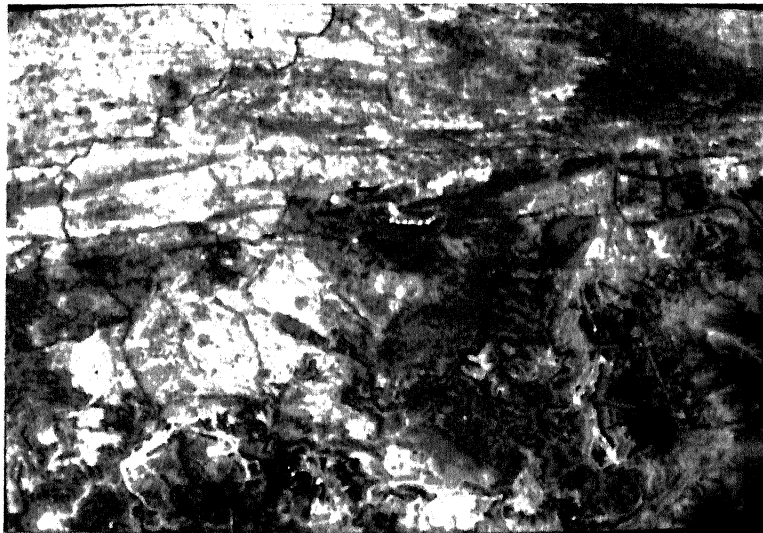


Fig. 2.6 LANDSAT - TM image of study area, Band 7

The LANDSAT – TM data (with a resolution of 30 m) is to be transformed into the grid size of IRS – 1B data (with a resolution of 36.25 m). For this purpose the geometric transformation is carried out as follows :

$$R'_{TM} = T[f(R_{TM}, R_{IRS}, C_{IRS})] \quad (2.1)$$

$$C'_{TM} = T[f(C_{TM}, R_{IRS}, C_{IRS})] \quad (2.2)$$

where

R_{IRS} is line number of IRS – 1B image,

C_{IRS} is pixel number of IRS – 1B image,

R_{TM} is line number of LANDSAT – TM image,

C_{TM} is pixel number of LANDSAT – TM image,

R'_{TM} is line number of geometrically corrected LANDSAT – TM image and

C'_{TM} is pixel number of geometrically corrected LANDSAT – TM image.

For obtaining a transformation of this type, coordinates of ground control points (GCPs) present on both the imagery are required. Eight ground control points were identified both on LANDSAT – TM image and on IRS – 1B LISS – II image. For the geometric correction, image of any band of IRS can be taken. In the present operation Band 3 image of IRS – 1B (Fig. 2.4) was utilized as the same is used subsequently. LANDSAT – TM image utilized for transformation to IRS – 1B grid domain is presented in Fig. 2.6. The size of Band 3 IRS image is 512×512 whereas the size of uncorrected LANDSAT – TM image is 632×616 . Three possible approaches are available for establishing a mapping relationship between line and pixel numbers of LANDSAT – TM and IRS – 1B imagery. They are generally linear, quadratic or cubic. The ground control points required for these three cases should be greater than 3, 6 and 10 respectively. For greater accuracy either quadratic

or cubic relationship is preferred over the linear type. In the present work, the quadratic relation was adopted since the available ground control points were limited within the study area. The quadratic mapping function is of the following form :

$$R_{TM} = b_0 + b_1 C_{IRS} + b_2 R_{IRS} + b_3 C_{IRS}^2 + b_4 C_{IRS} R_{IRS} + b_5 R_{IRS}^2 \quad (2.3)$$

and,

$$C_{TM} = b'_0 + b'_1 C_{IRS} + b'_2 R_{IRS} + b'_3 C_{IRS}^2 + b'_4 C_{IRS} R_{IRS} + b'_5 R_{IRS}^2 \quad (2.4)$$

Eight GCPs from the LANDSAT – TM and IRS – 1B images were picked up (Table 2.4) on the basis of which the coefficients of the quadratic mapping function (Table 2.5) for transforming LANDSAT – TM image coordinates to IRS – 1B coordinate system were computed.

After the geometric rectification of the LANDSAT – TM image into IRS – 1B grid system, the resampling of the LANDSAT – TM image is performed.

Table 2.4 : Ground control points selected for the study area

Point number	Line number (LANDSAT)	Pixel number (LANDSAT)	Line number (IRS)	Pixel number (IRS)
1	573	449	433	332
2	139	486	70	357
3	298	579	205	439
4	406	578	296	439
5	184	325	105	220
6	189	355	112	245
7	386	464	276	343
8	561	247	420	161

Table 2.5 : Coefficient of quadratic mapping function for geometric correction

Coefficient	C_{TM}	coefficient	R_{TM}
b_0	53.7774	b'_0	80.2012
b_1	1.2139	b'_1	-0.0658
b_2	0.0234	b'_2	1.1259
b_3	-0.0001	b'_3	0.0001
b_4	0.0	b'_4	0.0001
b_5	-0.0001	b'_5	0.0001

2.4.2 Image resampling

Once the transformation of grid system has been achieved, it is necessary to read the corresponding grey level values and put them in the new grid domain. The original grid as well as the geometrically corrected grid are shown in Fig. 2.7. As indicated in the figure, the original grey level values can not be directly associated to any of the corrected grid cell. For properly assigning the appropriate grey level values in the new grid, the following techniques are available (Lillesand and Kiefer, 1979).

1. Nearest neighbourhood technique
2. Bilinear interpolation technique
3. Cubic convolution technique

The *nearest neighbourhood technique* has been applied in present case. In this method, the grey level of the nearest cell is adopted for the corrected grid cell. Therefore in the example shown in Fig. 2.7, the grey level of cell 3 - 3 will be recorded in the shaded cell of corrected grid. Here the grey levels are not altered.

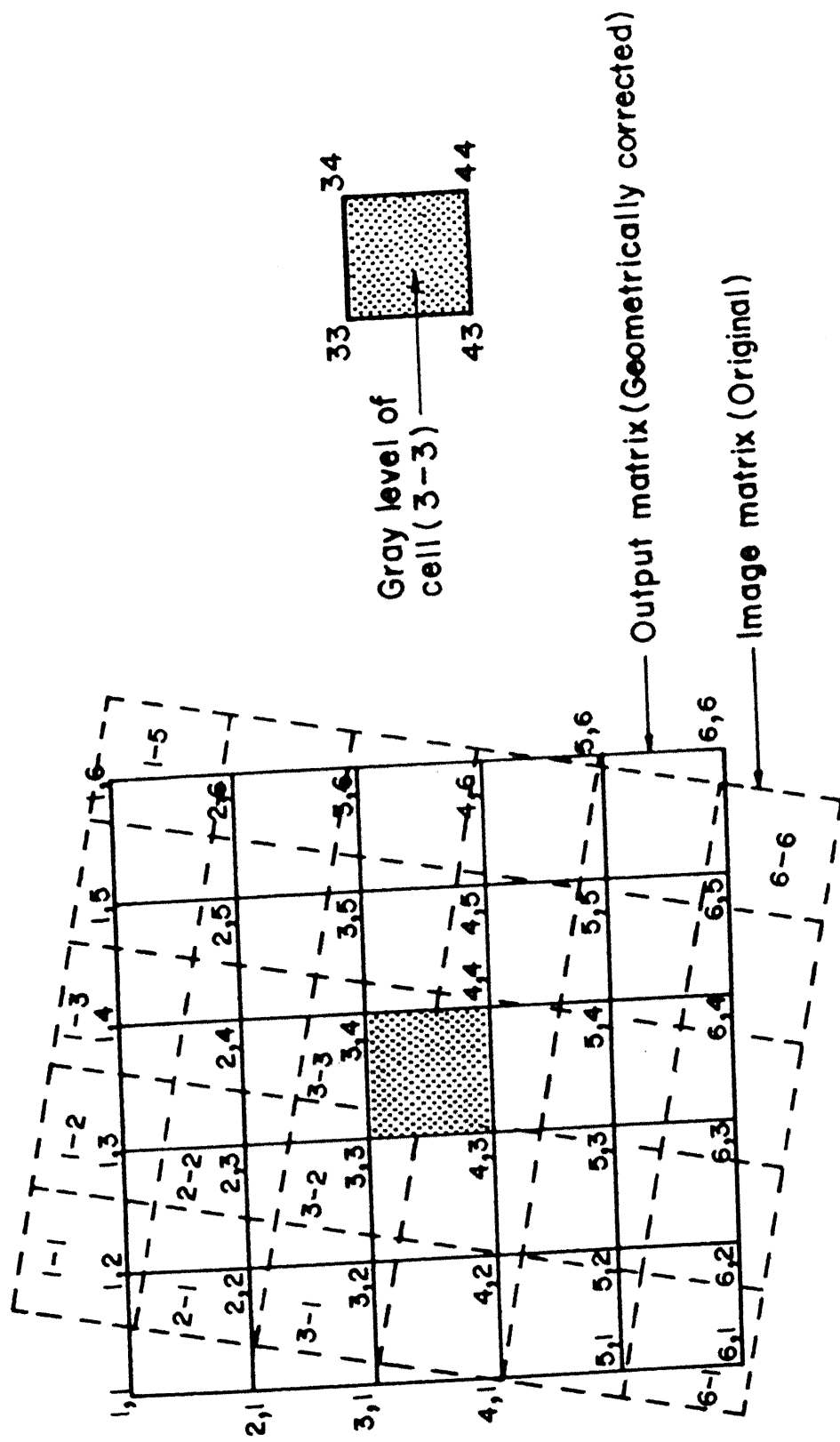


Fig. 2.7: Nearest neighborhood process for resampling.

This technique is computationally very simple and straightforward. The *bilinear interpolation* and *cubic convolution techniques* require large computational time compared to this operation. The grey levels are also modified. Because of this, image may look little smoother but with the transformation of grey level the basic aim behind selecting a particular spectral band is denied. The LANDSAT – TM Band 7 is selected for study as it is very useful for geological feature interpretation. If there is any kind of modification in these spectral responses, then the usefulness of the image for geological applications may severely be affected. Thus, the process of nearest neighbourhood sampling is well justified in present application.

Using this method, the LANDSAT – TM image is transformed in to identical grid as of IRS – 1B LISS – II and the output LANDSAT – TM image is shown in Fig. 2.8. This LANDSAT – TM image has been made use of in subsequent interpretation and processing along with the four IRS – 1B LISS – II bands.

2.5 Data Compression

In the present case the main features targeted for identification are geological. It is also understood that vegetation, drainage patterns and moisture content of surface contribute significantly in the identification of geological details. Incorporating all these details in the best form is not possible by selecting a single spectral band. At the same time it is very difficult to handle large data simultaneously. Another problem of concern, is that the image objects often have intermixing nature of grey level values. This problem is severe in a highly correlated dataset and imposes a problem of misclassification and misinterpretation. To maximize the variance and minimize the correlation, the technique of *principal component analysis* (Jolliffe, 1986; Jensen, 1986) was utilized. The principal components are computed using the *Karhunen – Loeve transformation* (Moik, 1987).

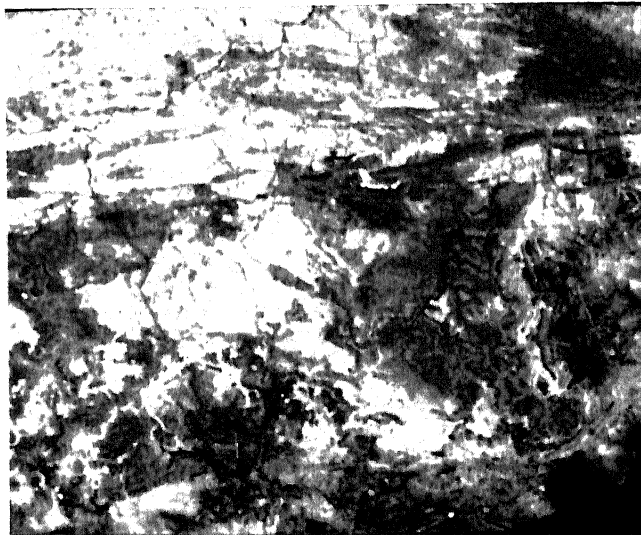


Fig. 2.8 Geometrically corrected LANDSAT - TM image of study area.

The main objective of principal component analysis is to transform a highly correlated n - dimensional data set into a lesser dimension feature space by redistributing the variance and information content. Number of bands or dimension of data should be equal or more than the desired components.

For understanding the concept of principal component analysis a two - dimensional case has been explained that can also be extended to the multi - dimensional case. For two bands b_1 and b_2 , the principal components p_1 and p_2 can be computed as

$$p_1 = c_{11}b_1 + c_{12}b_2 \quad (2.5)$$

$$p_2 = c_{21}b_1 + c_{22}b_2 \quad (2.6)$$

This can be expressed in the matrix form as,

$$\begin{bmatrix} p_1 \\ p_2 \end{bmatrix} = \begin{bmatrix} c_{11} & c_{12} \\ c_{21} & c_{22} \end{bmatrix} \begin{bmatrix} b_1 \\ b_2 \end{bmatrix} \quad (2.7)$$

By a graphical representation this concept can be better appreciated as shown in Fig. 2.9. The data of two spectral bands of an image are plotted on two axes b_1 and b_2 (Fig. 2.9 a). The scatter plot is reflecting a highly correlated dataset and hence the image is of very little information value. To augment the information value of an image, the correlation of dataset has been reduced by transformation to maximize the variance. In the two - dimensional case, first a linear transformation is applied by linear translation of the origin of previous coordinate system. For this purpose mean values of bands, b_1 and b_2 are determined as μ_1 and μ_2 . A new coordinate system based on b'_1 and b'_2 is then derived by a simple expression

$$b'_1 = b_1 + \mu_1$$

$$b'_2 = b_2 + \mu_2$$

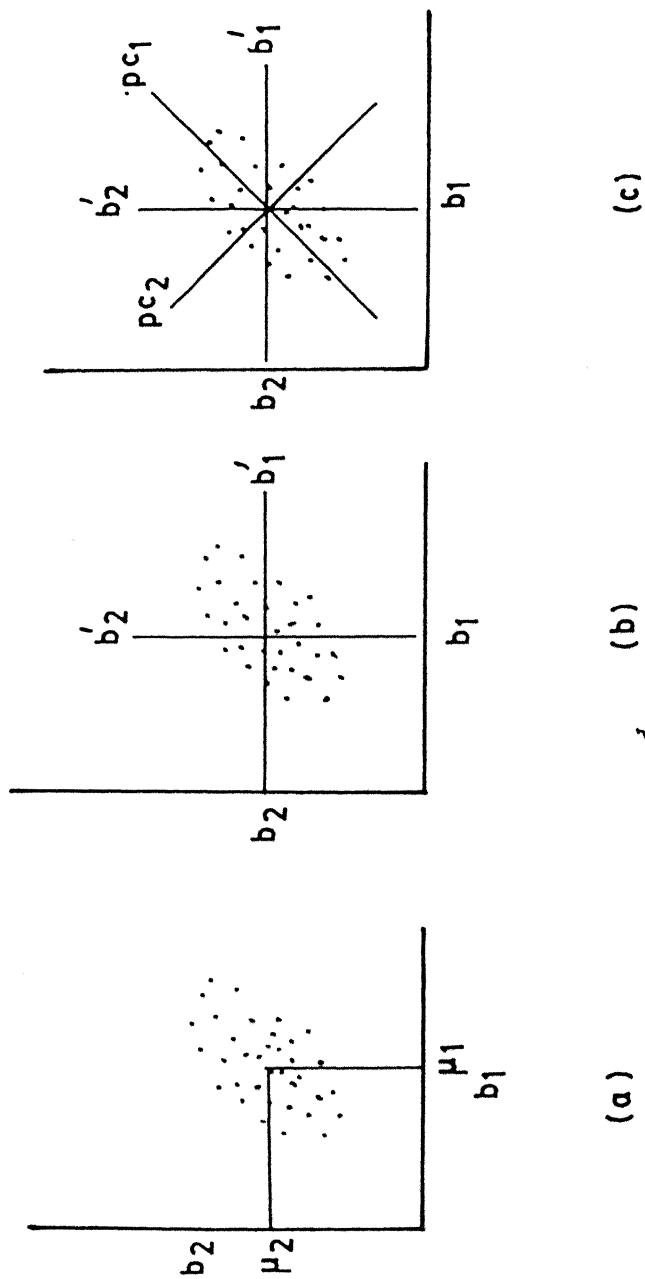


Fig. 2.9 Graphical illustration of data transformation using principal component analysis;

(a) Scatter plot of Band 1 and 2; (b) Linear translation of the origin and axes; (c) Rotation of axes to map the data in the direction of maximum variance.

This is illustrated in Fig. 2.9 (b). In order to obtain the maximum variance along one principal component, the newly found axis is again rotated by an angle θ so as to align b'_1 along the maximum variance direction which is along the major axes direction in the present figure. This component is the first principal component (PC_1) and the component orthogonal to it is the second principal component (PC_2). The rotation transformation is illustrated in Fig. 2.9 (c). In order to reproject the original dataset onto the new (PC_1) and (PC_2) axes, certain transformation coefficients are needed which are derived from the covariance matrix of the original dataset.

Similarly on a multichannel dataset which is highly correlated, a transformation has to be applied to produce a new multichannel uncorrelated dataset having an ordered set of variance. The transformation for a multichannel spectral case is carried out in the following steps :

- (1) The mean and standard deviation values for the given spectral bands TM (Band 7), IRS (Band 1), IRS (Band 2), IRS (Band 3) and IRS (Band 4) are determined.
- (2) Variance – Covariance matrix for this dataset is computed (Table 2.6).
- (3) The correlation matrix is computed (Table 2.6).
- (4) The eigen values and eigen vectors are calculated such that

$$[EV][COV][EV^T] = \begin{bmatrix} \lambda_{11} & 0 & 0 & 0 & 0 \\ 0 & \lambda_{22} & 0 & 0 & 0 \\ 0 & 0 & \lambda_{33} & 0 & 0 \\ 0 & 0 & 0 & \lambda_{44} & 0 \\ 0 & 0 & 0 & 0 & \lambda_{55} \end{bmatrix} \quad (2.8)$$

where, λ_{nn} , $n = 1 \dots 5$ are eigen values for Bands 1 to 5. Here, Band 1 designated

for TM Band 7, and Bands 2 to 5 are for Bands 1 to 4 of IRS. The right hand side matrix is the diagonal matrix having respective eigen values as diagonal elements.

EV is eigen vector.

$$EV = [a_{rs}]$$

where, $r = 1$ to 5 Bands and $s = 1$ to 5 components.

EV^T is the transpose of matrix EV

Percent of total variance ($\%_{PC}$) contained in each principal component is determined by the expression

$$\%_{PC} = \frac{\lambda_{PC}}{\sum_{p=1}^n \lambda_{PC}} \times 100 \quad 2.9$$

where λ_{PC} is the eigen value for concerned principal component. In present case $n = 5$.

By evaluating the correlation of each band with each component it is possible to determine how each band is associated with each principal component or its *factor loading*.

$$f_{rs} = \frac{a_{rs} \times \sqrt{\lambda_p}}{\sigma_r} \quad (2.10)$$

The computed percent variance, eigen values, eigen vectors and factor loadings are listed in the Table 2.7.

In above case five principal components have been computed for the five spectral channels in consideration. As evident from the Table 2.7, the maximum information (upto 61.64 percent) is contained in the first principal component. The image of this principal component is shown in the Fig. 2.10. The first and second component together offer information upto 92.80 percent. In addition, the fourth principal component is integrated with the first two. Although the fourth principal component exhibits only 1.36 percent variance, its image (Fig. 2.11) depicts a detailed

lineament fabric of the study area. The first, second and fourth principal components were used in this study to generate FCC which has been used in the study for further interpretation.

Table 2.6 : Variance – Covariance matrix and Correlation matrix of original dataset

Variance – Covariance Matrix

	TM7	IRS1	IRS2	IRS3	IRS4
TM7	481.35	-31.17	-20.52	16.22	76.26
IRS1	-31.17	56.38	48.73	70.31	20.15
IRS2	-20.52	48.73	48.09	75.06	24.83
IRS3	16.22	70.31	75.06	138.31	65.41
IRS4	76.26	20.15	24.83	65.41	85.70

Correlation Matrix

	TM7	IRS1	IRS2	IRS3	IRS4
TM7	1.0000	-0.1892	-0.1349	0.0629	0.3755
IRS1	-0.1892	1.0000	0.9359	0.7962	0.2899
IRS2	-0.1349	0.9359	1.0000	0.9204	0.3868
IRS3	0.0629	0.7962	0.9204	1.0000	0.6008
IRS4	0.3755	0.2899	0.3868	0.6008	1.0000

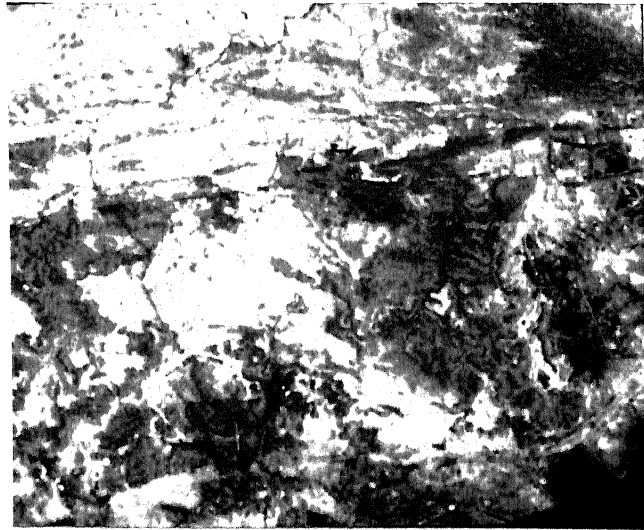


Fig. 2.10 Principal component 1 image of study area.



Fig. 2.11 Principal component 4 image of study area.

Chapter 3

GEOLOGICAL AND LAND USE MAPPING USING SATELLITE DATA

3.1 Introduction

For the demarcation of lithological boundaries, geomorphological features and structural details, false colour composites find extensive use. IRS data earlier has been used for similar purpose, effectively. Krishnamurthy (1990) used false colour composites generated from Bands 1, 2, 3 and 4 of IRS for discriminating litho units and for the identification of major geological and geomorphic features. Ganesh Raj and Gupta (1990) have prepared a hydrogeomorphological map based on FCC generated from IRS-1A LISS-II data. Newton and Boyle (1993) have utilized Landsat TM data for preparation of FCC of principal components to retrieve geological information. According to them, such FCC is more useful for differentiating rock types compared to the FCC of SPOT data.

To have an overview of the study area, false colour composites have been generated and used in this chapter. These have been prepared using various combinations of four bands of IRS data. In addition, principal components calculated earlier using four bands of IRS and Band 7 of LANDSAT TM, have been integrated to create FCC which has been utilized for geomorphological and land use mapping.

3.2 Lithological and Structural Mapping

False colour composites using IRS Bands 1, 3 and 4 (Fig. 3.1) and Bands 1, 2 and 4 (Fig. 3.2) have been generated on VAX 11/780 computer system.

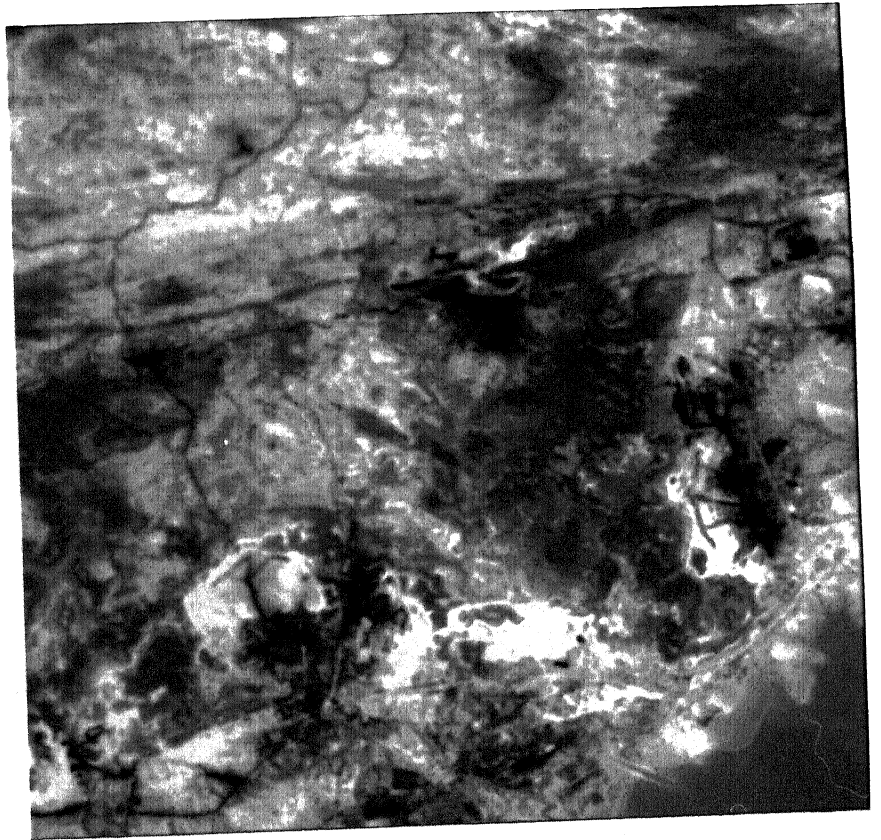


Fig. 3.1 False colour composite of IRS (Bands 1, 3 and 4)

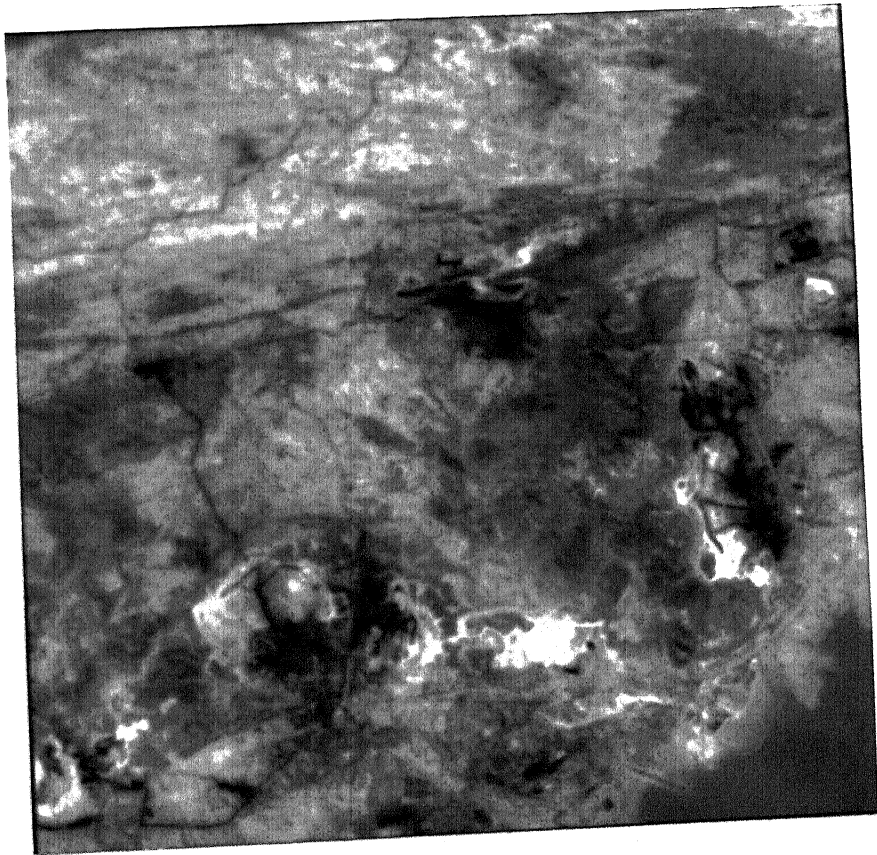


Fig. 3.2 False colour composite of IRS (Bands 1, 2 and 4)

These have been used along with Band 7 image of Landsat TM for the visual interpretation and mapping of geological and structural details (Fig. 3.3). In the study area, the different sedimentary formations of the lower Gondwana group could be clearly recognized and the boundaries marked. In addition, within the Precambrian metamorphic terrain, gneisses could easily be distinguished from the slates and phyllites.

The major EW trending boundary fault is seen clearly on the FCC along with another fault in metamorphic terrain in the eastern part of the area. Several faults in the Jingurdah region and in the SW part of the study area could be identified. Fault delineation in other parts of the area was not possible on FCC due to tonal contrast limitations. Methodology, presented in the subsequent chapters, has enabled a clear delineation of all the linear features in the entire study area.

3.3 Geomorphological Mapping

Classification of the area in terms of various geomorphic units is carried out. For this purpose, FCC (Fig. 3.4) is generated as already indicated in Section 3.1. The structural ridges in the region of slates and phyllites (for example: A2, B2, B1, C1) and in the gneissic terrain (D4, G4, H4, C4) are clearly visible. Drainage network of Bijul river in the NW part of the area (A4 to F1) with its dendritic pattern has been observed to flow at several places along the lineaments indicating a distinct structural control of drainage in the region (B3-C3, A4-B4, C3, D2-E2, E1 and F1).

As already indicated, the coal field area stands out, in contrast, as a plateau compared to the adjoining metamorphic region. The drainage pattern of Bijul river (B6-B4 and E5-E3) is in conformity with the same. Another drainage network Ballianala (E10, F10, E11, H11, I11) flowing through coal mine areas of Dudhichua (E9) could be easily traced upto its final merger into the G. B. Pant reservoir.

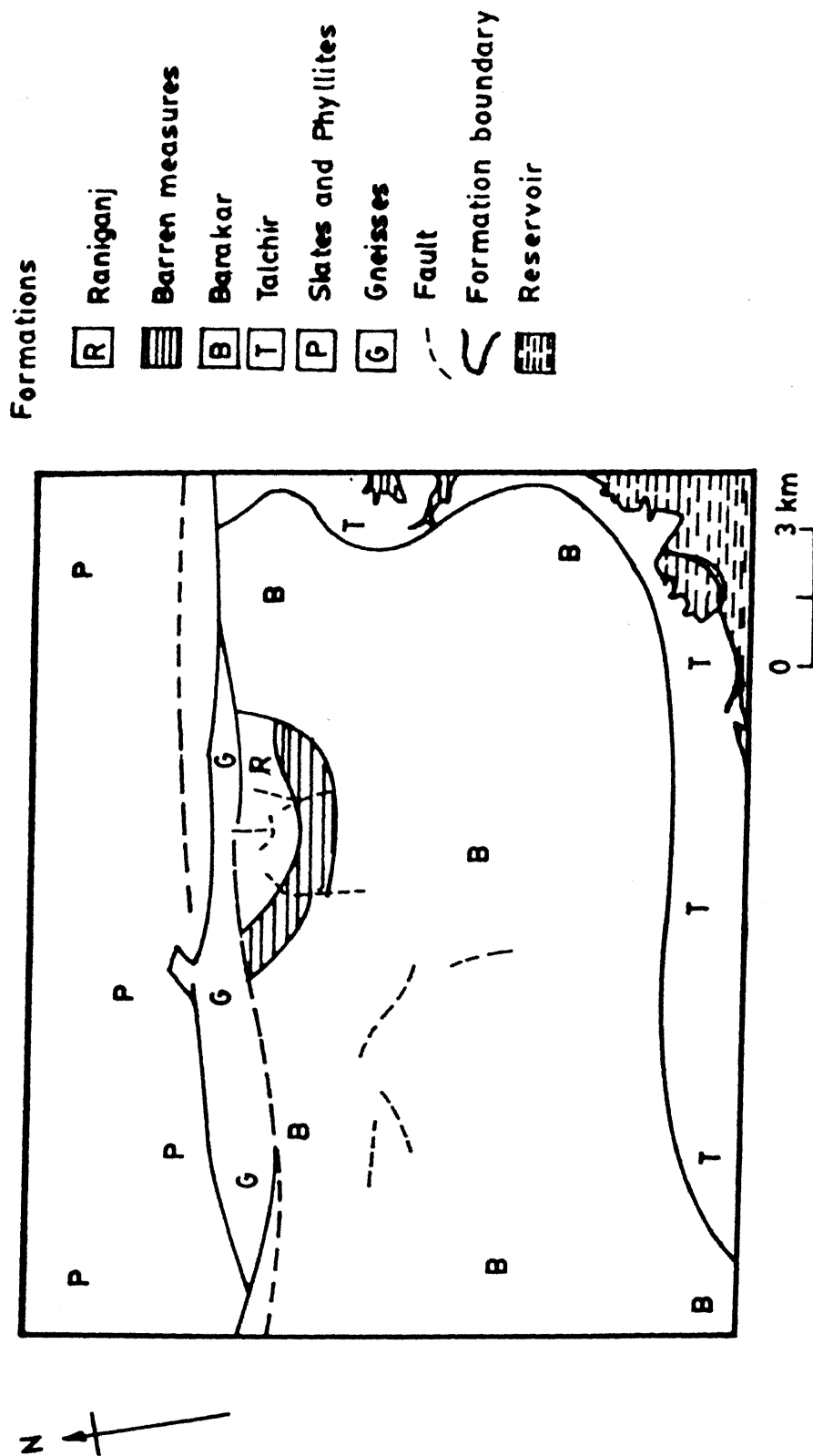


Fig. 3.3 Lithological and fault demarcation based on false colour composites and LANDSAT-TM image of Band - 7

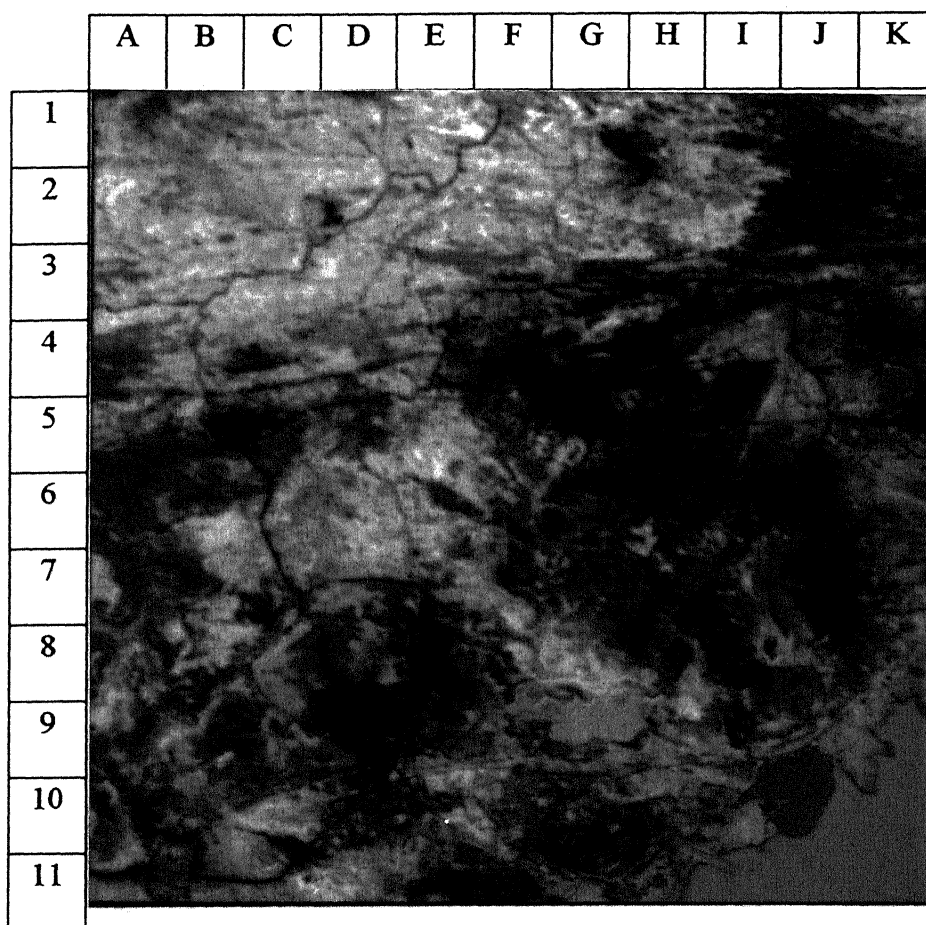


Fig. 3.4 FCC generated by using principal components 1, 2, and 4.

The flow direction confirms the elevation gradient from Barakar terrain to Talchir terrain.

Pediment zones in several places (A5, B7, C6, E5, and E7) and pediplain areas (D6-E8) within Barakar terrain are identified. Several Mesa and Butte features (A7, A9, B8, H5, H6, H7) are also mapped. The geomorphological map prepared is presented in Fig. 3.5. During field checks, typical geomorphic features observed in the field are presented in Figs. 3.6 to 3.10.

3.4 Land Use Mapping

The FCC (Fig. 3.4) of principal components has also been visually interpreted to prepare land use map (Fig. 3.11). Mining activity in the region has a significant impact on the ecology. As the coal mining is through open cast method, serious environmental hazards have resulted. These include depletion of vegetation or forest cover, degradation of agricultural land, piling of huge mine dumps (Fig. 3.12) and acid mine drainage (Fig. 3.13) that pollutes the G. B. Pant reservoir.

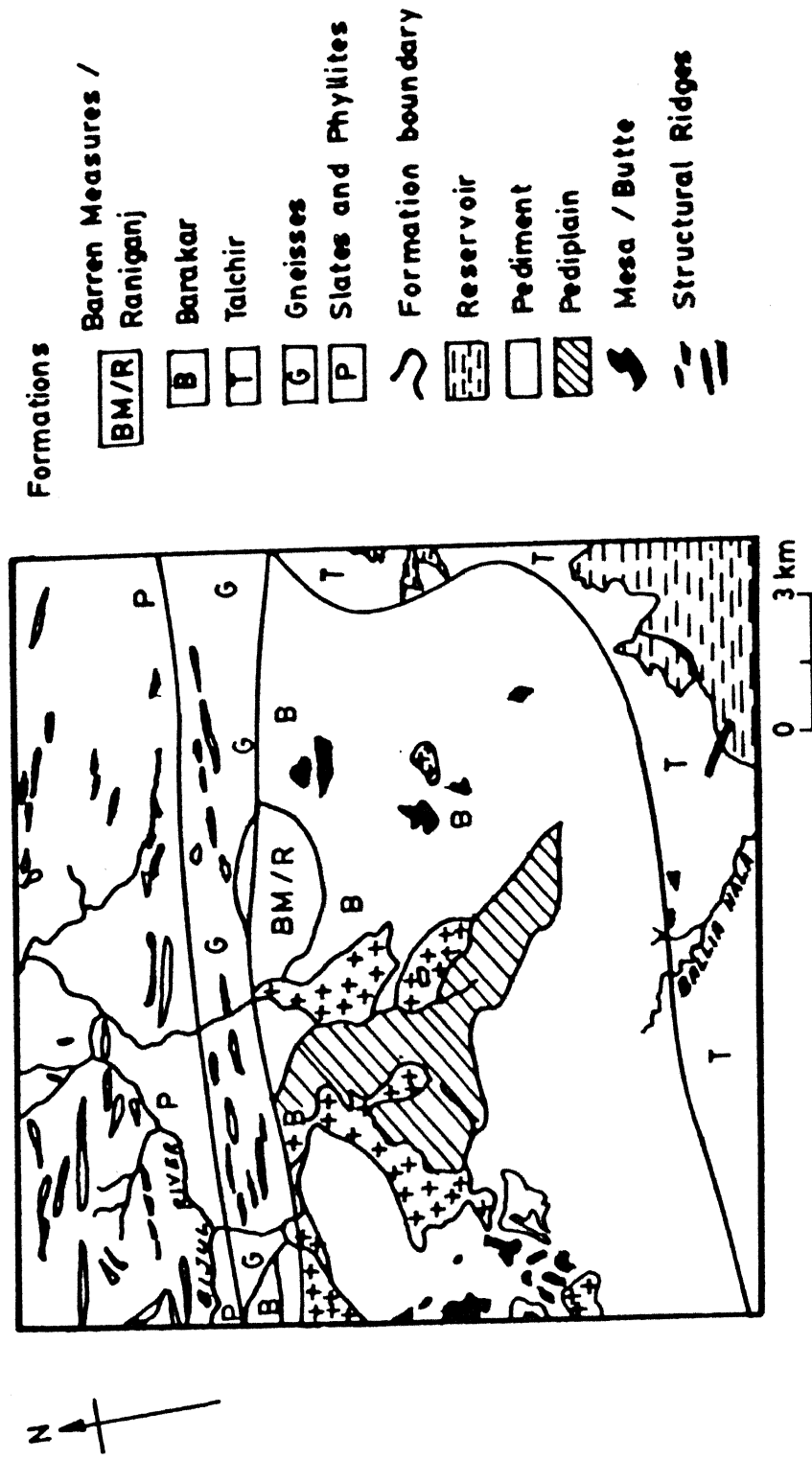


Fig.3.5 Geomorphological map of the study area prepared from false colour composite generated using principal components (Fig. 3.4)

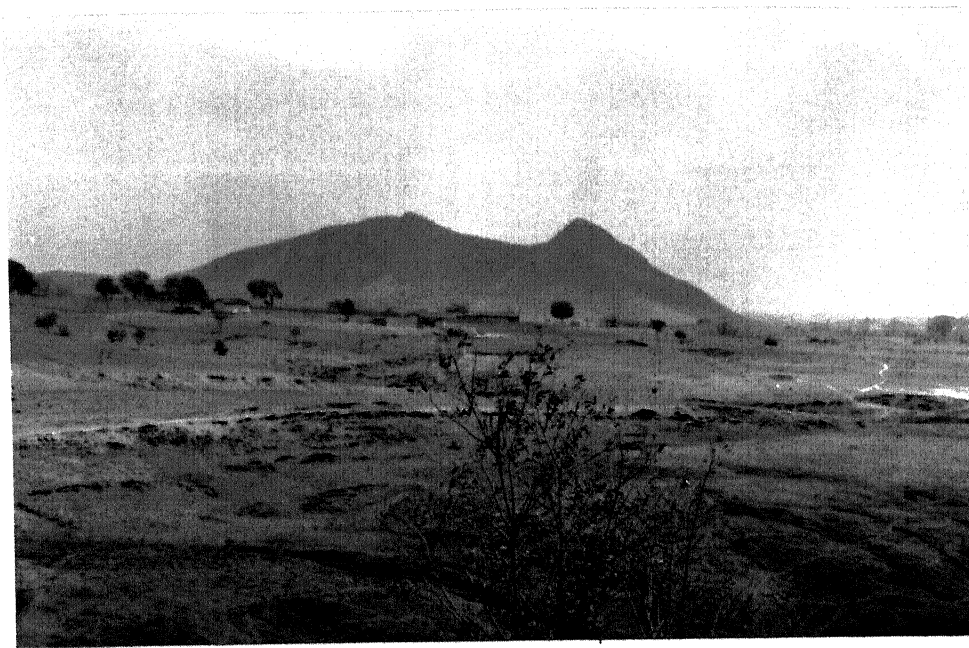


Fig. 3.6 Structural ridges in slates and phyllites near Khirba.

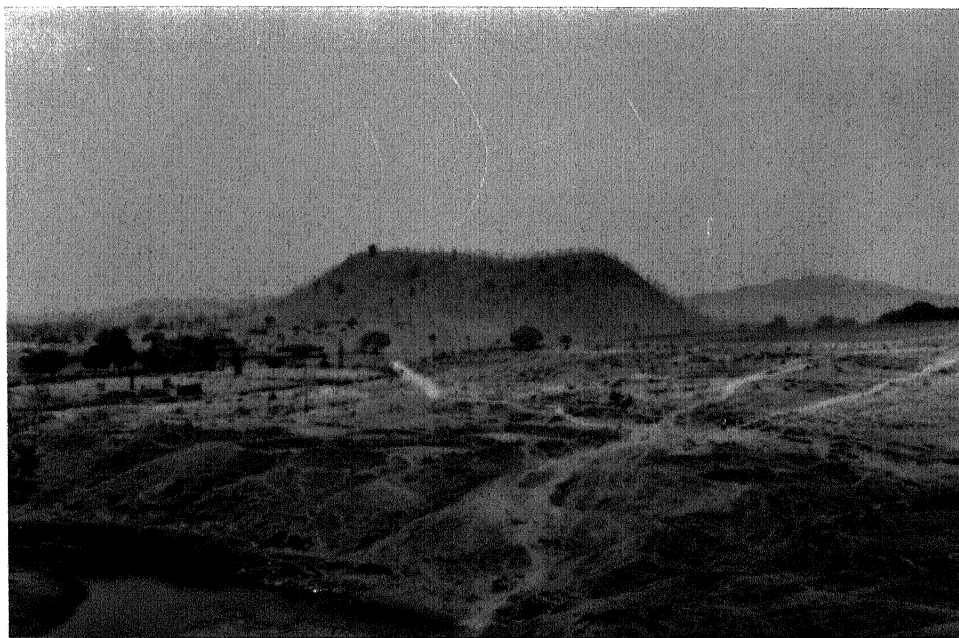


Fig. 3.7 Structural ridges in gneissic terrain near Bijul river (North of Singrauli)

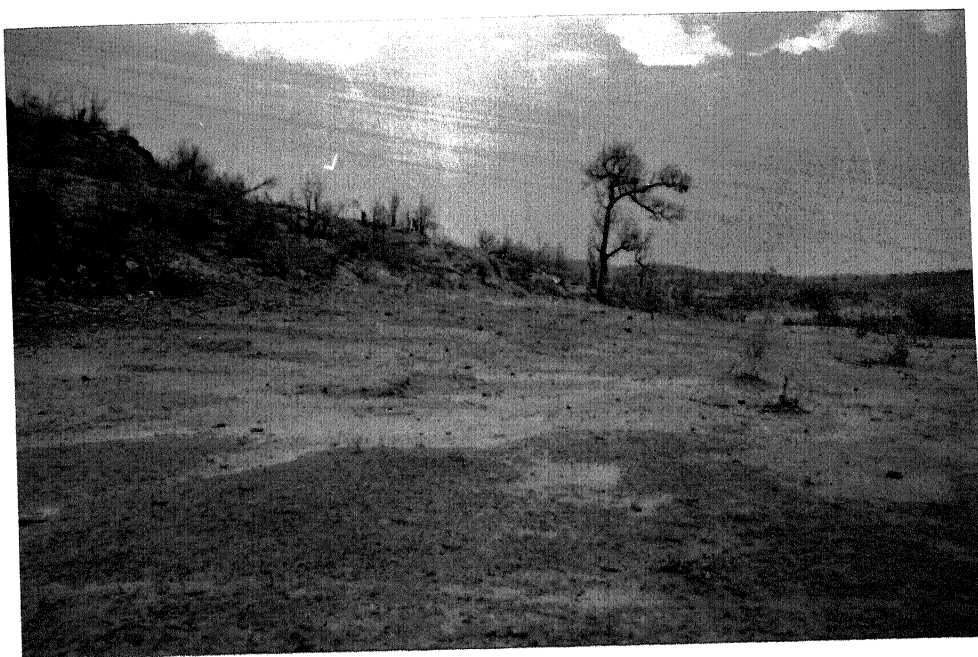


Fig. 3.8 Typical pediplain in the Barakar terrain near Merhauri.

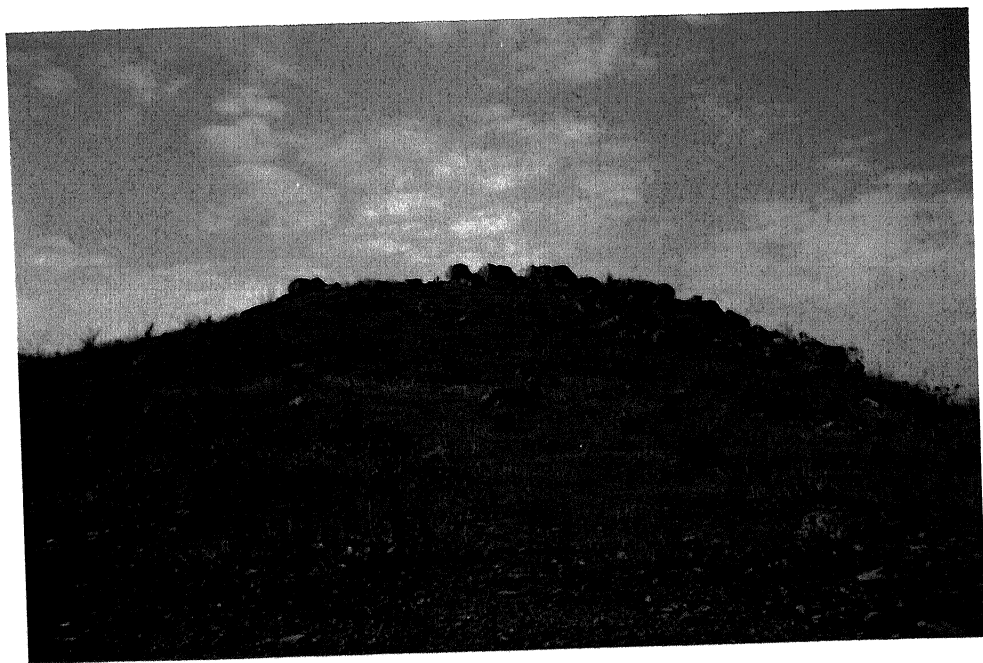


Fig. 3.9 A typical mesa in Barakar terrain near Nigahi.



Fig. 3.10 Butte in Barakar terrain near Shaktinagar.

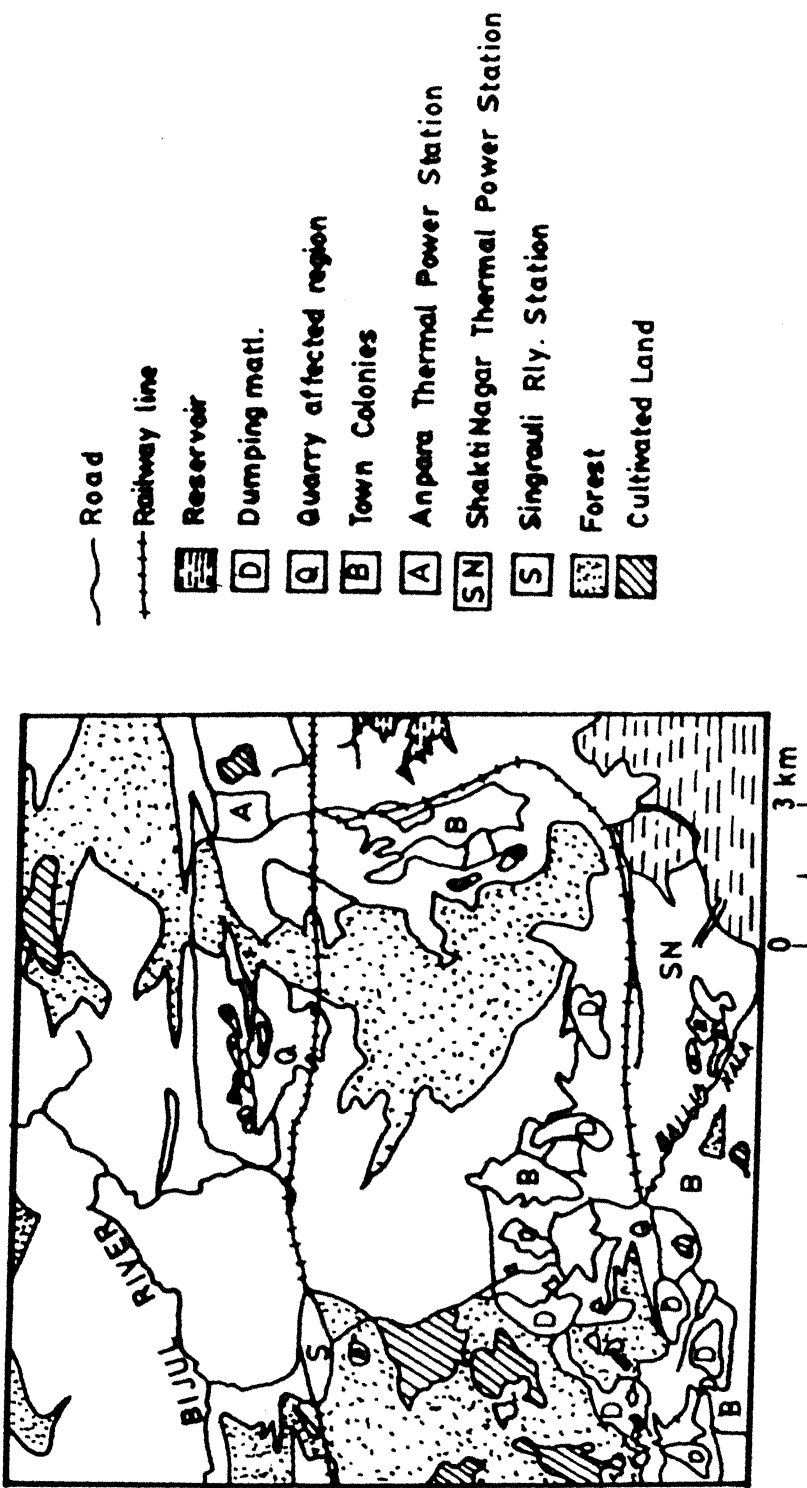


Fig. 3.11 Land use map of the study area prepared from FCC generated using principal components (Fig. 3.4)

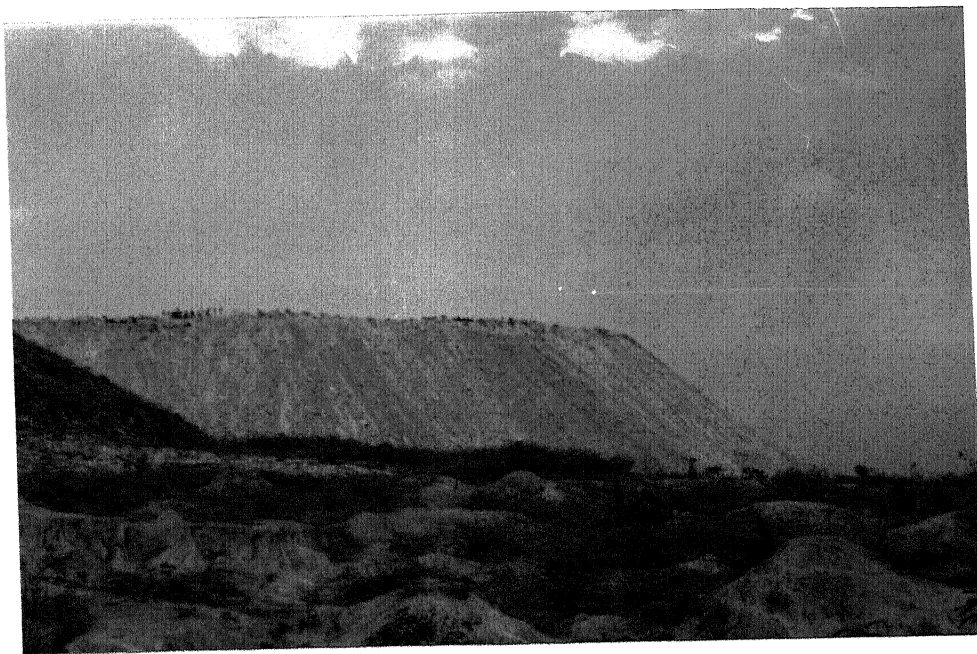


Fig. 3.12 A mine dump in the Jayant block.



Fig. 3.13 Ballia nala polluted with mine drainage prior to its confluence with G.
B. Pant reservoir.

Chapter 4

DIGITAL ENHANCEMENT OF LINEAMENTS

4.1 Introduction

Structural features such as lineaments, faults, joints, fractures, folds are manifested on the surface of the Earth by their specific signatures. Satellite images offer a global view of the Earth's surface and facilitate the identification of these geological structural features. Due to various Earth cover types like forest, agriculture and urban sprawl, it is often not possible to delineate structural patterns efficiently. Image processing techniques play an important role in enhancing the structural features in such cases.

Satellite imagery is utilized for digital enhancement using filtering in frequency or spatial domain. Structural features are enhanced by enhancing the edges. Edges are defined as the boundary between two regions with relatively distinct grey level properties (Gonzalez and Wintz, 1977). The objective of filtering in present case is to enhance the edges. Choice of individual filters depends on specific requirement. If *a priori* knowledge of the lineament pattern in the area is available, a filtering scheme based on this criterion may be adopted for the best result. Folds have special curvilinear nature while faults, fractures and joints approximately follow a straight line pattern.

Edge detection is a process of applying a transformation (T) to an original image $f(x, y)$ to obtain the output image $g(x, y)$ containing edge informations. Mathematically, It may be expressed as

$$g(x, y) = T[f(x, y)] \quad (4.1)$$

and hides important details. These techniques are computationally costly. The local operators are applied to the noisy images in a small neighbourhood of the concerned pixel in the computation. They have great potential of real time or near-real time implementation, because several pixels can be processed in parallel without waiting for their neighbouring pixels to be processed. Local processing can be implemented with better control over the preservation of subtle details and edges. Due to their computational efficiency as well as better result, local operators are gaining popularity over global smoothing (Lee, 1983).

The most popular among local smoothing methods is the moving average method which is mathematically simple and useful in many applications. Median filter in one or two dimensions has become popular due to its characteristics of edge preservation and removal of spikes (Huang, 1981). The other popular smoothing operations used by many researchers are edge preserving smoothing of Nagao and Matsuyama (1979), the gradient inverse weighting scheme of Wang et al. (1981), the box-filtering algorithm (McDonnel, 1981) and the local statistics methods of Lee (1980, 1981). It is not appropriate to generalize their ranking since an algorithm effective for a class of images, may be ineffective for others. In the present study four image smoothing techniques namely moving average filtering, sigma filtering, median filtering and pseudomedian filtering are being discussed and compared, based on computational requirement as well as suitability.

4.2.1 Moving average filtering

An image $f(x, y)$ is transformed to a smoothed output image $\bar{f}(x, y)$ whose grey level at each pixel location (x, y) is found by averaging the grey level values of the pixels of image contained in a predefined neighbourhood of central pixel at (x, y) . The neighbourhood size varies with the nature of the image. The transformation is

obtained as

$$\bar{f}(x, y) = \frac{1}{N \times N} \sum_{(x, y) \in S} f(x, y) \quad (4.2)$$

for $x, y = 0, 1, \dots, (N - 1)$. S is a set of coordinates of points in the neighbourhood of the point (x, y) including (x, y) itself and $N \times N$ is the total number of points in the neighbourhood (Gonzalez and Wintz, 1977). It has been reported by Gonzalez and Wintz (1977) and Lee (1980) that this filter is useful in some cases but fails in many other applications due to its main drawback of blurring the edges.

For a band 3 image of IRS, this method has yielded a better smoothed output over a 3×3 size window compared to a 5×5 size window. The image received in latter case is oversmoothed and appears blurred. The degree of blurring is found to be strongly proportional to the size of the neighbourhood used.

Moving average method due to its drawback of blurring the edges, is unlikely to yield desirable smoothing output.

4.2.2 Sigma filtering

Sigma filtering has an improvement over the moving average filtering. As already discussed, in the moving average filters the edges get blurred as it replaces the central pixel of the window by the neighbourhood average. This is the result of blind averaging of pixels which are not exactly the real members of a feature family. Nagao and Matsuyama (1979) and Lee (1981) have produced solutions to rectify this problem.

Sigma filtering, also on similar lines, uses the basic concept of the sigma probability of *Gaussian distribution*. The primary aim in this filtering is to replace the central pixel of the kernel by the average of pixels which are members of the same feature class. This is attained by locating those neighbouring pixels having their

intensity within a fixed sigma range of the central pixel of the kernel. Replacing the central pixel of the kernel by the average of selected neighbouring pixels has also been suggested by various other researchers. The filter proposed by Nagao and Matsuyama (1979) replaces the central pixel of the kernel by the average of a subregion which has minimum variance. Lee (1981) has evolved a concept of using gradient information in his modified local statistics of neighbouring pixels. In the extended box-filtering algorithm the average is computed only for those neighbouring pixels falling within a fixed grey level domain (Pratt, 1991). Box-filter and sigma filter differ only in one way in that the box-filter has the grey level range fixed throughout the whole image while the sigma filter has freedom of adaptable grey level range.

Several advantages of sigma filter are

1. **Edge preservation** : The noise in the image space and near the boundaries and edges will be smoothed without blurring the edge because only pixels falling on one side of the edges are utilized while computing the average. Since not all pixels are included in average the blurring effect is avoided.
2. **Preservation of shape** : Sigma filtering does not resort to any biases for direction as adopted by Nagao and Matsuyama (1979) and Lee (1981) in their methodology. This helps in retaining the original shape of inherent details which is very important as far as the remote sensing imagery is concerned as a change in morphology affects the process of feature identification.
3. **Preservation of salient details** : By selecting a proper window size, the salient subtle details of several pixel group pertaining to similar class and linear features of desired dimension can be designed to be preserved since only relevant pixels are included in computation of the average and not the background information.

4. **Efficiency of computation** : It is computationally more efficient since only simple comparison and addition operations are performed.

The class of pixels in a very tiny neighbourhood, uncorrelated with the surrounding image space, is generally considered *a noise*. Most of the image noises are characterized by *Gaussian distribution* (Lee, 1983). The two-sigma probability for a feature space is defined as the probability of a random variable being within two standard deviations of its class mean. Here one can recall that the two-sigma probability for a one-dimensional Gaussian distribution is 0.955. This means that 95.5% of random pixels lie within the range of two standard deviations. Any pixel falling outside the two-sigma range most likely comes from a different population and hence it should be excluded from the computation of the average. It is assumed that *a priori* mean comes from the two-sigma range of the grey level values of the pixels to be smoothed.

Assuming that the noise is additive in nature with zero mean and standard deviation of σ , the sigma filtering (Lee, 1983) on a discrete image is performed as follows :

1. A grey level range $(r_{ij} + \Delta, r_{ij} - \Delta)$ is formed, where r_{ij} is the grey level value of the pixel (i, j) and $\Delta = 2\sigma$.
2. Compare the neighbourhood pixels in the specified window.
3. Compute the sum of all the pixel lying in the specified grey level range.
4. Compute the average by dividing the sum by the number of pixels included in the computation of the sum.
5. Now $\hat{r}_{ij} = \text{average}$.

6. Replace the kernel by \hat{r}_{ij} .

Mathematically the algorithm may be explained as follow :

$$\delta_{kl} = \begin{cases} 1, & \text{if } (r_{ij} - \Delta) \leq r_{kl} \leq (r_{ij} + \Delta); \\ 0, & \text{otherwise.} \end{cases}$$

Then,

$$\hat{r}_{ij} = \frac{\sum_{k=i-n}^{n+i} \sum_{l=j-m}^{m+j} (\delta_{kl} r_{kl})}{\sum_{k=i-n}^{n+i} \sum_{l=j-m}^{m+j} \delta_{kl}} \quad (4.3)$$

By assuming a two-sigma range it is ensured to include 95.5% of the pixels from same feature space. At the same time it is also ensured not to include pixels representing high contrast edges such as spikes. Structural information from satellite imagery which is linear in nature, is mostly retained if it is two or more pixels wide, because only those pixels falling within the specified two-sigma range are included in the average. This is the main drawback as the scattered noise of one or two pixels size will not be smoothed, resulting in an undesirable output specially in case of noisy image. This problem is resolved by replacing the two-sigma average with the window average. If the number of pixels within the specified range, is less than a threshold value m then the step (5) is replaced by

$$\hat{r}_{ij} = \begin{cases} \text{two-sigma average,} & \text{if } n > m; \\ \text{immediate neighbour average,} & \text{if } n \leq m \end{cases} \quad (4.4)$$

where, n is number of pixels in the specified range.

The value of m should be carefully chosen to remove isolated spot noise without affecting linear features. For a 7×7 window, m should be less than 4 while for a 5×5 window it should be less than 3. It is found that subtle textures within two sigma-range are wiped out after few iterations (Lee, 1983). If conservation of

textural information is required which is vital in the case of remote sensing, a small Δ range and one or two iterations should be used.

Generally local smoothing operators do not require any prespecified threshold or any parameter. Sigma filter requires specification of the grey level range and the size of the window.

The computational ease and efficiency in addition to edge preserving nature and other advantages over contemporary smoothing algorithms makes sigma filter a distinct choice to be adopted in the case of remotely sensed imagery. The main drawback found in the present application is of selecting a common threshold m . The reason being that remote sensing image contains a wealth of information i.e. local variance in a neighbourhood changes abruptly. This results in turning the sigma filter into moving average filter most of the time. Thus all the advantages discussed above are not realized in the case of an overall image.

Window sizes of 3×3 and 5×5 are selected for smoothing using sigma filtering. Results of smoothing obtained by 3×3 sigma filter are better than those of moving average filter.

4.2.3 Median filtering

Median filtering is a nonlinear signal processing technique which is generally used for image smoothing and has received much of the attention due to its edge preserving nature. Tukey (1971) has suggested it as a tool in time series analysis. Afterwards, it was applied in digital image processing. Median filtering can be one-dimensional or two-dimensional. It is performed on an image space by moving a window over the pixel points and replace the central pixel of the kernel with the median of the original grey levels within the window. The output image thus received is smoother than the original one.

The classical image smoothing or noise suppression is considered to adopt a low-pass filter and in many cases this is found to be a more appropriate procedure. However, in the case of remotely sensed satellite imagery, it could not yield the satisfactory results as it fails to preserve the most vulnerable feature of the image i.e. edges or lineaments. In certain situations median filtering is better and two of its main advantages are :

(1) It preserves sharp edges while linear low-pass filtering blurs such edges.

(2) It is very efficient for smoothing spiky noise. This property is illustrated in Fig. 4.1.

One-dimensional median filtering

The median filtering may be applied in one-dimension case by selecting a one-dimensional window and moving it on to the image space. Considering the size of the window as m with its members as x_1, \dots, x_m . These members are arranged in order and if m is odd then grey level corresponding to the middle number is designated as median and if m is even then median is computed as the mean of the two middle numbers.

Median of a sequence is expressed as $\text{Median}(x_1, \dots, x_m)$.

A median filter of size m on a sequence $x_i, i \in \mathcal{Z}$ and m being an odd number, is expressed as

$$y_i = \text{Median } x_i = \text{Median } (x_{i-v}, \dots, x_i, \dots, x_{i+v}), \quad i \in \mathcal{Z}. \quad (4.5)$$

where $v = (m - 1)/2$ and \mathcal{Z} corresponds to the set of all natural numbers. It is obvious from above definition that median filter preserves edges, whereas the corresponding moving average filter transforms an edge into a ramp of width m as shown by the following equation.

$$z_i = (x_{i-v} + \dots + x_i + \dots + x_{i+v})/m, \quad i \in \mathcal{Z} \quad (4.6)$$

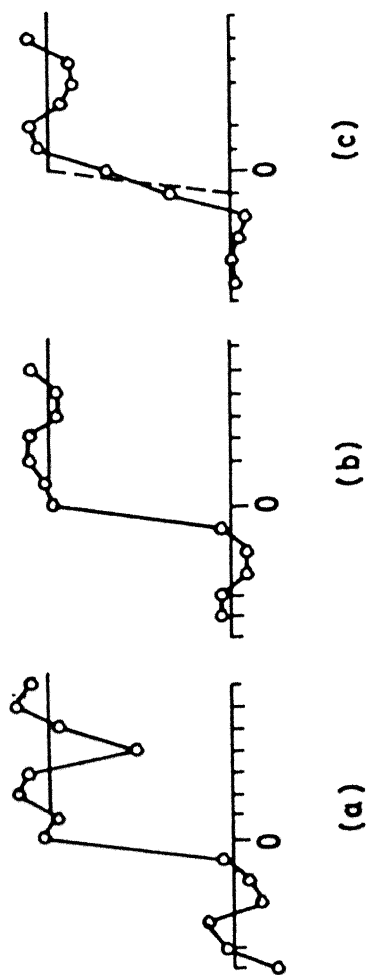


Fig. 4.1 (a) Edge plus noise signal (b) After median filtering
(c) After moving average filtering

Two-dimensional median filtering

In most of the image processing operations it is found that digital images are represented on a square grid by grey levels. A two-dimensional image is expressed as $f(x, y)$.

Where (x, y) lies on \mathcal{Z}^2 or subset of \mathcal{Z}^2 .

The image is considered two-dimensional with specific numbers of rows and columns as in the case of satellite imagery. For a filter window (A) of size $u \times v$, median of an image $f(x, y)$ is defined as

$$g(x, y) = \text{Median}\{f(x, y)\} = \text{Median}[f(x + u, y + v); (u, v) \in A], \quad (x, y) \in \mathcal{Z}^2 \quad (4.7)$$

The selection of the shape and size of the filter window depends on the anticipated feature classes present in the image. Windows may have a shape like line segments, squares, circles, crosses, square frames and circle rings. Some of these windows are shown in Fig. 4.2.

Edge preservation and noise reduction, the two important characteristics of the median filtering are explained below :

(a) Edge preservation by median filter

An edge or boundary in image processing gives an impression of an image in which all pixels on one side of the line have a common grey level value p and all points on the other side of the line have a another common value q , and $p \neq q$. Using this definition of edge, the edge preservation property of the median filter is presented by the following result :

If the median filter window set A is symmetric around the origin and includes the origin, i.e. if

$$(r, s) \in A \Rightarrow (-r, -s) \in A, \quad (4.8)$$

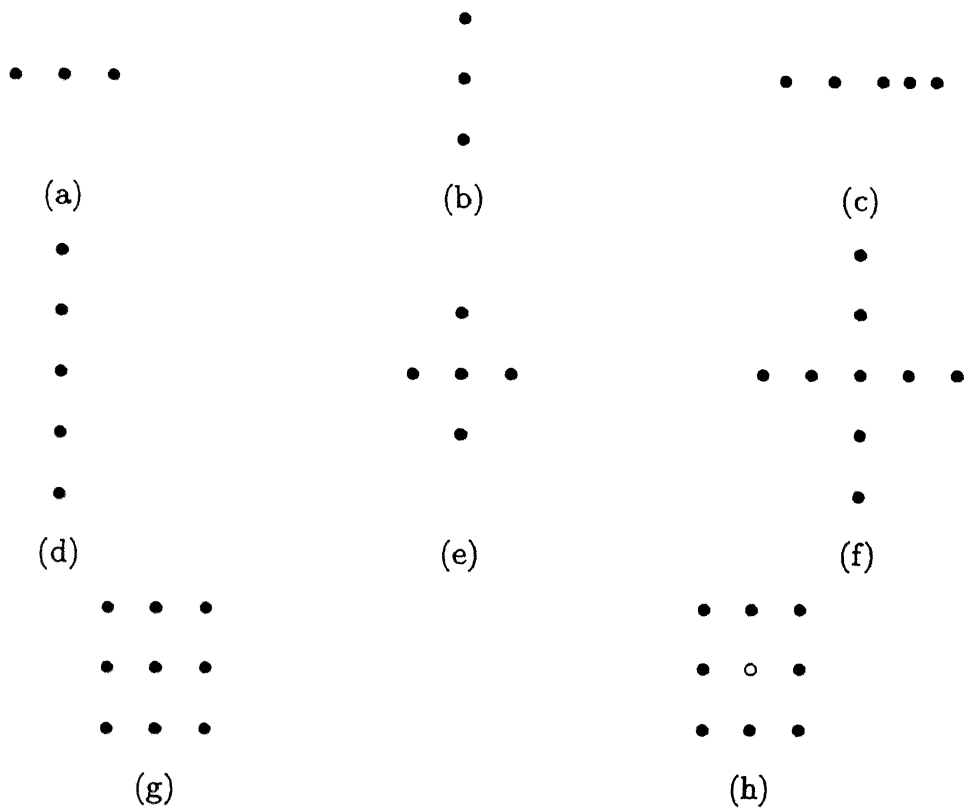


Fig. 4.2 Configuration of filter windows for median filtering;

- (a) Horizontal line segment (size 3); (b) Vertical line segment (size 3)
(c) Horizontal line segment (size 5); (d) Vertical line segment (size 5)
(e) Plus shape window (size 3); (f) Plus shape window (size 3);
(g) Plus shape window (size 3); (h) Plus shape window (size 5).

$$(0, 0) \in A, \quad (4.9)$$

then the median filter preserves any edge picture (Huang,1981). It should be noted here that these conditions imply that the number of points n in A is odd.

Since a symmetrical window is considered for filtering and median is being calculated within that window, it is obvious that boundary of the two regions will be preserved.

(b) Noise reduction by median filter

Basic aim of median filter is to suppress the noise. Pratt (1991) has discussed in rather qualitative way its effect on impulse noise. Fig. 4.3 illustrates some examples of the operation of a median filter and a moving average filter for a discrete step function, ramp function, pulse function and a triangle function with a window of size five. It is seen from these examples that median filter has the desirable property of not affecting step functions or ramp functions. Pulse functions with periods less than one-half the window width, are suppressed. But, the peak of the triangle is flattened.

Operation of the median filter can be analyzed qualitatively to a certain extent. The median of a product of a constant K and a sequence $f(j)$ is expressed (Pratt, 1991) as

$$\text{Median } [K\{f(j)\}] = K \text{ Median } \{f(j)\} \quad (4.10)$$

$$\text{Median } [K + f(j)] = K + \text{Median } \{f(j)\} \quad (4.11)$$

This result can also be generalized for two dimensional case $f(x, y)$ as follows:

$$\text{Median } [K\{f(x, y)\}] = K \text{ Median } \{f(x, y)\} \quad (4.12)$$

$$\text{Median } [K + f(x, y)] = K + \text{Median } \{f(x, y)\} \quad (4.13)$$

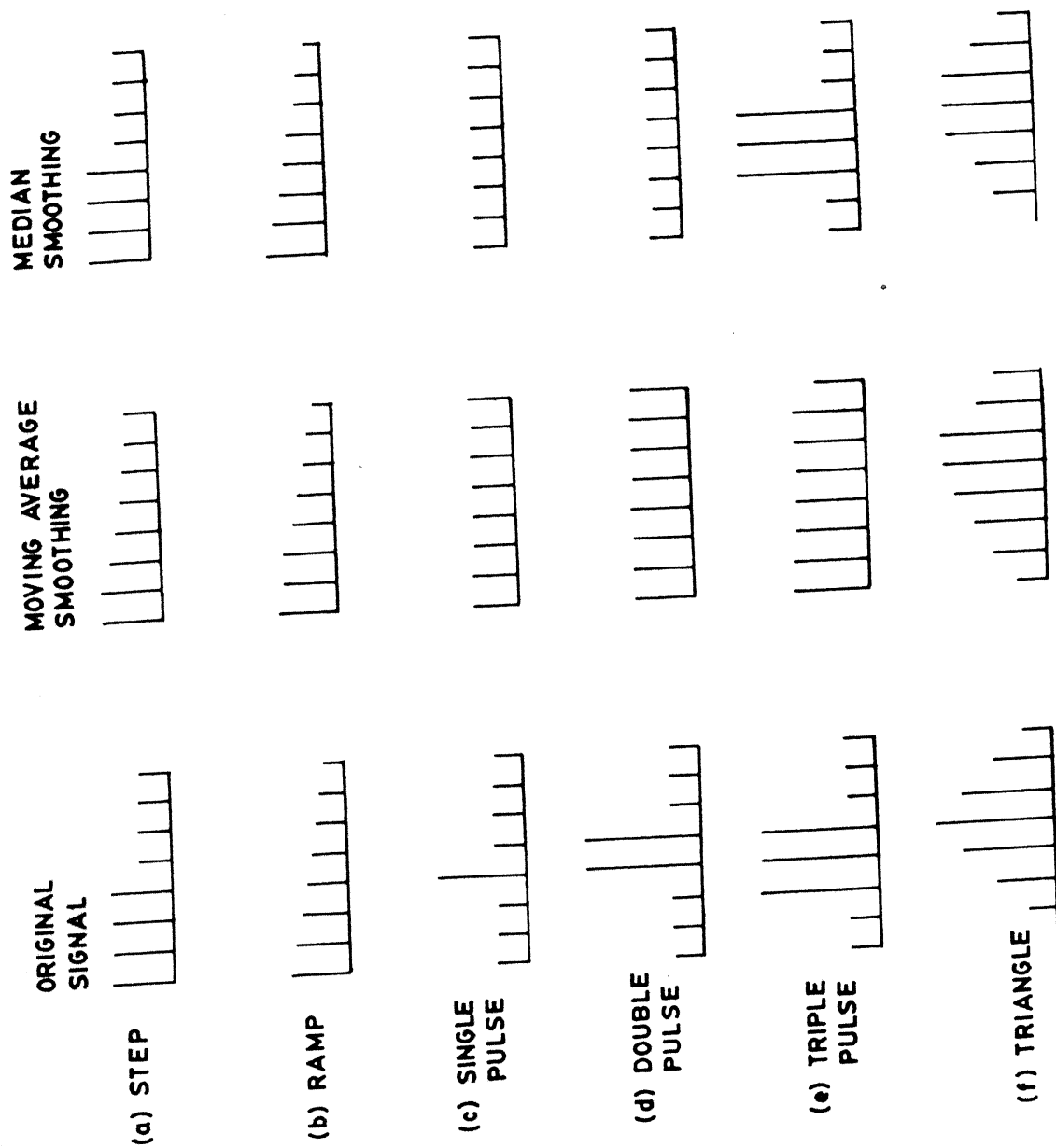


Fig. 4.3 Moving average and Median filtering on various test signals

Thus it is evident that salient details do not change when median is performed on the raw image or even on translated or transformed (by a factor K) image.

4.2.4 Pseudomedian filtering

In comparison to moving average filtering, the median filtering is found to be more efficient as far as edge preservation and the noise suppression are concerned. But its computational requirements are higher as number of operations, for every slide of the window, required are arranging members within the window in order, locating the middle number and replacing the central pixel by it. Number of computations increase if window size is increased. Attempts have been made by earlier workers to evolve various methods to attain high throughput using median filtering. Pratt (1984) evolved a filter known as the pseudomedian filter which possesses the properties of the median filter.

Consider the median of a five-element sequence x_1, x_2, x_3, x_4, x_5 which can be expressed as

$$\begin{aligned} \text{MED}(x_1, x_2, x_3, x_4, x_5) = & \text{MAX}[\text{MIN}(x_1, x_2, x_3), \text{MIN}(x_1, x_2, x_4), \\ & \text{MIN}(x_1, x_2, x_5), \text{MIN}(x_1, x_3, x_4), \\ & \text{MIN}(x_1, x_3, x_5), \text{MIN}(x_1, x_4, x_5), \\ & \text{MIN}(x_2, x_3, x_4), \text{MIN}(x_2, x_3, x_5), \\ & \text{MIN}(x_2, x_4, x_5), \text{MIN}(x_3, x_4, x_5)] \end{aligned}$$

or

$$\begin{aligned} \text{MED}(x_1, x_2, x_3, x_4, x_5) = & \text{MIN}[\text{MAX}(x_1, x_2, x_3), \text{MAX}(x_1, x_2, x_4), \\ & \text{MAX}(x_1, x_2, x_5), \\ & \text{MAX}(x_1, x_3, x_4), \text{MAX}(x_1, x_3, x_5), \text{MAX}(x_1, x_4, x_5), \\ & \text{MAX}(x_2, x_3, x_4), \text{MAX}(x_2, x_3, x_5), \text{MAX}(x_2, x_4, x_5), \\ & \text{MAX}(x_3, x_4, x_5)] \end{aligned} \quad (4.15)$$

It is found that for a sequence of size l , the median will be the MAX (or MIN) of the MIN (or MAX) of all $l! / [n!][(l - n)!]$ subsequences

where,

$$n = (l + 1)/2 \text{ and}$$

$$l! = l(l - 1) \dots 2.$$

For a specific case of a one-dimensional array of order five, psuedomedian is computed as follows :

$$\begin{aligned} \text{Pmed}(x_1, x_2, x_3, x_4, x_5) &= (1/2)\text{MAX}[\text{MIN}(x_1, x_2, x_3), \text{MIN}(x_2, x_3, x_4), \\ &\quad \text{MIN}(x_3, x_4, x_5)] \\ &+ (1/2)\text{MIN}[\text{MAX}(x_1, x_2, x_3), \text{MAX}(x_2, x_3, x_4), \\ &\quad \text{MAX}(x_3, x_4, x_5)] \end{aligned} \quad (4.16)$$

Considering the same array as above, ten possible subsequences of the order three are used for computing the median. But in the case of pseudomedian filtering only the three subsequences (x_1, x_2, x_3) , (x_2, x_3, x_4) and (x_3, x_4, x_5) are used. In this case the MIN followed by MAX in the first half of Equation 4.16 always gives the median of the array or a grey level which is smaller than the median, while the MAX followed by the MIN gives the median or a larger grey level value. The average of the two grey level values are then computed with a view to cancel the discrepancy, if any.

Pratt (1991) on the basis of an analysis with 120 possible arrangements of the five elements has indicated that in only eight of the cases the pseudomedian was found equal to the median. At the same time pseudomedian was never found more than the median by classical method in any arrangement. This indicates the effective elimination of the noise content, specially the spikes and stripping problem.

Let l_m denote an array of elements l_1, l_2, \dots, l_m . The pseudomedian of the array is

$$\text{Pmed}(l_m) = (1/2)\text{MAXIMIN}(l_m) + (1/2)\text{MINIMAX}(l_m) \quad (4.17)$$

Here the MAXIMIN the MINIMAX are computed as follows by considering a subsequence of the size n

where, $n = (m + 1)/2$

$$\begin{aligned} \text{MAXIMIN}(l_m) = & \text{MAX}[\text{MIN}(l_1, \dots, l_n), \\ & \text{MIN}(l_2, \dots, l_{n+1}), \\ & \dots, \text{MIN}(l_{m-n+1}, \dots, l_m)] \end{aligned} \quad (4.18)$$

and

$$\begin{aligned} \text{MINIMAX}(l_m) = & \text{MIN}[\text{MAX}(l_1, \dots, l_n), \\ & \text{MAX}(l_2, \dots, l_{n+1}), \\ & \dots, \text{MAX}(l_{m-n+1}, \dots, l_m)] \end{aligned} \quad (4.19)$$

Since in the present study two-dimensional image or array is being considered, it is essential to extend the one-dimensional pseudomedian concept to two-dimensional satellite image case in a simple way. Array of any shape such as rectangular, square or plus type can be chosen. While applying the MAX or MIN operations the resulting image is oversmoothed hence few details disappear compared to classical median filtering.

The application of a plus-shape pseudomedian generally provides a much better result in comparison to MAX and MIN operation or the classical median filtering approaches. While applying the pseudomedian filtering several configurations of the window shape and size were tried and it was realized that the plus shape window yields superior results and it is also computationally much faster.

Several windows selected for pseudomedian filtering are illustrated in the Fig. 4.4.

For a plus shaped window of a general size l , the pseudomedian is computed as follows :

$$\begin{aligned} P_{med} = & (1/2)\text{MAX}[\text{MAXIMIN}(p_l), \text{MAXIMIN}(q_l)] \\ & + (1/2)\text{MIN}[\text{MINIMAX}(p_l), \text{MINIMAX}(q_l)] \end{aligned} \quad (4.20)$$

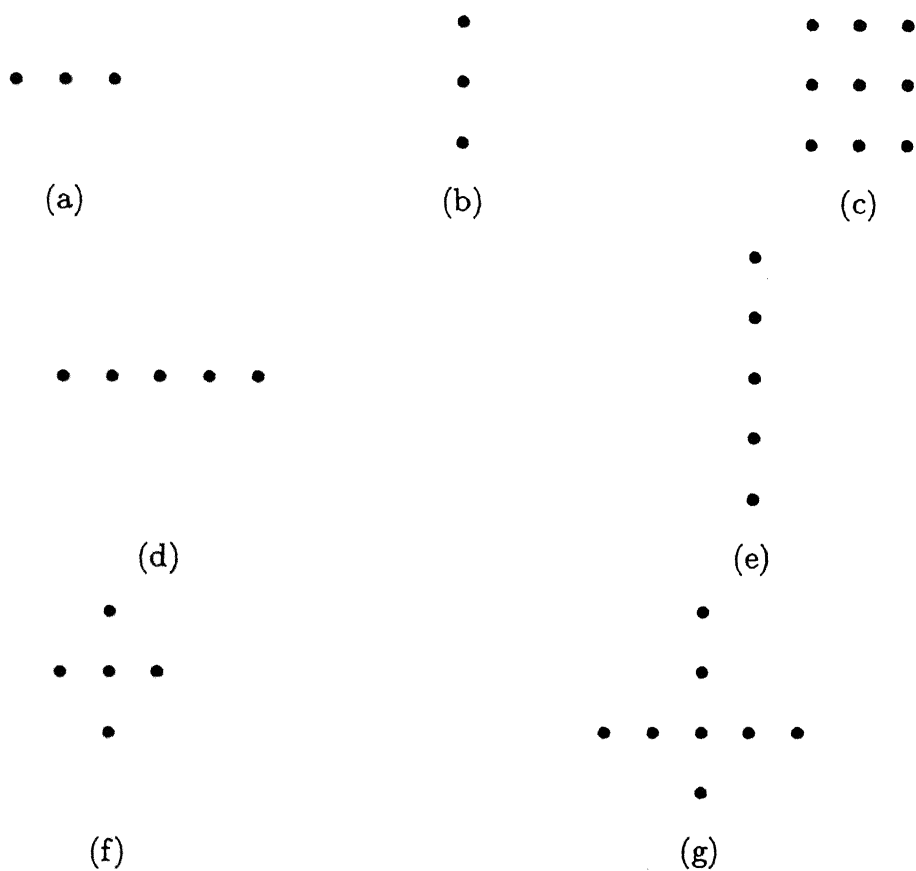


Fig. 4.4 Various window configurations utilized in performing pseudomedian filtering

- (a) Horizontal line segment (size 3), (b) Vertical line segment (size 3),
(c) Solid square (3×3), (d) Horizontal line segment (size 5),
(e) Vertical line segment (size 5), (f) Plus segment (5×5),
(g) Plus segment (size 5).

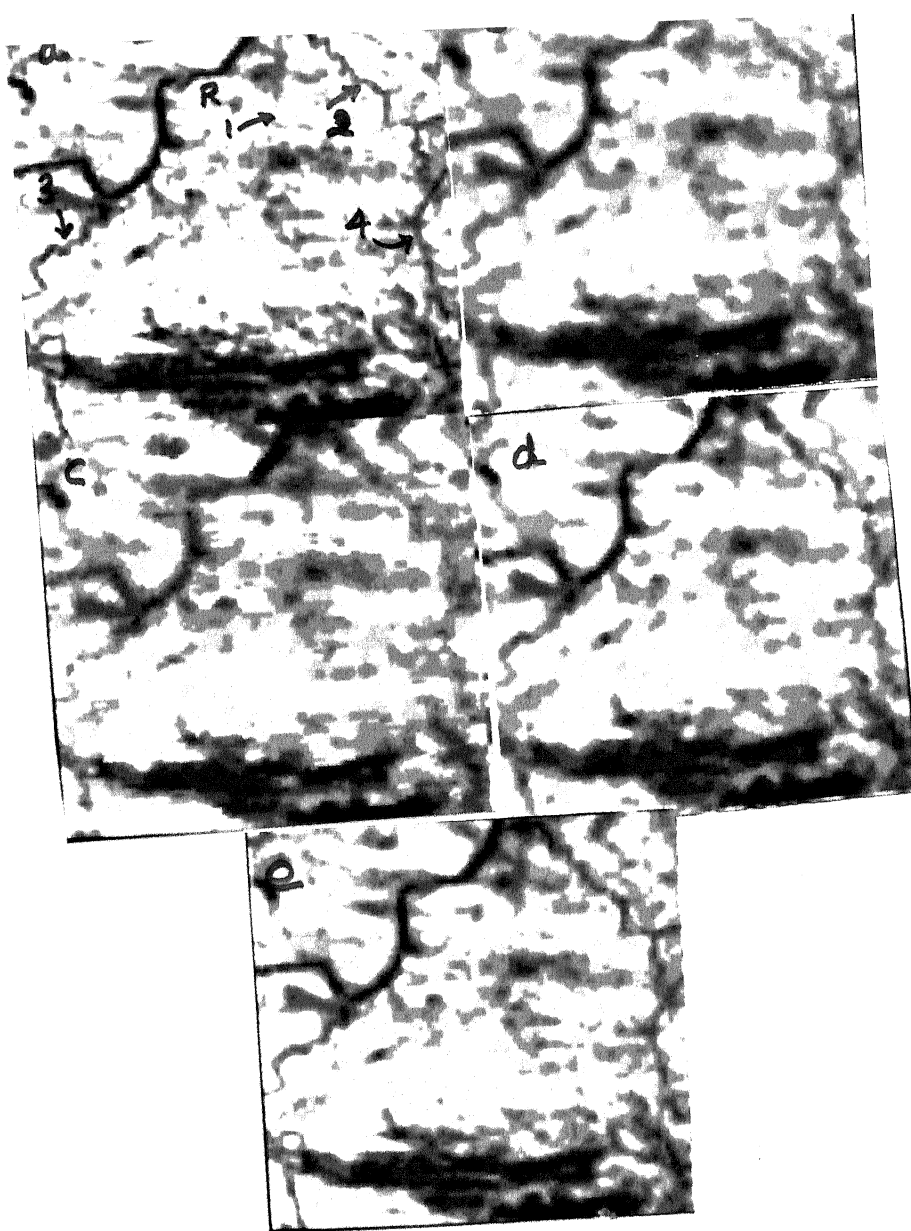


Fig. 4.5 Original test region (a) and its smoothed output for moving average filtering (b); sigma filtering (c); median filtering (d) and pseudomedian filtering (e).

where, p_i and q_i are grey levels for central row and central column.

It is found that the MAXIMIN operator in one or two-dimensional form is useful for removing bright spikes and impulse noise, but has little or no effect on dark spikes or impulse noise. On the other hand, the MINIMAX operator is very good at removing dark spikes or impulse noise, but not the bright ones. A solution to this problem was suggested as to cascade the operators (Pratt et al., 1984). The pseudomedian operator used here removes either of the noises very efficiently.

Out of various configurations the best results have been obtained in the case of plus shape window. Plus shape windows of sizes 3×3 and 5×5 are employed. The output obtained by these appear similar. In present case, a 3×3 size has been selected based on computational efficiency compared to a larger window.

Based on the above theoretical background and discussions it has been inferred that pseudomedian filtering will yield best smoothing result. For a visual assessment of these filtering techniques a small test region of the study area has been selected as shown in Fig. 4.5(a). The following smoothing filters found most suitable in each of the categories were applied on this test region: (a) Moving average filter (3×3) (b) Sigma filter (3×3) (c) Median filter (3×3) (d) Pseudomedian filter (Plus shape of size 3)

Outputs received after smoothing by these filters are shown in Fig. 4.5 (b), (c), (d), and (e). In the original image four linear features 1 (Railway line), 2 (tributary to river Bijul), 3 (tributary to river Bijul) and 4 (road) have been identified for assessing the effect of smoothing. It is evident that 1 has completely vanished in (b) and (c). Linear features 2 and 3 have become blurred in (b) and (c). Linear feature 4 is blurred in (b) but is lost in (c). In (d) and (e) images these features are preserved and smoothing is carried out effectively. A comparison of median filtered output (d) and pseudomedian filtered output (e) revealed that these linear features

appeared sharply in (e).

Therefore, based on the results of this experiment, Pseudomedian filtering has been found most suitable for the present case of remotely sensed images. The smoothing output received after applying a plus shape (size 3) pseudomedian filter is shown in Fig. 4.6.

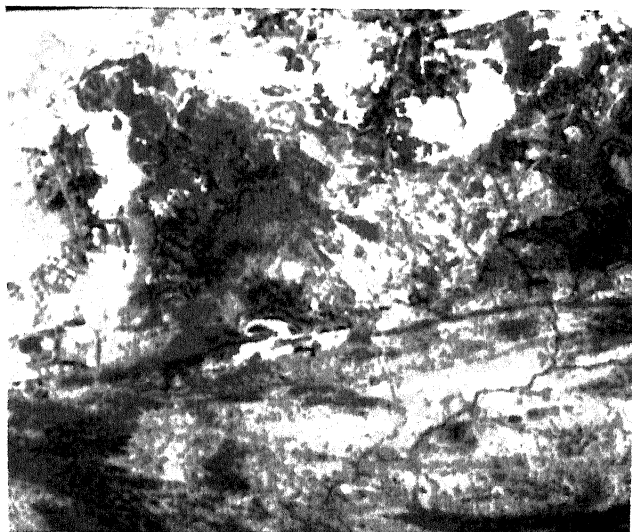


Fig. 4.6 Smoothened image using a 3×3 plus shape pseudomedian filtering

4.3 Edge Detection

In the present study the main objective is to enhance the image so that maximum structural details are revealed. Faults, fractures, joints and other lineaments can be identified easily if edges in an image are detected. A rich repertoire of tools are available in classical image processing which may filter out these edges or linear features. For the delineation of lineaments, quite often edge detection is carried out using Sobel operator, Laplacian operator and Roberts operator, without clearly justifying the basis of their selection for the concerned applications. Therefore, the main objective here is to choose the most appropriate edge detection algorithm for lineament detection.

In a grey level picture an edge is defined as the boundary between two regions of different constant grey levels. Edges, as conceived in image processing are generally of the following types : (Peli and Malah, 1982; Pratt et al., 1984)

- (1) Ideal step edge
- (2) Ideal roof edge
- (3) Ideal spike edge
- (4) Noisy edges superimposed on noisy image

Depending upon the class of image being analyzed, a variety of edge configurations exist. An illustration of various kinds of edges is presented in Fig. 4.7.

Edge detection algorithms may be broadly divided into two groups: parallel and sequential.

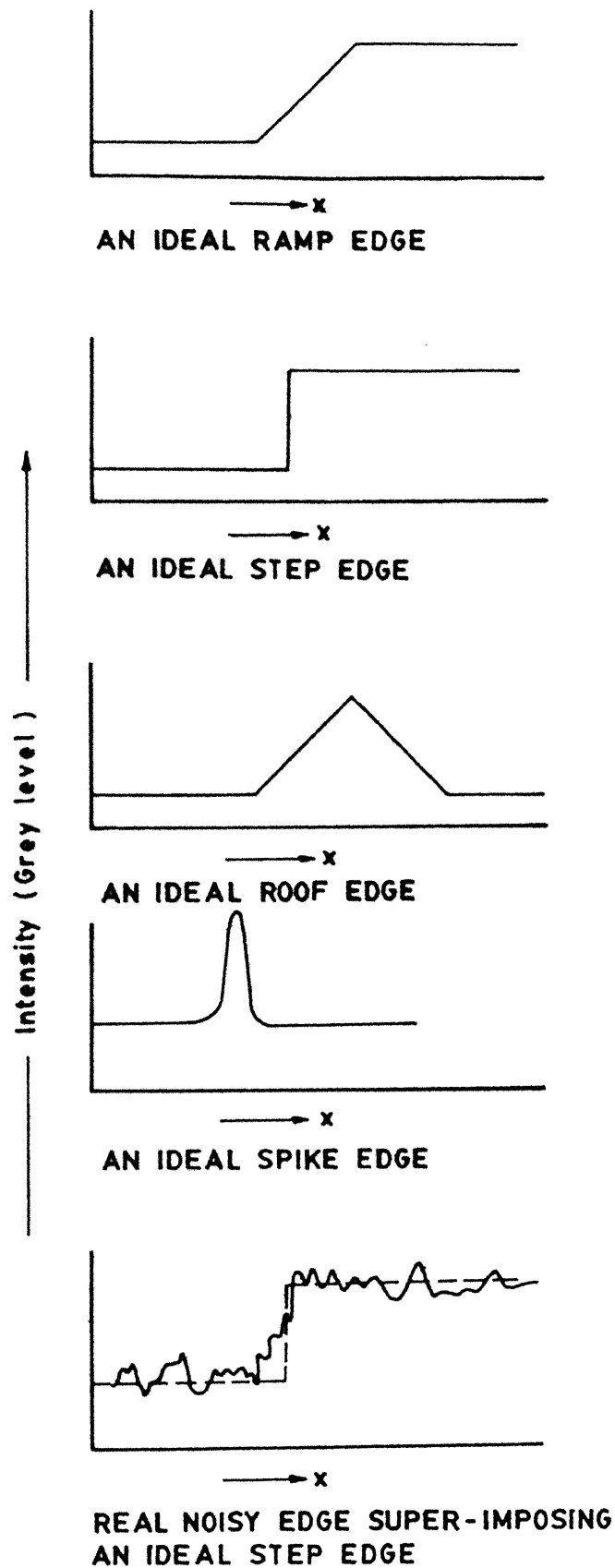


Fig.4-7 One-dimensional ideal and real edge signals

Parallel detection algorithms read and process all pixels of the image space simultaneously and output the obtained edges in parallel. In sequential detection algorithms, pixels are serially read and on the basis of neighborhood pixels, the pixels in consideration are assigned to either an edge or background domain (Smith and Davis, 1975).

Lineaments visible on satellite imagery are very useful from resource study point of view. Earlier, photo-interpreters job had been to identify relevant lineaments associated for various kind of application and prepare a map for further study. It has been felt over the years that image processing plays a significant role in making this process more reliable and efficient. With this in view several edge detectors have been used time and again. A large number of software packages are available based on common edge detection techniques. However, they often fail to serve the user in diverse image application requirements.

It has been seen that in several fields including remote sensing, workers have been using the filtering based on the concept of computing derivatives in an image. Other methods are also present such as frequency domain filtering, geometrical image processing, optical image processing and entropy based approaches. Filtering based on spatial derivative and entropy may be a viable option for remotely sensed imagery. In the following sections a detailed discussion and use of these algorithms are presented.

4.3.1 Derivative filtering

The edge detectors used here are based on the computation of derivatives in a small neighborhood of central pixel. This neighborhood can be selected depending

on type of image to be processed. The derivatives to be computed in these edge detectors are of the first and second order. These are discussed in detail in the following sections.

(a) First order derivative filtering

The operators based on this concept can be grouped into two categories. The first one involves computation of gradients in two orthogonal directions in an image. The other computes a set of directional derivatives. For a few of these operators, considered appropriate in present study, the details are as follows :

(i) Orthogonal gradient generation

In orthogonal gradient based methods, gradient in a small neighborhood of the image is evaluated in two orthogonal directions. Using these orthogonal components the magnitude and slope of the gradient are determined. In the case of a continuous image $f(x, y)$, an edge can be identified by forming the continuous one-dimensional gradient $g(x, y)$ along a line normal to the edge slope. The slope of this is at an angle α with respect to the horizontal axis. If the magnitude of gradient is sufficiently large, i.e., above a prespecified threshold value, an edge is deemed present otherwise not. The gradient along the line normal to the edge slope can be computed in terms of the derivatives along orthogonal axes as in the following equation

$$g(x, y) = \frac{\partial f(x, y)}{\partial x} \cos \alpha + \frac{\partial f(x, y)}{\partial y} \sin \alpha \quad (4.21)$$

Since images of concern in this chapter are discrete in nature, a scheme for computing the edges following the above method is presented in Fig. 4.8.

The magnitude of combined gradient is computed as follows :

$$g(x, y) = \left\{ [g_r(x, y)]^2 + [g_c(x, y)]^2 \right\}^{0.5} \quad (4.22)$$

where, $g_r(x, y)$ is row gradient and $g_c(x, y)$ is column gradient.

In the present study, the above equation is used for the magnitude of combined gradient. But several workers have used the following approximate formula for computational efficiency.

$$g(x, y) = |g_r(x, y)| + |g_c(x, y)| \quad (4.23)$$

The slope of the combined gradient with respect to the horizontal axes can be computed as follows :

$$\theta(x, y) = \tan^{-1} \left\{ \frac{g_c(x, y)}{g_r(x, y)} \right\} \quad (4.24)$$

Several operators have been proposed to accomplish the discrete domain differentiation approximating the above mentioned continuous differential equation with a view to provide a computationally efficient and better solution than the earlier methods.

One simple approach of extracting edges using derivative filtering is to compute running difference of pixels along rows and columns of the image. The row gradient and column gradients are defined (Jensen, 1986) as row gradient

$$g_r(x, y) = f(x, y) - f(x, y - 1) \quad (4.25)$$

column gradient :

$$g_c(x, y) = f(x, y) - f(x + 1, y) \quad (4.26)$$

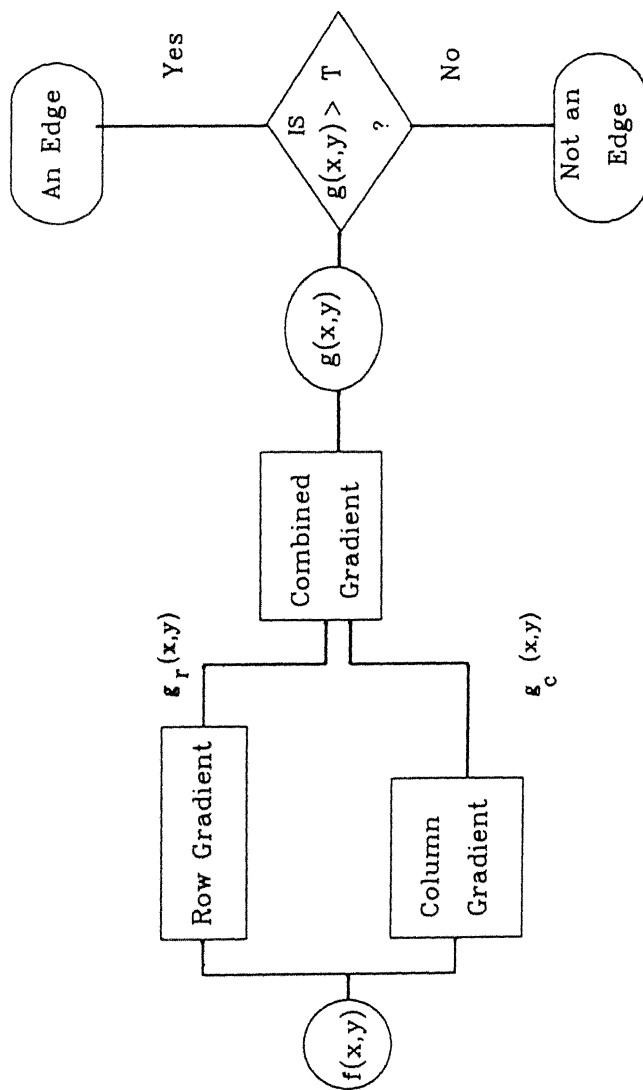


Fig. 4.8 Derivative filtering for edge detection

The row and column gradients are computed so as to ensure that g_r and g_c remain positive for an edge which increases in magnitude from left-to-right and from bottom-to-top in the discrete satellite images.

Of the two windows of size 2×2 and 3×3 , It has been observed that 3×3 provides advantage of increased smoothing over 2×2 . This makes the derivative operations less sensitive to the noise (Gonzalez and Wintz, 1977). Roberts operator of the size 2×2 , has been used by several workers in remote sensing but was not used for the reason stated above. A 3×3 edge gradient operator has been floated by Prewitt (1970) which can be described by the pixel numbering convention as shown below

$$\begin{pmatrix} a0 & a1 & a2 \\ a7 & f(x, y) & a3 \\ a6 & a5 & a4 \end{pmatrix}$$

The Prewitt square root edge gradient may be defined as

$$g(x, y) = \left\{ [g_r(x, y)]^2 + [g_c(x, y)]^2 \right\}^{0.5} \quad (4.27)$$

with row gradient component

$$g_r(x, y) = \frac{1}{k+2} \left[(a_2 + ka_3 + a_4) - (a_0 + ka_7 + a_6) \right] \quad (4.28)$$

and column gradient component

$$g_c(x, y) = \frac{1}{k+2} \left[(a_0 + ka_1 + a_2) - (a_6 + ka_5 + a_4) \right] \quad (4.29)$$

where $k = 1$.

In the above equation the row and column gradients are normalized to provide unit-gain positive weighted and unit gain negative weighted averages.

Sobel has proposed an orthogonal edge detector which differs from Prewitt edge detector in a way that the values of the north, south, east and west pixels are doubled, i.e., $k = 2$ (Duda and Hart, 1973). This has been done for the purpose of assigning equal weights to each pixel for its contribution to the gradient magnitude. An algorithm proposed by Frei and Chen (1977) has given weighting to north, south, east and west pixels by $k = \sqrt{2}$ so that the gradient is same for the horizontal, vertical, and diagonal edges. The advantage of the Frei-Chen edge detector is that the edge gradient is the same at the edge center for the single pixel transition vertical and diagonal ramp edge situation. In the case of Sobel, the gradient for diagonal edge is 1.06 and for Prewitt 0.94. Thus Sobel operator is very sensitive to diagonal edges than the Prewitt edge detector while the Prewitt edge detector is more sensitive to the horizontal and vertical edges than the diagonal edges. The Frei-Chen operator is equally efficient in the case of horizontal and vertical edges as well as for the diagonal edge case.

The computation of gradient as discussed above is linear in nature. This involves computation of row and column gradients, which can be represented by simple convolution operation.

$$g_r(x, y) = f(x, y) \odot h_r(x, y) \quad (4.30)$$

$$g_c(x, y) = f(x, y) \odot h_c(x, y) \quad (4.31)$$

where,

$h_r(x, y)$ and $h_c(x, y)$ are 3×3 row and column impulse response operators respectively and are illustrated for present image processing case in Fig. 4.9.

It has been realized that these operators provide noisy edges in a noisy image environment. This problem is alleviated by resorting to a larger window size. To incorporate this point, softwares are developed in a general way to adopt any user-specified window size. These kind of operators are also called as *boxcar operators*. In present context, a window size of 3×3 was selected and it has been observed that it yields satisfactory results. When resorted to a larger window dimension as in the case of *boxcar filters* the computation time has increased which makes the process highly uneconomical and at the same time some salient edges are left out.

Hence the choice has been narrowed to Frei-Chen 3×3 derivative filtering.

Thresholding

Large number of false edges appear when an edge detector is applied. Although the data image is smoothed to suppress scattered noise from the image space still some eddies and other tiny edge contours appear. To make the interpretation easier, insignificant edges must be eliminated. This was achieved in the present case using selective thresholding. Threshold calculation is based on the standard deviation for each of the filter window. This standard deviation is updated with each shifting of the window. The threshold is calculated as :

$$T = \mu + K \times \sigma \quad (4.32)$$

Roberts:

Row Gradient

$$\begin{pmatrix} 0 & 0 & -1 \\ 0 & 1 & 0 \\ 0 & 0 & 0 \end{pmatrix}$$

Column Gradient

$$\begin{pmatrix} -1 & 0 & 0 \\ 0 & 1 & 0 \\ 0 & 0 & 0 \end{pmatrix}$$

Prewitt :

Row Gradient

$$\frac{1}{3} \begin{pmatrix} 1 & 0 & -1 \\ 1 & 0 & -1 \\ 1 & 0 & -1 \end{pmatrix}$$

Column Gradient

$$\frac{1}{3} \begin{pmatrix} -1 & -1 & -1 \\ 0 & 0 & 0 \\ 1 & 1 & 1 \end{pmatrix}$$

Sobel :

Row Gradient

$$\frac{1}{4} \begin{pmatrix} 1 & 0 & -1 \\ 2 & 0 & -2 \\ 1 & 0 & -1 \end{pmatrix}$$

Column Gradient

$$\frac{1}{4} \begin{pmatrix} -1 & -2 & -1 \\ 0 & 0 & 0 \\ 1 & 2 & 1 \end{pmatrix}$$

Frei-Chen :

Row Gradient

$$\frac{1}{2 + \sqrt{2}} \begin{pmatrix} 1 & 0 & -1 \\ \sqrt{2} & 0 & -\sqrt{2} \\ 1 & 0 & -1 \end{pmatrix}$$

Column Gradient

$$\frac{1}{2 + \sqrt{2}} \begin{pmatrix} -1 & -\sqrt{2} & -1 \\ 0 & 0 & 0 \\ 1 & \sqrt{2} & 1 \end{pmatrix}$$

Fig. 4.9 : Impulse response operators used in orthogonal derivative gradient edge detection

where,

T : threshold,

μ : mean of the window pixel grey levels,

K : coefficient by the user and

σ : standard deviation for window pixel grey levels.

Computation of the magnitude of the gradient is followed by threshold computation, which is again followed by a decision making process of assigning the central pixel to edge domain or to background. If magnitude of the gradient is greater than the threshold then the central pixel is assigned to the edge pixel domain, otherwise it is not.

Based on the methodologies discussed above Frie-Chen, Prewitt and Sobel 3×3 operators are applied on the image of a test region of the study area. The edge output received are shown in Figs. 4.10 (a), (b), and (c) respectively.

It is seen that a large number of noisy edge contours appear in b and c. A small rectangle shown by green arrow has come out as hollow in a but is filled in b and c. This made it clear that Frie-Chen operator has filtered the internal edges more accurately than Prewitt and Sobel operator. A vertical edge (3-B and lower part of 3-C) has been filtered very sharply in a than in other two images. An overall inspection suggested that edges found by applying Frie-chen operator were thin and sharp while other two rendered thick edges. For lineament mapping a sharp edge is preferred.

Therefore, the result obtained in this experiment suggested to adopt Frie-Chen operator for edge detection in present context. An edge image received after employing this operator is shown in Fig. 4.11.

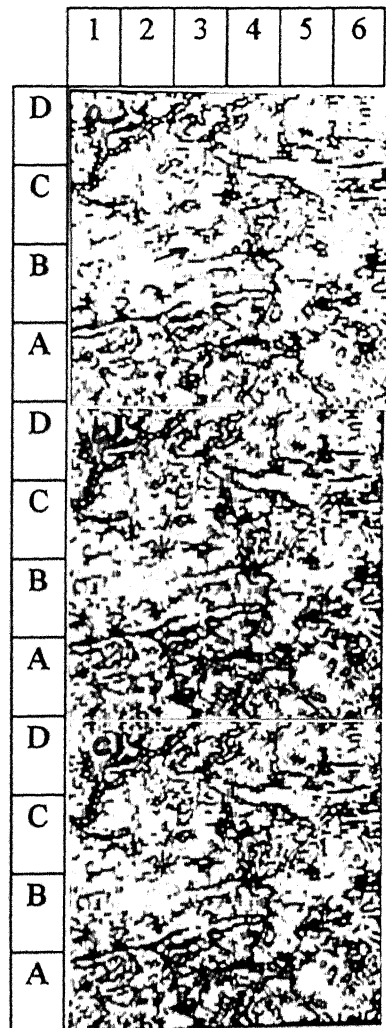


Fig. 4.10 Edge detection output using first order orthogonal derivative filtering on an image subregion of the area (a) Frei-Chen operator (b) Prewitt operator (c) Sobel operator



Fig. 4.11 Edge detection using orthogonal derivative filtering by Frei-Chen operator

(ii) Directional gradient filtering

Geological features are generally of irregular shape. Structural features are commonly linear or curvilinear. Often they are oriented in few preferred directions within the region. Directional aspect thus is very important. If prior information regarding the direction is available it is easier to design or adopt a suitable filter. Generally this information can be obtained in the field or from available geological maps. If access to such information is not possible then the only choice left is to test the filters of all possible orientation.

In the previous section, the orthogonal edge gradient methods have been discussed. Here a different approach suggested by several researchers is adopted which is to compute gradients in several directions. This method is also known as edge template gradient generation. It is accomplished by convolution of a digital image with a set of directional edge templates. The edge template gradient is expressed as

$$g(x, y) = \text{MAX}[|g_1(x, y)|, \dots, |g_i(x, y)|, \dots, |g_n(x, y)|] \quad (4.33)$$

where,

$$g_i(x, y) = f(x, y) \odot h_i(x, y) \quad (4.34)$$

is the gradient in the i^{th} direction which is computed by convolving an image with a gradient impulse response array $h_i(x, y)$. Out of all the directional gradients computed for each of the setting of window in the image space the edge direction is computed by the direction of the maximum gradient. Prewitt (1970) has suggested compass gradient operator which is gain-normalized. Kirsch (1971)

has proposed a 3×3 directional gradient operator using modulo 7 operation

$$g(x, y) = \text{MAX}_{i=0}^{i=7} \left[|5p_i - 3q_i| \right] \quad (4.35)$$

where,

$$p_i = a_i + a_{i+1} + a_{i+2} \quad (4.36)$$

and

$$q_i = a_{i+3} + a_{i+4} + a_{i+5} + a_{i+6} + a_{i+7} \quad (4.37)$$

Here, the pixel numbering convention is same as in the Section 4.3.1. Robinson (1977) has proposed 3-level and 5-level directional template gradients. The 3-level Robinson operator is derived after the Prewitt operator and the 5-level Robinson operator is derived after the Sobel operator. In this study an application of Prewitt's compass gradient, Kirsch directional gradient, Robinson 3-level and Robinson 5-level directional gradient have been applied with an assumption that there is no knowledge base regarding lineament orientation available for the area into consideration. Directional gradient templates are shown in Figs. 4.12 to 4.15. These gradient templates have been utilised to produce the edge images. It is found that edges received in all the four images were similar except the noisy edge contours received in the case of Prewitt compass gradient and Robinson 3-level directional gradient. The edge output received by the Kirsch directional gradient and the Robinson 5-level direction gradient is shown in Figs. 4.16 and 4.17. Large number of edges appear in these images which may be utilised for lineament map-

ping in case of remotely sensed images in association with available ground truth informations such as geological and topographical maps.

(b) Second order derivative filtering

In the case of second order derivative the edges appear more prominently than first order derivative filtering (Gonzalez and Wintz, 1977). While taking the second derivative at boundaries or edges, it is found that extraordinary change occurs in magnitude or in sign of the derivative. Two types of second order derivative methods are available

- (i) Laplacian and
- (ii) Directed second order derivative.

(i) Laplacian operator

This impulse response operator is based on second order derivative concept and is rotation invariant. When applied in the continuous domain $f(i, j)$ signal case, the Laplacian can be expressed as follows :

$$f_L(i, j) = -\nabla^2 \left\{ f(i, j) \right\} \quad (4.38)$$

where,

$$\nabla^2 = \frac{\partial^2}{\partial i^2} + \frac{\partial^2}{\partial j^2} \quad (4.39)$$

East (h_1)

$$\frac{1}{5} \begin{pmatrix} 1 & 1 & -1 \\ 1 & -2 & -1 \\ 1 & 1 & -1 \end{pmatrix}$$

Northeast (h_2)

$$\frac{1}{5} \begin{pmatrix} 1 & -1 & -1 \\ 1 & -2 & -1 \\ 1 & 1 & 1 \end{pmatrix}$$

North (h_3)

$$\frac{1}{5} \begin{pmatrix} -1 & -1 & -1 \\ 1 & -2 & 1 \\ 1 & 1 & 1 \end{pmatrix}$$

Northwest (h_4)

$$\frac{1}{5} \begin{pmatrix} -1 & -1 & 1 \\ -1 & -2 & 1 \\ 1 & 1 & 1 \end{pmatrix}$$

West (h_5)

$$\frac{1}{5} \begin{pmatrix} -1 & 1 & 1 \\ -1 & -2 & 1 \\ -1 & 1 & 1 \end{pmatrix}$$

Southwest (h_6)

$$\frac{1}{5} \begin{pmatrix} 1 & 1 & 1 \\ -1 & -2 & 1 \\ -1 & -1 & 1 \end{pmatrix}$$

South (h_7)

$$\frac{1}{5} \begin{pmatrix} 1 & 1 & 1 \\ 1 & -2 & 1 \\ -1 & -1 & -1 \end{pmatrix}$$

Southeast (h_8)

$$\frac{1}{5} \begin{pmatrix} 1 & 1 & 1 \\ 1 & -2 & -1 \\ 1 & -1 & -1 \end{pmatrix}$$

Fig. 4.12 Directional gradient templates for the Prewitt compass
gradient method

East (h_1)

$$\frac{1}{15} \begin{pmatrix} 5 & -3 & -3 \\ 5 & 0 & -3 \\ 5 & -3 & -3 \end{pmatrix}$$

Northeast (h_2)

$$\frac{1}{15} \begin{pmatrix} -3 & -3 & -3 \\ 5 & 0 & -3 \\ 5 & 5 & -3 \end{pmatrix}$$

North (h_3)

$$\frac{1}{15} \begin{pmatrix} -3 & -3 & -3 \\ -3 & 0 & -3 \\ 5 & 5 & 5 \end{pmatrix}$$

Northwest (h_4)

$$\frac{1}{15} \begin{pmatrix} -3 & -3 & -3 \\ -3 & 0 & 5 \\ -3 & 5 & 5 \end{pmatrix}$$

West (h_5)

$$\frac{1}{15} \begin{pmatrix} -3 & -3 & 5 \\ -3 & 0 & 5 \\ -3 & -3 & 5 \end{pmatrix}$$

Northeast (h_6)

$$\frac{1}{15} \begin{pmatrix} -3 & 5 & 5 \\ -3 & 0 & 5 \\ -3 & -3 & -3 \end{pmatrix}$$

South (h_7)

$$\frac{1}{15} \begin{pmatrix} 5 & 5 & 5 \\ -3 & 0 & -3 \\ -3 & -3 & -3 \end{pmatrix}$$

Southeast (h_8)

$$\frac{1}{15} \begin{pmatrix} 5 & 5 & -3 \\ 5 & 0 & -3 \\ -3 & -3 & -3 \end{pmatrix}$$

55

**Fig. 4.13 Directional gradient templates for the Kirsch
gradient method**

East (h_1)

$$\frac{1}{4} \begin{pmatrix} 1 & 0 & -1 \\ 2 & 0 & -2 \\ 1 & 0 & -1 \end{pmatrix}$$

Northeast (h_2)

$$\frac{1}{4} \begin{pmatrix} 0 & -1 & -2 \\ 1 & 0 & -1 \\ 2 & 1 & 0 \end{pmatrix}$$

North (h_3)

$$5\frac{1}{4} \begin{pmatrix} -1 & -2 & -1 \\ 0 & 0 & 0 \\ 1 & 2 & 1 \end{pmatrix}$$

Northwest (h_4)

$$\frac{1}{4} \begin{pmatrix} -2 & -1 & 0 \\ -1 & 0 & 1 \\ 0 & 1 & 2 \end{pmatrix}$$

West (h_5)

$$\frac{1}{4} \begin{pmatrix} -1 & 0 & 1 \\ -2 & 0 & 2 \\ -1 & 0 & 1 \end{pmatrix}$$

Northeast (h_6)

$$\frac{1}{4} \begin{pmatrix} 0 & 1 & 2 \\ -1 & 0 & 1 \\ -2 & -1 & 0 \end{pmatrix}$$

South (h_7)

$$\frac{1}{4} \begin{pmatrix} 1 & 2 & 1 \\ 0 & 0 & 0 \\ -1 & -2 & -1 \end{pmatrix}$$

Southeast (h_8)

$$\frac{1}{4} \begin{pmatrix} 2 & 1 & 0 \\ 1 & 0 & -1 \\ 0 & -1 & -2 \end{pmatrix}$$

**Fig. 4.15 Directional gradient templates for the Robinson
5-level gradient method**

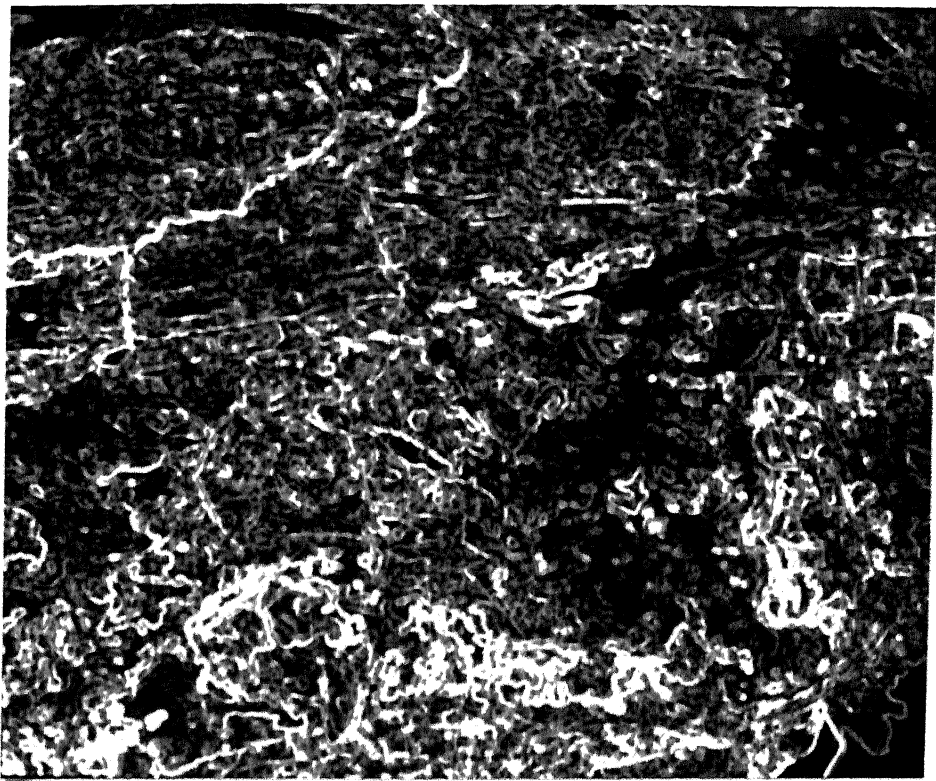
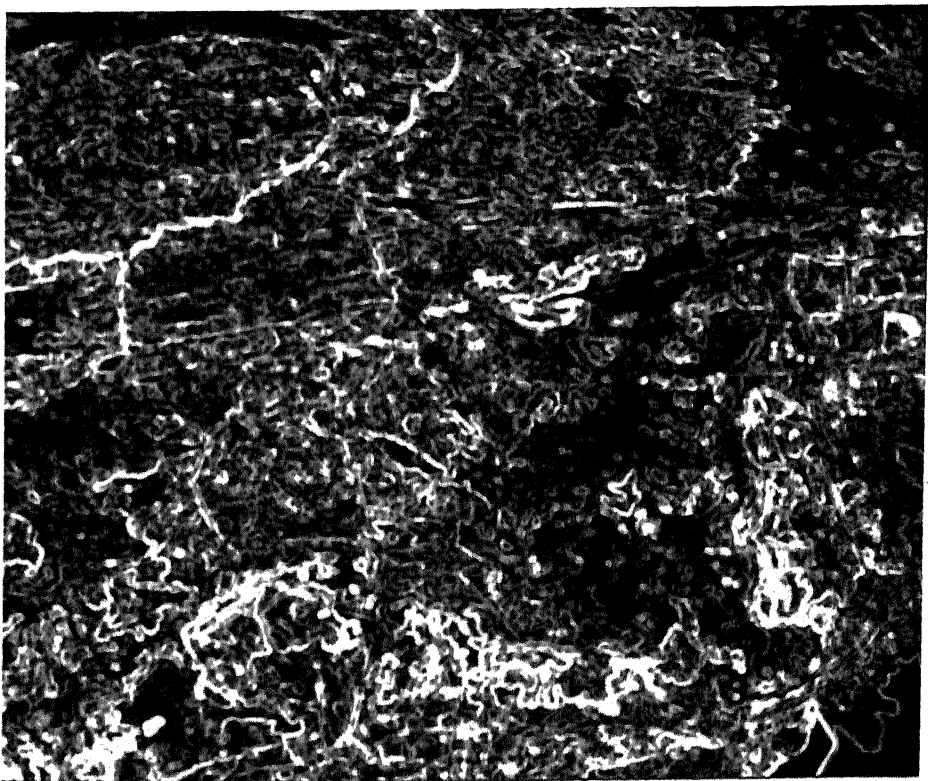


Fig. 4.16 Edge detected image using the Kirsch gradient



The magnitude of Laplacian $f_L(i, j)$ is zero if $f(i, j)$ is constant or changing in a linear manner.

If the rate of change of $f(i, j)$ is greater than linear, $f_L(i, j)$ exhibits a sign transformation at the point of inflexion of $f(i, j)$. This point is called as the zero crossing of $f_L(i, j)$ and manifests the presence of an edge. The negative sign has been incorporated in the Expression 4.38 so that zero crossing of $f_L(i, j)$ should invariably possess a positive slope for an edge whose amplitude increases from left-to-right and from bottom-to-top in an image (Pratt, 1991). This operator can easily be applied to the case of discrete remote sensing imagery by computing difference of gradients along each axis. Mathematically, this is expressed as

$$f_L(x, y) = \left[f(x, y) - f(x, y - 1) \right] - \left[f(x, y + 1) - f(x, y) \right] + \left[f(x, y) - f(x + 1, y) \right] - \left[f(x - 1, y) - f(x, y) \right] \quad (4.40)$$

Since this process is essentially performed by convolution it can be represented as

$$f_L(x, y) = f(x, y) \odot h(x, y) \quad (4.41)$$

with,

$$h = \begin{pmatrix} 0 & 0 & 0 \\ -1 & 2 & -1 \\ 0 & 0 & 0 \end{pmatrix} + \begin{pmatrix} 0 & -1 & 0 \\ 0 & 2 & 0 \\ 0 & -1 & 0 \end{pmatrix} \quad (4.42)$$

or

$$h = \begin{pmatrix} 0 & -1 & 0 \\ -1 & 4 & -1 \\ 0 & -1 & 0 \end{pmatrix} \quad (4.43)$$

A four neighbor 3×3 Laplacian which is also normalized to unit gain is expressed as

$$h = \frac{1}{4} \begin{pmatrix} 0 & -1 & 0 \\ -1 & 4 & -1 \\ 0 & -1 & 0 \end{pmatrix} \quad (4.44)$$

Prewitt has suggested an eight-neighbor Laplacian, defined by the unit gain normalized impulse response operator, as

$$h = \frac{1}{8} \begin{pmatrix} -1 & -1 & -1 \\ -1 & 8 & -1 \\ -1 & -1 & -1 \end{pmatrix} \quad (4.45)$$

This array is not separable into a sum of second derivatives as in Equation 4.42. A eight-neighbor Laplacian impulse response operator which is separable in nature can be expressed as

$$h = \begin{pmatrix} -1 & 2 & -1 \\ -1 & 2 & -1 \\ -1 & 2 & -1 \end{pmatrix} + \begin{pmatrix} -1 & -1 & -1 \\ 2 & 2 & 2 \\ -1 & -1 & -1 \end{pmatrix} \quad (4.46)$$

The gain normalized separable eight neighbour Laplacian impulse response operator is represented as

$$h = \frac{1}{8} \begin{pmatrix} -2 & 1 & -2 \\ 1 & 4 & 1 \\ -2 & 1 & -2 \end{pmatrix} \quad (4.47)$$

It has been reported earlier (Heurtas and Medioni, 1986; Pratt, 1991) for the response of Laplacian operator in discrete image case that the zero crossings do not always lie at pixel sample location. As remotely sensed imagery are occasionally subjected to solar luminance variability hence they have ramp edges of varying

slopes. Due to this zero valued Laplacian response do not occur many times which makes detection of edges difficult.

A simple approach to detect Laplacian zero crossing in discrete domain is to find maximum of all positive Laplacian responses and minimum of all negative Laplacian responses in a 3×3 window. If the magnitude of the difference between the maxima and the minima exceeds a threshold, an edge is adjudged present. The Laplacian operator is sensitive to the grey level jump but it is considered over-sensitive to the noise in the image domain (Gonzalez and Wintz, 1977). Due to this nature, it is less utilized in edge detection. It is considered useful only for preliminary edge detection. Hence, this operator is applied on the study area data set, only for giving a broad idea of the lineament fabric.

A separable eight neighbor gain normalized Laplacian operator is applied on the original image and the output edge image is illustrated in Fig. 4.18.

(ii) Directed second order derivative generation

In above discussion of Laplacian operator, rotationally invariant second order derivative has been employed to ascertain the existence of an edge. The direction of an edge may be determined during zero crossing detection process. In this section, an alternate approach to first estimate the edge direction, and then compute the one-dimensional second order derivative along the edge direction is presented. The directed second order derivative of a continuous domain image $f(i, j)$ along a line at an angle ϕ with respect to horizontal axis is given by

$$f''(u, v) = \frac{\partial^2 f(u, v)}{\partial u^2} \cos^2 \phi + \frac{\partial^2 f(u, v)}{\partial u \partial v} \sin \phi \cos \phi + \frac{\partial^2 f(u, v)}{\partial v^2} \sin^2 \phi \quad (4.48)$$

Directed second order derivative is a non-linear operator. Therefore, con-

volution of a smoothing operator over $f(u, v)$ before differentiation process is not equivalent to convolving the directed second order derivative of $f(u, v)$ with the smoothing function.

The main problem with this filter is to have the knowledge base of the slope of edge domain pixels. This can be solved by selecting a suitable first order derivative filter and determining the slope. Selection of an appropriate filter itself is a difficult task. Once the probable slope of the edge pixel is determined then above equation which is applicable only for continuous signal case is approximated for the discrete image case.

The edge direction can be determined for each of the neighborhood case but the problem arises in approximating the continuous function $f(u, v)$. In the absence of any strong methodology to implement this procedure for discrete images, it was decided to select only the Laplacian second order approach out of the two available second order derivative filtering techniques for lineament detection.

4.3.2 Edge detection based on image entropy

Edges are characterized by sudden variation of grey level values in an image space. Remotely sensed images having large number of structural features, may be characterized by a random model involving a large family of such edge pixels scattered in an image. Derivative filters discussed above are generally employed for detecting the edges. They generally show larger magnitude of gradient in a zone of sudden variation of grey level information. Other schemes for edge detection not involving the derivative filtering approaches are also available in literature (Pratt, 1978; Rosenfield and Kak, 1982).

In this section, an approach based on the entropy of the image is employed

for edge detection in remotely sensed imagery. Entropy of the image in a predefined small neighborhood of the global image is computed which yields low values in the areas where the grey level values are going through rapid variation rather abruptly (Shiozaki, 1983). Edges are characterized by sudden variation in the grey levels hence they are located in the areas where the entropy is small. The edges may thus be filtered out from background by operating the entropy operator throughout an image and detect the areas where the entropy is small.

The entropy based approach provides is a non-linear spatial filter. It evaluates the entropy of the image grey level values in a small neighborhood centered at the $(r, s)^{\text{th}}$ pixel. The configuration of pixels in a window is as follows :

$$\begin{pmatrix} a_1 & a_2 & a_3 \\ a_8 & a_0 & a_4 \\ a_7 & a_6 & a_5 \end{pmatrix}$$

Let the grey levels of the $(r, s)^{\text{th}}$ pixel and the n neighbouring pixels is $a_0, a_1, a_2, \dots, a_n$, respectively.

Then the entropy E of the brightness in the region is defined as follows :

$$E = -\frac{\sum_{i=0}^n p_i \log p_i}{\log(n+1)} \quad (4.49)$$

where

$$p_i = \frac{a_i}{\sum_{j=0}^n a_j} \quad (4.50)$$

The techniques of edge detection discussed in previous sections such as the first order edge detection and second order edge detection utilize the basic concept of *rate of change of pixel grey level values* in a local neighborhood. They are not dependent on the average grey level value of that local region. When entropy of

the image sub-region is determined both these factors are taken into account which make this algorithm more reliable. However, this aspect makes it computationally slow. In the present study different window sizes are considered to understand the effect of size of neighborhood in extracting the edge pixels. Sizes of neighborhood considered are 3×3 , 5×5 and 7×7 . It is found that 3×3 neighborhood gives better response in comparison to other selected window sizes. The efficiency of entropy based method decreases with the increase in window size. In case of 7×7 entropy filter, the number of edges were less compared to 3×3 and 5×5 . Therefore edge output using 3×3 window size is selected for presented work which is shown in Fig. 4.19.

The entropy operator is highly susceptible to the noise. Therefore the image must be smoothed before edge detection to eliminate noise.

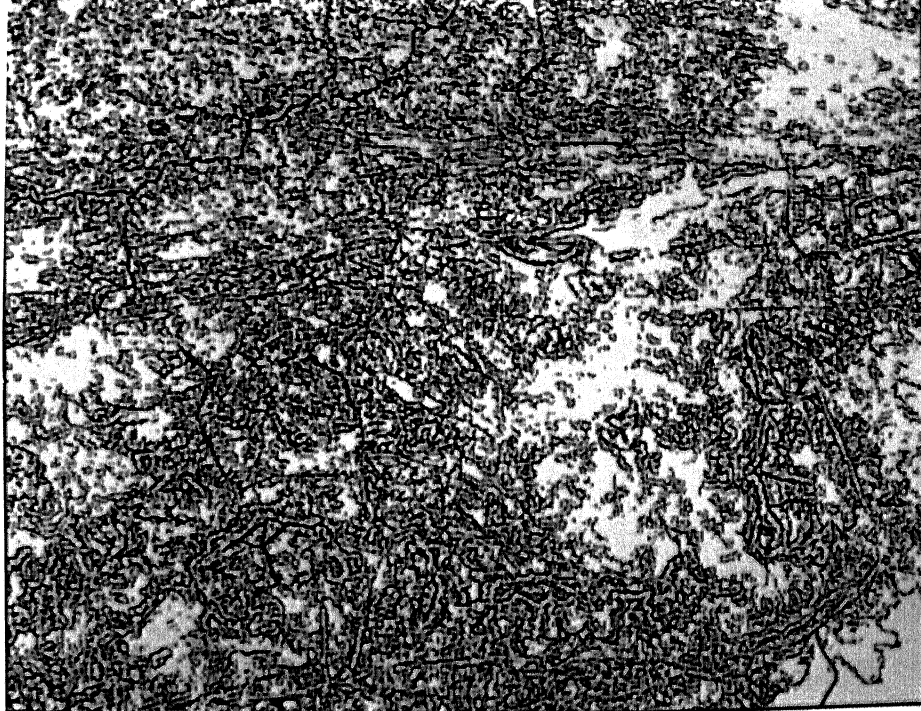


Fig. 4.18 Edge detected image using Laplacian eight neighbour,

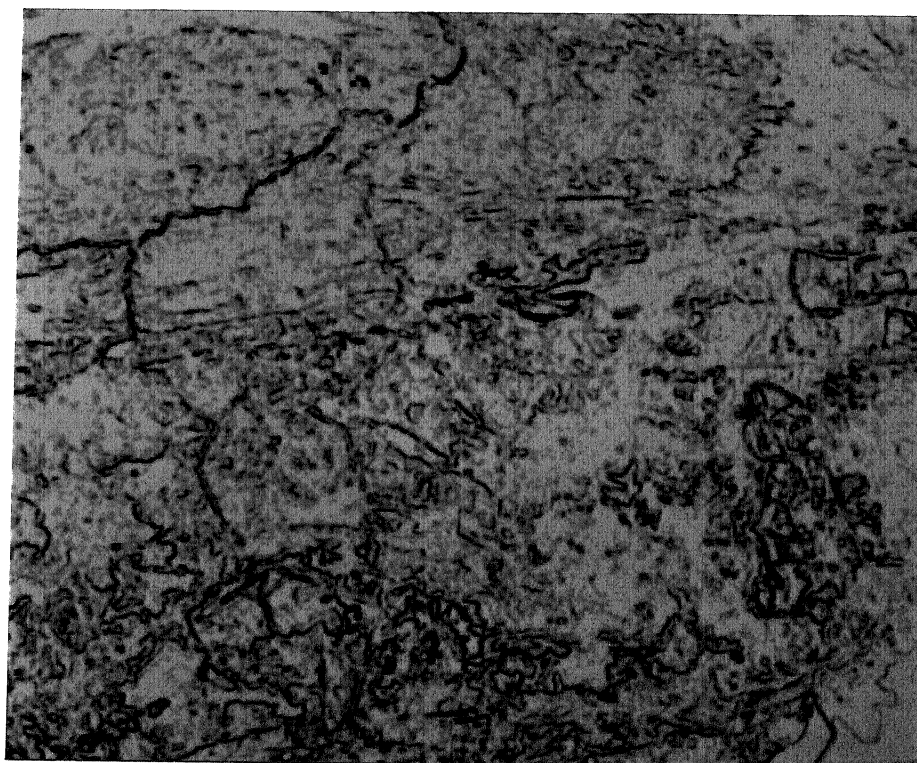


Fig. 4.19 Edge detection using non-linear entropy 3×3 operator

4.4 Edge Linking

In previous section, edge or lineament detection techniques have been discussed and it is found that all of them are based on detection of illumination discontinuities. They detect pixels lying at the boundary of background and the object or between two objects. In the case of remote sensing imagery this concept is not applicable, because of presence of noise, break in boundary due to topographical or nonuniform illumination situation and various other effects that induce spurious intensity discontinuities.

Due to this, edge detection algorithms must be followed by edge linking and other boundary detection procedures designed to assemble edge pixels into a more meaningful set of object boundaries. The procedure considered here is based on computation of edge orientation and magnitude.

The procedure followed for edge linking or boundary linking is dependent on a small neighborhood similar to edge detection process. All points having similar characteristics are linked, forming an almost continuous edge much better than that achieved by classical edge detection algorithm. The two characteristics to evaluate the similarity of edge pixels are :

1. The strength or the magnitude of the gradient operator used to produce the edge pixel
2. The direction of the gradient.

The strength of the gradient as computed in earlier sections is represented as $|g[f(x, y)]|$.

For edge linking operation, the edge detected image received from earlier methods is utilized. A pixel x', y' situated in a predefined neighborhood of (x, y)

was analyzed for edge linking as expressed in following algorithm :

if $|g[f(x, y)] - g[f(x', y')]| \leq T$ and

$|\theta(x, y) - \theta(x', y')| < A$

then $r_{xy} = k$

where

T and A are the gradient and angle thresholds respectively.

r_{xy} is the grey level of $(x, y)^{\text{th}}$ pixel.

k denotes the grey level of the edge pixel.

$\theta(x, y)$ is the direction of the gradient vector.

Based on the above algorithm, a point (x', y') in the predefined neighbourhood of (x, y) are linked. This operation is performed by moving the predefined window throughout the image. An edge detected output received using Frei-Chen derivative filtering was processed using edge linking operation. The output image is shown in Fig. 4.20.



Fig. 4.20 Edge detected image after edge linking (The Frei-Chen image is used for edge linking)

4.5 Results and Discussion

A detailed assessment of image processing tools for edge detection has been carried out in the present chapter. It is proposed to perform image smoothing operation prior to edge detection. For smoothing the satellite images, four techniques have been evaluated and the result is presented in Table 4.1

Table 4.1 Results of image smoothing techniques on a selected region of the image

Name of the technique	Size of kernel	Smoothing	Finer lineament details	Computational time required
Moving average filtering	5×5	over and blurred	mostly lost	Very slow
	3×3	blurred	some of the salient details are lost	Slow
Sigma filtering	5×5	over and blurred	mostly lost	Very slow
	3×3	Patchy appearance	Some details are lost but better than moving av. filt.	Slow
Median filtering	3×3	Excellent	Preserved	Very slow
Pseudomedian filtering	3×3 plus shape	Excellent	Preserved	Fast

Based on the above results it is decided to opt for pseudomedian filtering for smoothing the satellite images in order to attain excellent smoothing, preservation of lineament fabric and high processing speed. The smoothed image of the study area

using this technique is shown in Fig. 4.6. This image has been used in subsequent edge detection operations.

The delineation of lineaments is carried out by detection of edges in the satellite imagery. Several methodologies discussed here come from derivative filtering approach or entropy based approach. The results obtained are summarised in Table 4.2.

Based on these results, it has been realised that entropy based filtering do not yield encouraging response in the case of remotely sensed images of Earth surface. The second order Laplacian operator misses some other salient edges (ramp edges in nature) and hence can be utilized only for preliminary study of lineaments of the area. The best result has been obtained in the case of first order Frei-Chen derivative filtering. The edge output produced using this method may be utilised for lineament mapping. Results of edge detection yielded by Kirsch and Robinson 5-level operators appear impressive. These two edge outputs may be utilized in association with Frei-Chen output for final mapping of the lineaments.

Edge linking has been performed on the edge output received using the Frei-Chen operator (Fig. 4.11) and the edge linked image is shown in Fig. 4.20. It is found that some discontinuties have been filled which helps the process of lineament extraction and visual mapping.

In this chapter, the potentials of various digital image processing tools available to extract the edges and map the lineaments are presented. Based on these tools, an image processing scheme for delineation of mapping of edges has been proposed, which is detailed in Chapter 6.

Table 4.2 Results of edge detection techniques on a selected region of the image

Technique	Result
First order derivative filtering	
(a) Orthogonal derivative filtering	
(i) Prewitt operator	Very good detection of horizontal and vertical edges, thick edges obtained.
(ii) Sobel operator	Very good detection of inclined edges, large number of small edge contours formed.
(iii) Frei-Chen operator	Very good detection of horizontal, vertical and inclined edges, edges are sharper than Prewitt and Sobel operators.
(b) Directional gradient method	
(i) Prewitt compass gradient	Large number of edges detected but a large number of small edges.
(ii) Kirsch gradient operator	Very good detection of edges, less noisy than Prewitt compass gradient method.
(iii) Robinson 3-level directional operator	Very good edge detection, smaller edges found in large numbers.
(iv) Robinson 5-level directional operator	Very good edge detection, smaller edges found in small numbers.
(c) Second order Laplacian operator	Edges are detected but some of the salient edges are lost.
(d) Entropy based filtering	Only few edges detected.

Chapter 5

MORPHOLOGICAL IMAGE TRANSFORMATIONS FOR ENHANCEMENT OF LINEAMENTS

5.1 Introduction

In the previous chapter, structural features of digital satellite imagery have been extracted using classical image processing techniques. The other group of image processing techniques, being discussed in this chapter, is the *morphological image processing*. In this an image is understood to be a set of natural or real numbers which is constituted by a number of subsets comprising numerous different structuring elements. These subsets are having a relationship which can be described in the notion of set theory as proposed by Matheron (1975) and Serra (1982, 1986) and Giardina and Dougherty (1988).

Morphological image processing has been utilized in many areas and has gained popularity in recent years. Conrad in 1972, employed principles of mathematical morphology for studying the permeability characteristics of petroleum rocks using the simulation of a set of geological faults (Serra, 1982). Photographs of dust particles had been used to understand their size distribution and shape characteristics (Klein, 1973). Meyer (1977) employed mathematical morphology to build a device for automatically performing cytological examinations. In recent past, scientists in the area of remote sensing have initiated studies involving morphological image processing for feature identification in satellite imagery. In this chapter, the possibility of employing the concept of morphological image processing for enhancing structural features using remotely sensed satellite data are explored. In remote

sensing this concept is new and needs a thorough testing before a formal use. The attempt in this chapter is to develop a sequence of operations using the concept of mathematical morphology to achieve the same objective as in previous chapter i.e. extraction of geological structural details of the area.

Morphological operations for noise removal and edge enhancement have been developed based on the concept of mathematical morphology. The results obtained by the tools of morphological image processing are compared with the results obtained using techniques discussed in the previous chapter.

5.2 Mathematical Morphology

The concept of mathematical morphology was first proposed by Matheron in 1964, who developed the concept in a realistic manner by utilizing the morphology or geometric shape of the constituent elements of an object. The morphological image processing is generally based on the analysis of binary image in terms of some predetermined geometric shape known as a *structuring element* (Giardina and Dougherty, 1988). The methodology involved is also dependent on the selection of a suitable structuring element and investigating its behaviour in the image set. Development of the mathematical morphology was done utilizing the binary image case. Only recently, this concept has been developed for the case of multilevel or greyscale images. The remotely sensed images are essentially grey scale images. Therefore it is now possible to explore the usefulness of the concept of mathematical morphology for image processing of satellite digital images.

In mathematical morphology an image $f(x, y)$ is considered as a set which is a subset of n -dimensional euclidean space \mathcal{R} .

Any binary image object B is represented as follows :

$$B = \{z : f(z) = 1, z = (x, y), (x, y) \in \mathcal{R}^2\} \quad (5.1)$$

The binary image background is a set B^c which is defined as :

$$B^c = \{z : f(z) = 0, z = (x, y) \in \mathcal{R}^2\} \quad (5.2)$$

Here the function f is known as the characteristic function of B . If we are using digitized image data set which is an element of euclidean grid \mathcal{Z}^2 then the above equations can be represented as

$$B = \{(u, v) : f(u, v) = 1, (u, v) \in \mathcal{Z}^2\} \quad (5.3)$$

The binary image background is a set B^c which is defined as

$$B^c = \{(u, v) : f(u, v) = 0, (u, v) \in \mathcal{Z}^2\} \quad (5.4)$$

Mathematical morphology utilizes some set theoretic notions which form its foundation for morphological image processing and are summarized in the following paragraphs.

A digital image is considered an arbitrary space \mathcal{B} . An object B of this space is a subset i.e., $B \subset \mathcal{B}$. Thus an image space is constituted by infinite number of such image subsets. A family of such subsets like B constitute a set \mathcal{Z} which is supposed to be less random in nature than the image space \mathcal{B} . Some of its properties are listed as follows :

1. \mathcal{Z} is a complete array with a partial-ordering relation called inclusion. Any finite set which represent an object $B_i \in \mathcal{Z}$ in the image space has a least upper bound and a greatest lower bound both belonging to \mathcal{Z} .
2. The lattice \mathcal{Z} is distributive, i.e.,

$$B \cup (C \cap \mathcal{Z}) = (B \cup C) \cap (B \cup \mathcal{Z}) \quad (5.5)$$

Each of the subset like B possesses a complement B^c within \mathcal{Z} .

$$B \cup B^c = \mathcal{Z} \quad \text{and} \quad B \cap B^c = \Phi \quad (5.6)$$

If we have two sets B and C , their difference can be expressed as

$$B/C = B \cap C^c$$

In case of two sets B and C which belong to \mathcal{Z} , the following relations are possible :

1. B is included in C $[B \subset C]$
2. B hits C $[B \uparrow C : \text{meaning } B \cap C \neq \Phi]$
3. B misses C $[B \subset C^c : \text{meaning } B \cap C = \Phi]$

The Boolean algebra provides the framework for such morphological treatments for all image objects. These basic definitions are expressed pictorially in the Figure 5.1.

Morphological transformations

The images are used for obtaining the information of the inherent objects and the efforts have been to maximize information retrieval. Generally human vision fails to accomplish this task efficiently due to its spectral and spatial constraints (Gonzalez and Wintz, 1977). Digital image processing can alleviate this limitation to a larger extent. Morphological transformations attempt to establish spatial relationship between image subsets i.e., objects. In morphological image processing the basic set selected to identify any larger image subset of the principal image \mathcal{Z} is very important. This basic set is termed as *structuring element*.

In an image space \mathcal{Z} for each of its points i a separate structuring element $a(i)$ can be associated. An image can be modified to various forms by changing the structuring element or the transformation types.

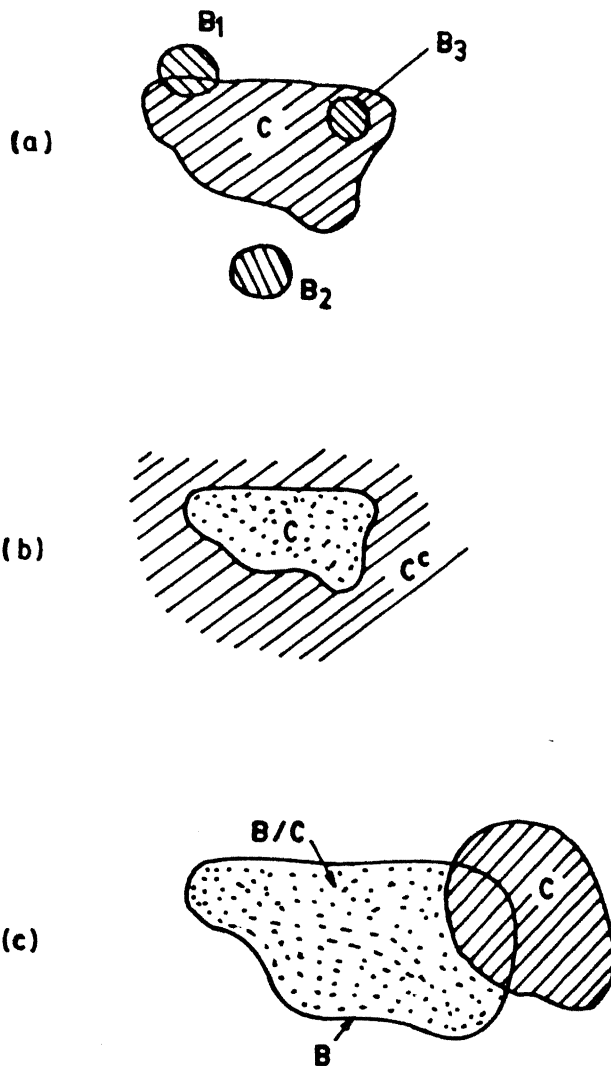


Fig. 5.1 An illustration of basic morphological operations
 (a) B_1 hits C ; B_2 misses C ; B_3 is included in C
 (b) Complement C^c of C
 (c) Difference set B and C , B/C

Few basic transformations are *dilation*, *erosion* and *hit and miss transformation*. Mathematically they are shown as follows :

Dilation of an image M

$$\text{DILATE}\{M\} : \{i : a(i) \uparrow M\} \quad (5.7)$$

Erosion of an image M

$$\text{ERODE}\{M\} : \{i : a(i) \subset M\} \quad (5.8)$$

By selecting two structuring elements $a_1(i)$ and $a_2(i)$, the hit-or-miss transformation can be expressed as the difference of M eroded by $a_1(i)$ and M dilated by $a_2(i)$.

$$\text{HMT}\{M\} : (\text{ERODE}\{M\} \text{ by } a_1) / (\text{DILATE}\{M\} \text{ by } a_2) \quad (5.9)$$

Several other morphological transformations Ψ are possible on these lines which may use union, complement, dilation, erosion, hit or miss, and various other available set theoretic notions.

An image consists of wealth of information which complicates the process of feature identification. In morphological image processing the attempts are directed to manage information loss through successive transformations. These transformations must adhere to some basic properties to yield desired quantitative and qualitative results. These properties have been evolved by Serra (1986) and have become popular as the basic principles of mathematical morphology. These principles are discussed as follows :

1. Increasing :

If inclusion is preserved the morphological transformation Ψ is called increasing, i.e., when,

$$B \subset C \rightarrow \Psi(B) \subset \Psi(C) \quad \forall B, C \in Z \quad (5.10)$$

2. Anti-extensivity :

A morphological operation is called anti-extensive when it shrinks B , i.e.,

$$\Psi(B) \subset B \quad \forall B \in \mathcal{Z} \quad (5.11)$$

3. Idempotence :

After each subsequent application if the output image is unchanged by morphological transformation then such transformations are called idempotent.

$$\Psi[\Psi(B)] = \Psi(B) \quad \forall B \in \mathcal{Z} \quad (5.12)$$

4. **Homotopy** : A transformation is called homotopic if it preserves the homotopic sequence of an image or its subset (B). This concept of homotopy is illustrated in Fig. 5.2.

The image set can be considered as a topological space. Each bounded set M is associated with some homotopy tree special to its kind and whose trunk corresponds to its background M_0 (which is constituted by infinite number of M^c component). The first branch of this homotopic tree is corresponding to M_1 of M adjacent to M_0 and the second branch M_2 of M next to M_1 as illustrated in the figure. A transformation is termed as *homotopic* only if it preserves this homotopic tree.

5.3 Greyscale Morphological Image Processing

Morphological image processing is a type of processing in which the spatial form or structure of the objects within an image are modified. Dilation and erosion are two fundamental morphological operations (Serra, 1982). With dilation, an object grows uniformly in spatial extent, while with erosion, an object shrinks uniformly.

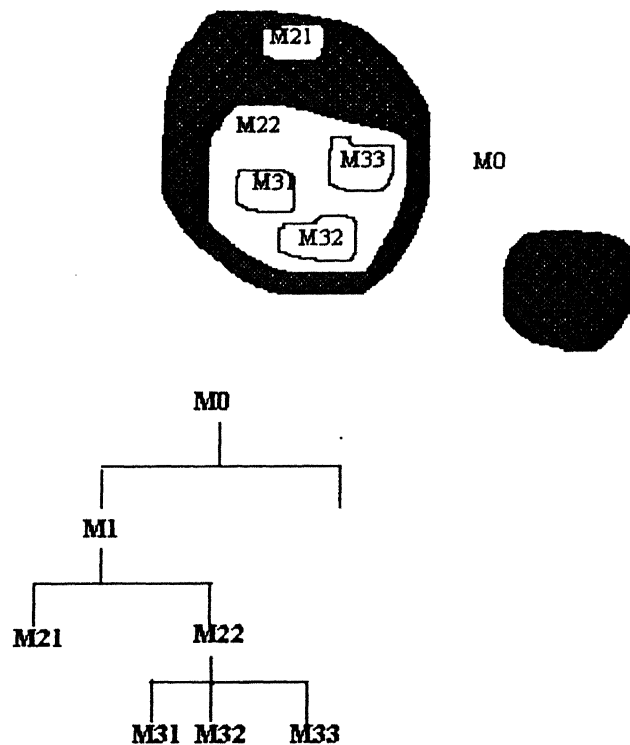


Fig. 5.2 Illustration of the concept of homotopy in mathematical image algebra

The principles of mathematical morphology described in preceding sections are applicable for binary images and can also be extended to the greyscale image case. Greyscale images are described as a grey level function $f(x, y)$ on the points of Euclidean 2-space. In euclidean 3-space the grey level function is considered a set of points $[x, y, f(x, y)]$ imagined as a thin, undulating and not necessarily a continuous sheet. A greyscale image is described in terms of mathematical morphology by an umbra $U(f)$ in Euclidean 3-space, where a point p with its coordinates (x, y, z) belongs to the umbra if and only if $z \leq f(x, y)$. In image processing the umbrae are very significant as they remain umbrae even after morphological operations such as union, intersection, dilation or erosion (Sternberg, 1986).

Sternberg (1986) has extended the fundamental morphological operations of dilation, erosion, opening and closing from the binary image case to the greyscale images and the same are explained in following subsections.

5.3.1 Dilation

The dilation of a set X by structuring element Y can be expressed as :

$$X \oplus Y = \bigcup_{y \in Y} X_y \quad (5.13)$$

The dilation of $U[a]$ by B is the union of translations of $U[a]$ by points of B . At a given location (x, y) the grey levels $d(x, y)$ of the dilation are determined by the maxima of the translated umbra $U[a]$. Although, $U[a]$ is translated by all the points of B , only those points on the surface of B can create maxima. The dilated greyscale image is computed then, as the maximum of the sum of grey levels of $b(x, y)$, the function describing the surface of B , with each of the points of $a(x, y)$,

$$d(x, y) = \max_{i,j} [a(x - i, y - j) + b(i, j)] \quad (5.14)$$

5.3.2 Erosion

The erosion of a set X by structuring element Y can be expressed as

$$X \ominus Y = \bigcap_{y \in Y} X_{-y} \quad (5.15)$$

The erosion of $U[a]$ by B is likewise determined as a difference of the grey levels of $b(x, y)$ and points of $a(x, y)$, the grey levels of the eroded image $e(x, y)$ determined by the minimum over all the points of $b(xy)$,

$$e(x, y) = \min_{i,j} [a(x - i, y - j) - b(-i, -j)] \quad (5.16)$$

The expressions for greyscale dilation and erosion bear a marked similarity to the convolution integral encountered frequently in digital image processing, with sums and differences replacing multiplication and minimum and maximum replacing summation. Image processing through iterative morphological transformation is a process of selective information removal where irrelevant image content is irrecoverably destroyed, enhancing the contrast of the essential image features.

5.3.3 Opening

The opening of X by Y is defined in terms of an erosion followed by a dilation. Mathematically it can be represented as:

$$X_Y = [X \ominus Y] \oplus Y. \quad (5.17)$$

The opening of X by Y is the union of translation of Y completely contained in X .

5.3.4 Closing

The closing of X by Y is a dilation followed by an erosion. Mathematically it can be represented as:

$$X^Y = [X \oplus Y] \ominus Y. \quad (5.18)$$

The closing of X by Y is the complement of the translations of Y completely contained in X^c .

Greyscale images opened and closed by 3-dimensional structuring elements are transformed in predictable and useful ways. Rotationally symmetric structuring elements are often employed for opening transformations because the results do not depend on the orientation of the image.

5.4 Morphological Image Smoothing

As discussed earlier satellite images consist of numerous cover types which suppress structural details of the area. This problem is solved by filtering the noise content of the image. All scattered tiny features less than a particular size are considered noise as they add to the misinterpretation. Morphological methods seem to be most appropriate to define noise and extract it more easily without disturbing the basic structure of the image. In following sections two methods used for image smoothing are discussed.

5.4.1 Morphological image smoothing using erosion

Pixel set constituting noise can be characterized and identified based on their specific spectral non-conformity in a greyscale image case as well as by their size. A structural element of small size either binary or multilevel can be selected which can be used for erosion of greyscale image. In present study a 3×3 structural element as shown below is selected to erode the original image space.

$$\begin{pmatrix} 1 & 1 & 1 \\ 1 & 1 & 1 \\ 1 & 1 & 1 \end{pmatrix}$$

Here the central pixel is replaced by the minimum of all the pixel considered within the structuring element window convolving with the image. This way any scattered

noise present in the image can be eliminated or eroded. This operation is based on the greyscale erosion concept developed by Sternberg (1986).

This operation provided good result in the case of binary images (Salim, 1991) but could not produce similar result in the case of multilevel satellite imagery. The output received by this method appeared blurred and hazy. Therefore, this method has not been used in present greyscale image case.

5.4.2 Morphological image smoothing using neighbourhood criterion

A morphological technique based on neighbourhood relation has been utilized. The structural element selected for defining neighbourhood relation is of plus shape. Identification of noisy pixels and smoothing has been carried out as shown below

IF

$$|(a_{xy} - a_i)| < \text{Threshold}; \quad \forall i = 1 \text{ to } 8$$

THEN

$$a_{xy} = a_{xy}$$

ELSE

a_{xy} = Mean of all neighbourhood pixels except the central pixel

The pixel numbering configuration is as follows:

$$\begin{pmatrix} a_1 & a_2 & a_3 \\ a_8 & a_{xy} & a_4 \\ a_7 & a_6 & a_5 \end{pmatrix}$$

For each of the window cases this operation is performed and the window is moved over the image space to smooth it. With this method smoothing of the image could be achieved without compromising the loss of minor linear features. The method is very fast as simple comparison and difference operations are involved. The degree of smoothness may be controlled by assigning suitable threshold.

Based on this algorithm the IRS band 3 image has been processed and the smoothened output is shown in Fig. 5.3.

5.5 Morphological Edge Detection

There are several transforms available to detect edges or boundaries in an image based on the principles of mathematical morphology. Most of them are based on the operations of dilation and erosion. These transforms are generally non-reversible in nature. They use a sequence of operations involving dilation, erosion and difference for detection of edges. Since extensive computations involving complex mathematics like differentiation, integration, inverse and division are not involved these techniques consume lesser computer time. These techniques use simple comparison, addition and subtraction processes therefore the shape of object is not disturbed.

Based on the morphological transformations and selection of suitable structuring elements, several edge detectors are being discussed in this section.

5.5.1 Edge detection using different structural elements

In the case of edge or lineament detection in satellite imagery using morphological filtering the following methodologies involving dilation and erosion have been utilized.

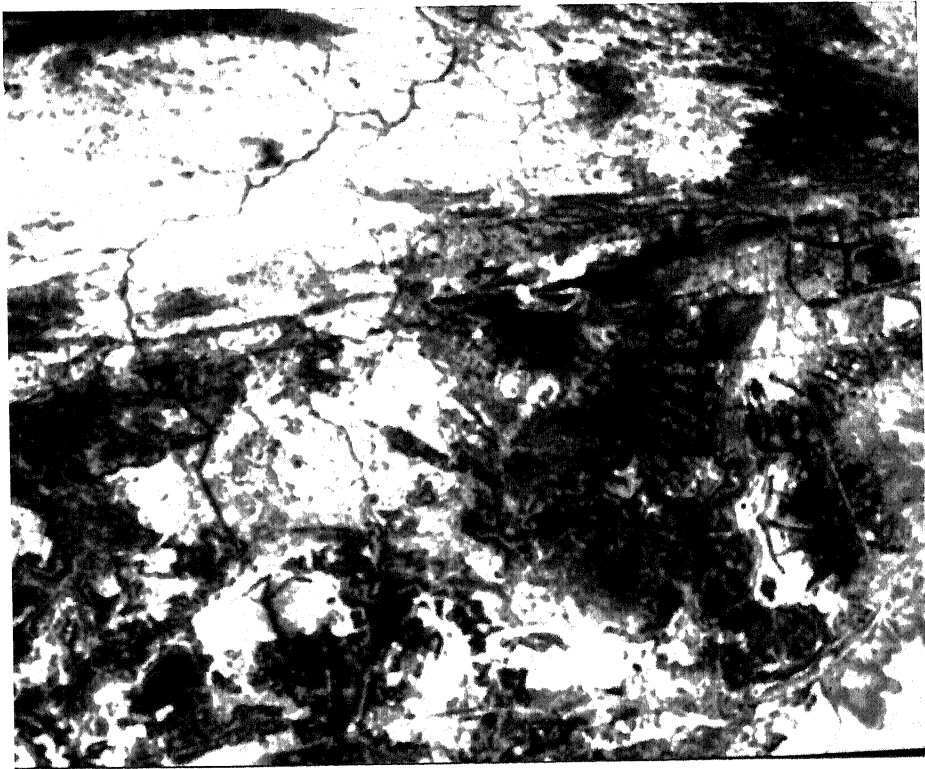


Fig. 5.3 Morphological image smoothing of IRS Band 3 image of the study area

1. In this process the digital satellite image $f(x, y)$ is first dilated using a structuring element $h(i, j)$. The original image is subtracted from this image. The resultant transformed image $g(x, y)$ reveals a large number of structural features or the edges. It is noticed here that edges mainly of outer boundary of the objects are detected.

Step One :

$$\text{DILATE}[f(x, y)] = f(x, y) \oplus h(i, j) \quad (5.19)$$

Step Two :

$$g(x, y) = \text{DILATE}[f(x, y)] - f(x, y) \quad (5.20)$$

Therefore, this process is relevant for extracting the geological boundaries of various formations and other structural details marked by outer peripheral boundary.

2. In the second method the digital satellite image $f(x, y)$ is eroded using a structuring element $h(i, j)$. This image is subtracted from the original image and the resultant image g' revealed a large number of edges.

Step One :

$$\text{ERODE}[f(x, y)] = f(x, y) \ominus h(i, j) \quad (5.21)$$

Step Two :

$$g'(x, y) = f(x, y) - \text{ERODE}[f(x, y)] \quad (5.22)$$

Here, edges mainly of interior boundary of the objects are delineated emphatically and the edges at the outer boundary are not revealed as efficiently as in first methodology. Since inner edges are present in abundance, they add to the confusion while interpreting the lineaments.

The structuring element $h(i, j)$, indicated in the Equation 5.21, is the basic element influencing the final output by its size and shape. Several such elements can be designed to obtain output closer to the desired one. Some of the structuring element used for delineating the structural features in digital image are presented in Fig. 5.4.

Edge detection based on above two methods have been performed using these structuring elements and the best extraction of edges were obtained in the case of plus shaped structuring element of size 3 (Figs. 5.5 and 5.6).

5.5.2 Edge detection using top hat transformation

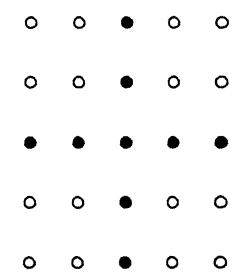
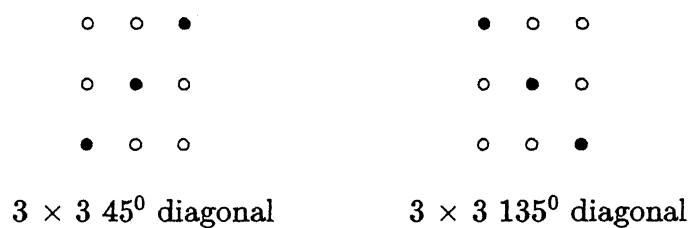
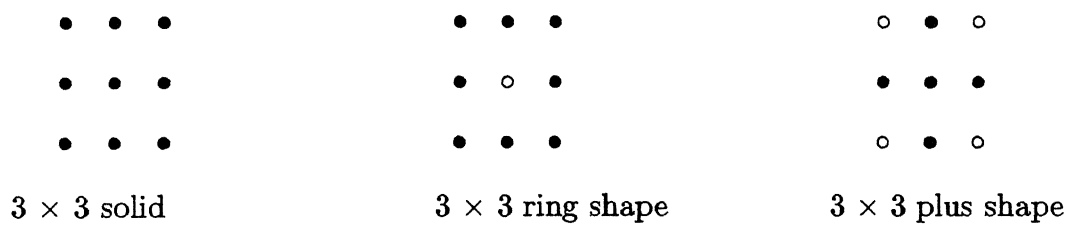
Edge detection may also be achieved using transformation involving operations of closing and difference. This technique is known as *top hat transformation*.

Top hat morphological transformation extracts topographical peaks or valleys from a digital images. It can also be used in the case of a greyscale satellite image.

Consider an image transformation involving open and difference operations performed on a raw image $f(x, y)$.

$$g(x, y) = f(x, y) - f_{\rho D}(x, y) \quad (5.23)$$

Here, $f_{\rho D}(x, y)$ is a transformed image of the original image $f(x, y)$ which has undergone open operation using a structuring element of convex disk D .



5 × 5 plus shape

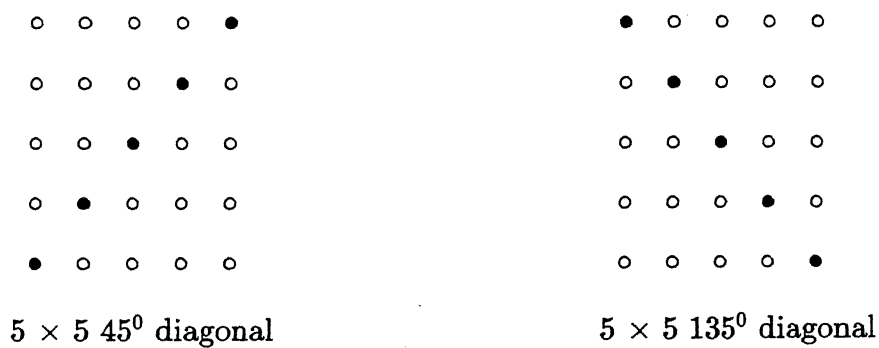


Fig. 5.4 Structuring elements used in edge detection



Fig. 5.5 Edge image using morphological edge detection (using DILATION operation)

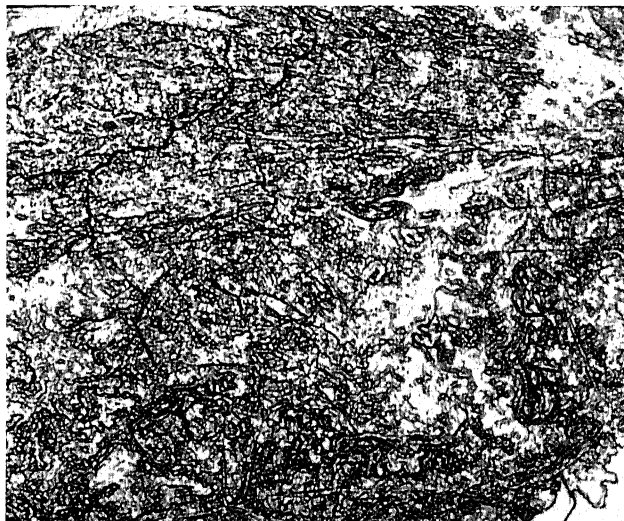


Fig. 5.6 Edge image using morphological edge detection (using EROSION operation)

Serra (1982) has discussed the geometrical and mathematical properties of open and close operations in detail. They are graphically indicated in Fig. 5.7. As seen in the figure, the changes in shape show that open operation using a structuring element mentioned above trims down the capes, peaks and saddles. The close operation on the other hand fills the valleys and emphasizes the isthmuses. The difference operation performed between the original image and the image received after opening is shown in Fig. 5.7(c). This image reveals the salient features such as the top portion of the capes and peaks after filtering. In Fig. 5.7(d), the difference operation performed on the closed image and the original image is shown. Here, it may be indicated that sudden drop in elevations, discontinuities and valleys are filtered out efficiently. In the present study, for the extraction of structural features such as faults, folds, fractures and lineaments, a transformation involving closing and difference with original image is expected to yield better result than the one involving opening and difference operations.

Meyer (1977) proposed the top hat transformation in his pioneering work on extraction of chromatin in cell nuclei. He conducted a large number of experiments which prove the power of this algorithm in extracting topographical peaks, isthmuses and capes.

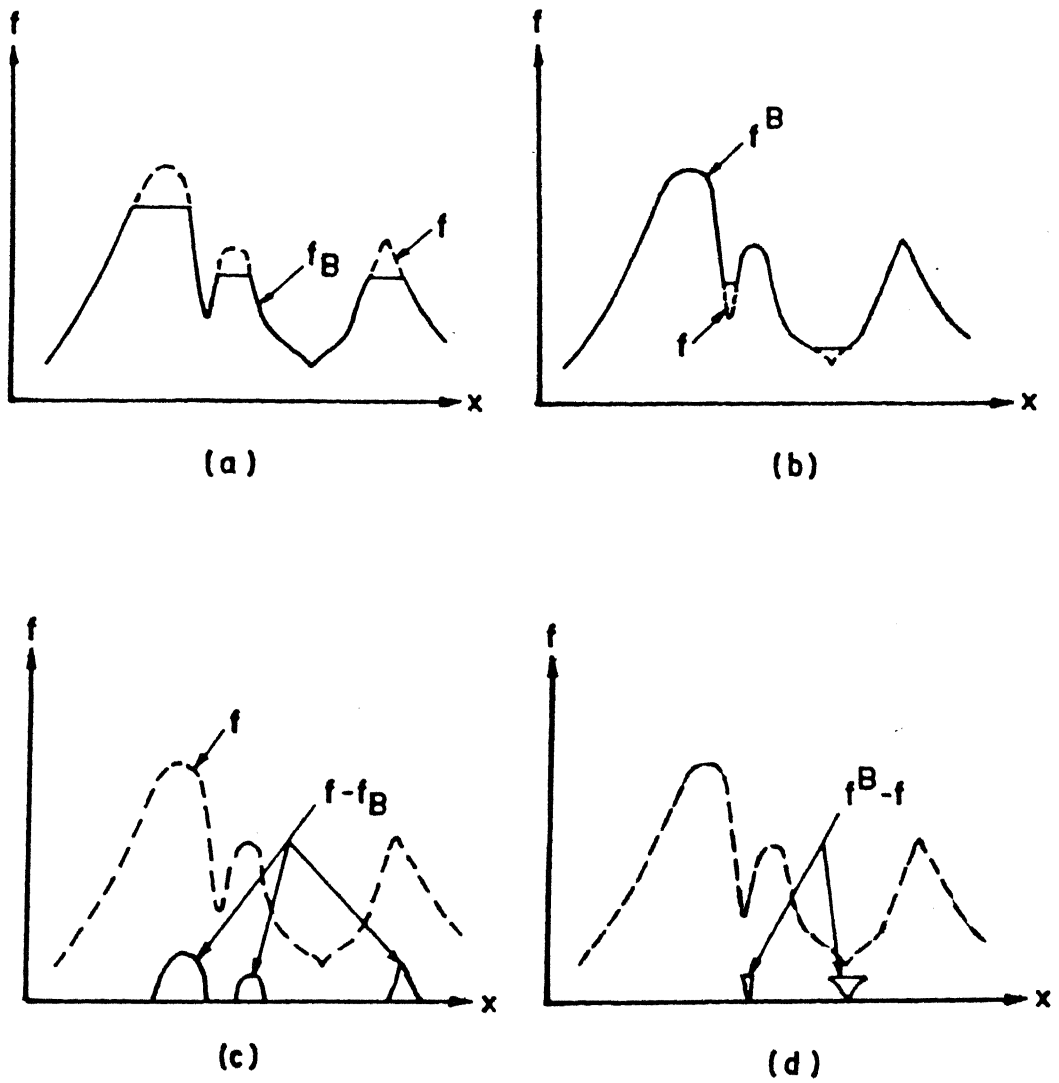


Fig. 5.7 (a) OPEN operation on one-dimensional signal
 (b) CLOSE operation on one-dimensional signal
 (c) Difference $(f - f_B)$;
 (d) Difference $(f^B - f)$.

The top hat transformation can be expressed mathematically as follows :

$$\text{Top hat } (f) = f^B - f; \quad (5.24)$$

where, f^B is an image obtained after performing close operation on image f .

The top hat transformation should be performed in all possible directions since the orientation of linear features in a new image is not known.

This transformation is performed in present study using a sequence of closing by three structuring elements having the directions ($0^\circ, 60^\circ, 120^\circ$) and also the complementary structuring elements in the directions ($30^\circ, 90^\circ, 150^\circ$) followed by the differencing operation with the original image. The structuring elements used in this study have hexagonal shape as shown in Fig. 5.8.

The smoothened image (Fig. 5.3) has been used for detection of the edges. The result of transformation using structuring element in 0° direction on the input image appeared very noisy. The other directions in which the transformation was applied were $60^\circ, 120^\circ, 30^\circ, 90^\circ$ and 150° . The respective edge images for these are indicated in Figs. 5.9 to 5.13.

5.5.3 Edge detection using top hat transformation and image superimposition

In the preceding section, edge detection based on top hat transformation has been discussed. This technique has brought out edge details efficiently which is useful for mapping the lineaments. Lineaments such as faults, fractures, dissected zones and joints are delineated on the satellite imagery using certain visual keys like isolated linear vegetation trend, drainage pattern and moisture in comparatively dry region. These cover types are associated with lower grey levels. If these cover types are superimposed on to the edge output generated in previous subsection then interpretation of lineaments would be easy.

This object has been achieved by involving the operation of top hat transformation and image superimposition. The top hat transformation is performed in the same way as shown by Equation 5.24. The process along with the modification suggested here is as follows:

- (1) Perform the close operation on the image;
- (2) Subtract the original image from the output image of step 1, it is same as Top hat transformation;

$$\text{Tophat } (f) = f^B - f \quad (5.25)$$

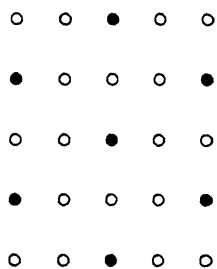
- (3) Compare each pixel of top hat (f) and original smoothened output and replace the pixel of top hat image if there exists a minima in the original smoothened image.

$$\text{EDGE}(f) = \text{MIN}[\{\text{Tophat}(f)\}, f] \quad (5.26)$$

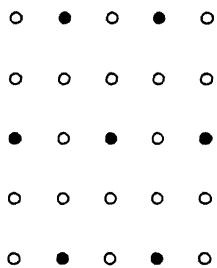
The operations involved in this method are indicated in Fig. 5.14.

This method using several structuring elements as shown in Fig. 5.15 has been attempted and the best results have been obtained in the case of 45° , 135° and plus shape structuring elements of size three. In the case of other structuring elements of larger size, fewer edges were obtained and other configuration of structuring elements rendered noisy edge environment unsuitable for edge mapping.

Edge images obtained using plus shaped, 45° and 135° structuring element of size 3 are shown in the Figs. 5.16 to 5.18 respectively.



First configuration



Second configuration

Figure 5.8 Hexagonal structuring elements chosen for directional top hat transformation

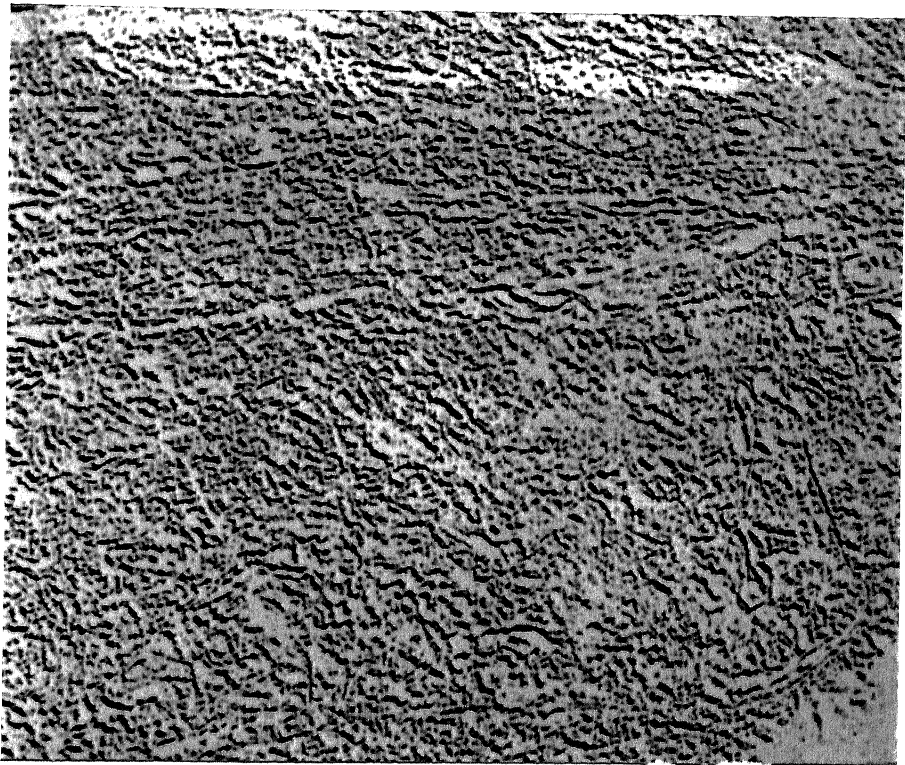


Fig. 5.9 Top hat transformation at 60° using hexagonal structuring element

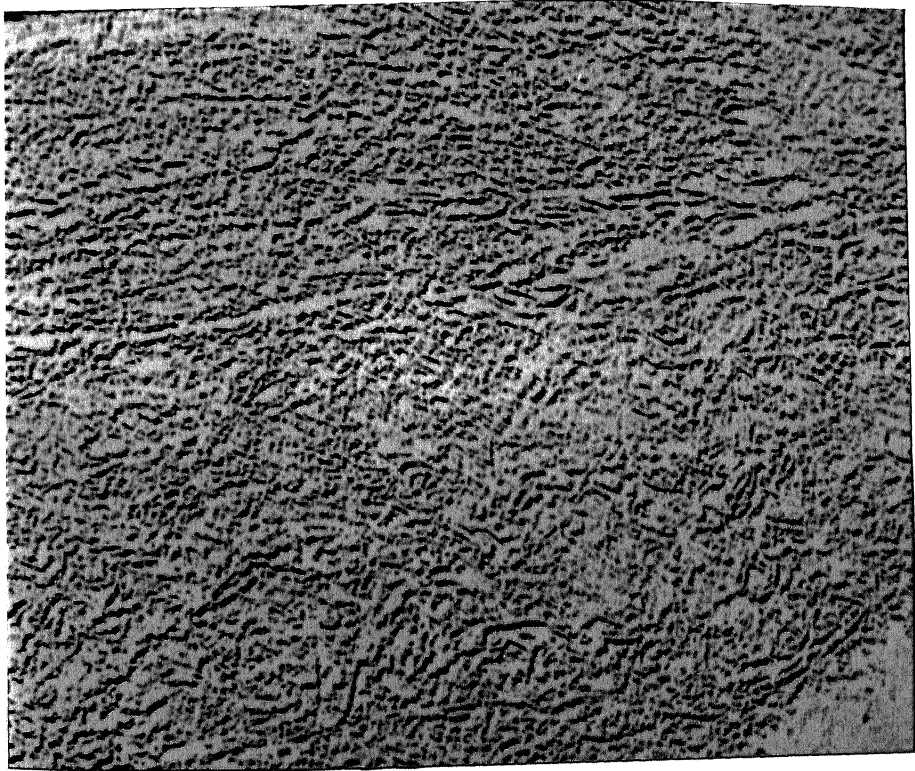


Fig. 5.10 Top hat transformation at 120° using hexagonal structuring element

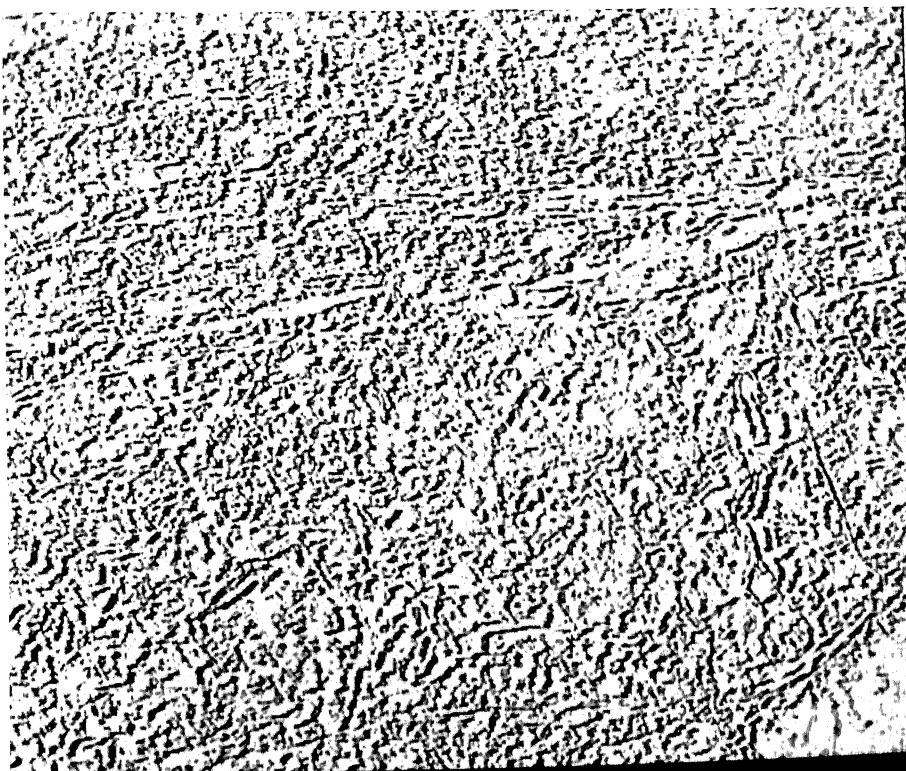


Fig. 5.11 Top hat transformation at 30° using hexagonal structuring element

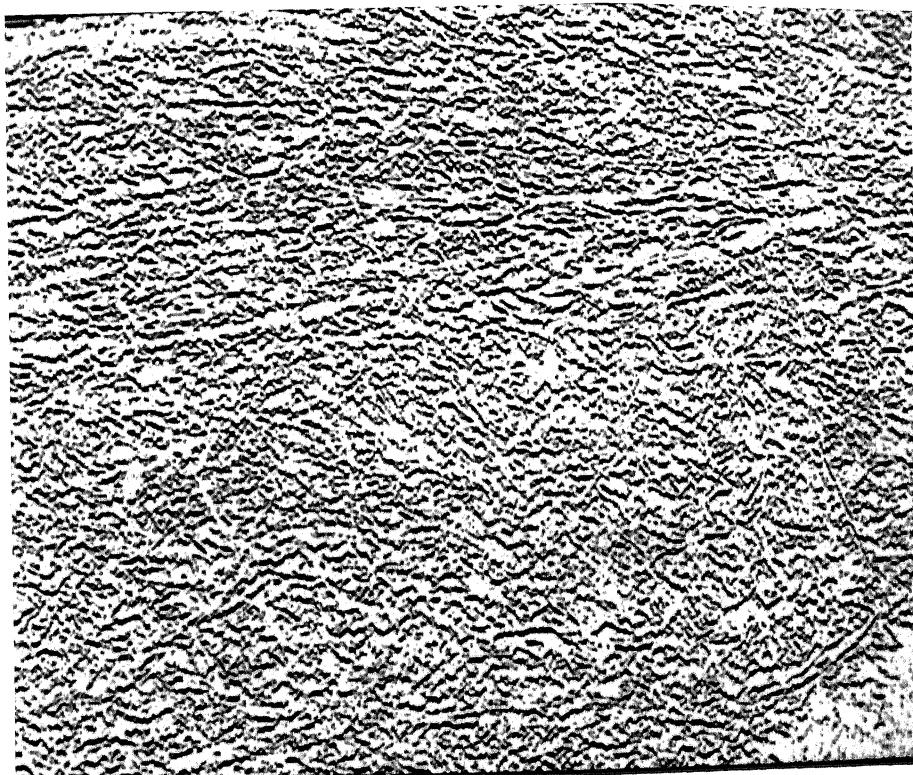


Fig. 5.12 Top hat transformation at 90° using hexagonal structuring element

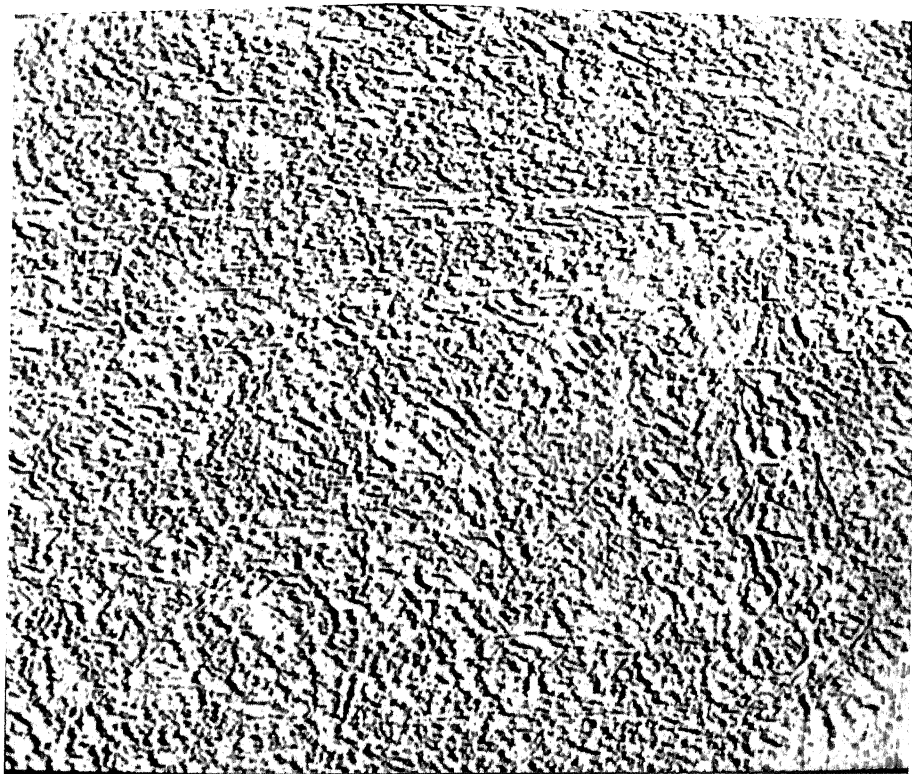


Fig. 5.13 Top hat transformation at 150^0 using hexagonal structuring element

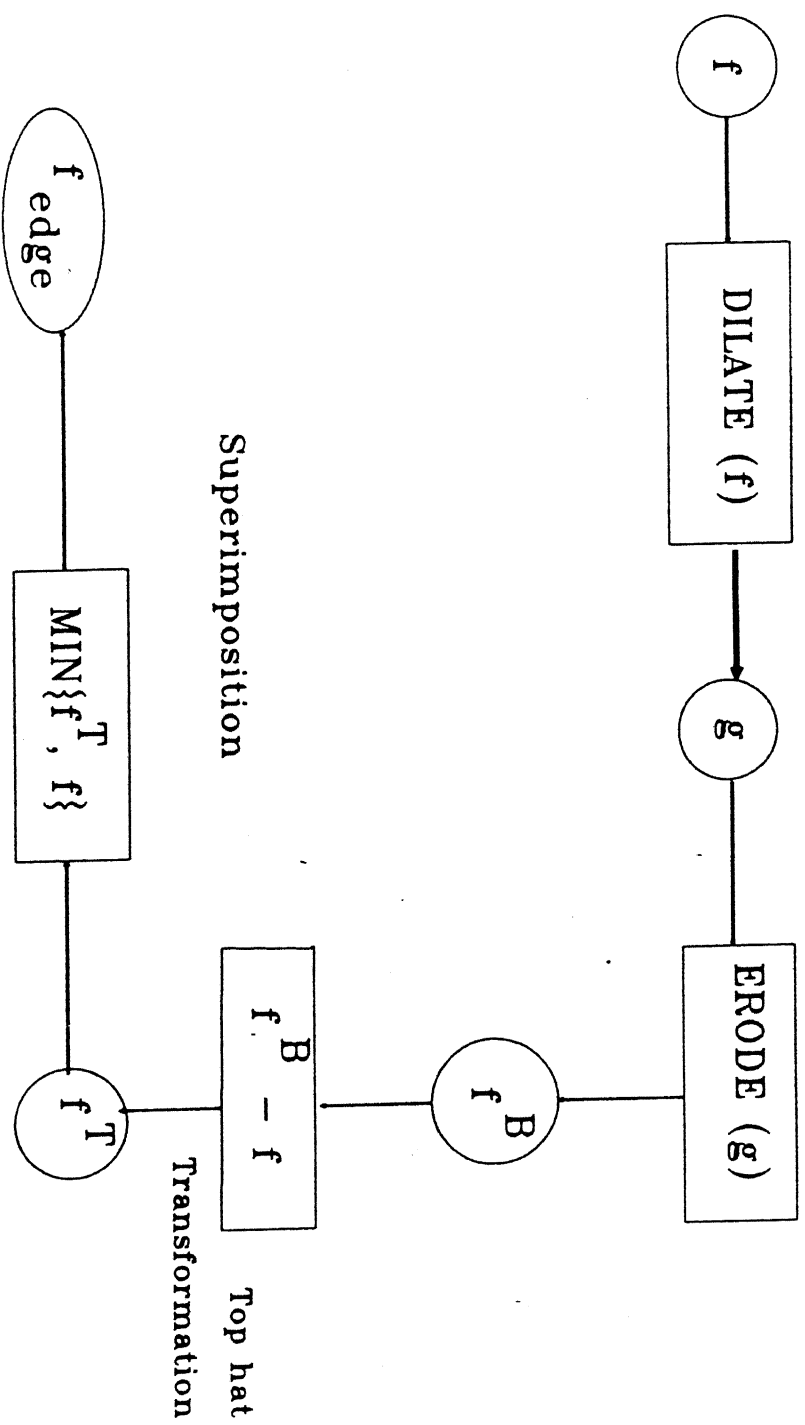
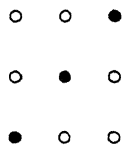
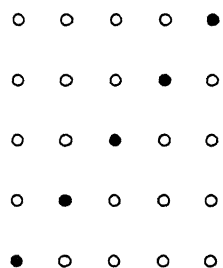


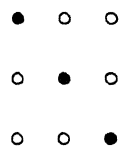
Fig. 5.14 Edge image using top hat transformation and image superimposition



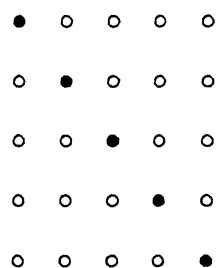
3×3 45^0 diagonal



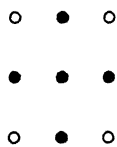
5×5 45^0 diagonal



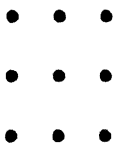
3×3 135^0 diagonal



5×5 135^0 diagonal



3×3 plus shape



3×3 solid disc

Figure 5.15 : Structural elements used for Top hat transformation and Image superimposition

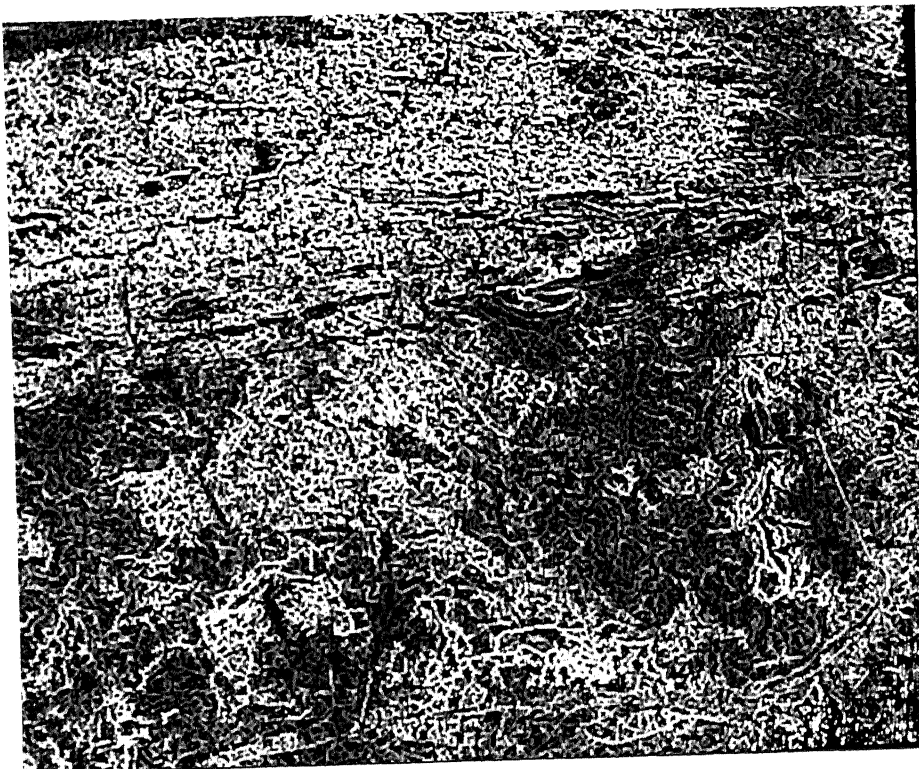


Fig. 5.16 Top hat transformation and image superimposition using 3×3 plus structuring element

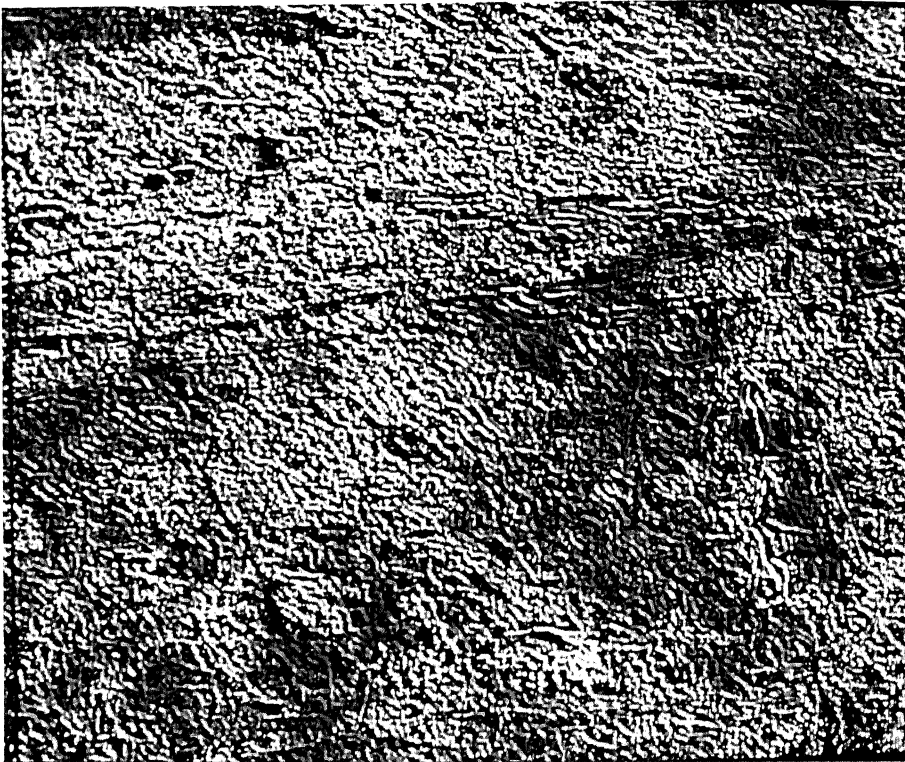


Fig. 5.17 Top hat transformation and image superimposition using 3×3 45° structuring element



Fig. 5.18 Top hat transformation and image superimposition using 3×3 135° structuring element

5.6 Results and Discussion

Two morphological image smoothing operations have been attempted and the one involving neighbourhood criterion has yielded better smoothing. This method is faster compared to median or pseudomedian filtering. In addition to this, the lineament fabric is preserved and also the appearance of overall image is sharper than moving average and sigma filter. The results obtained are comparable to the median or pseudomedian filter.

Three transformations dedicated for edge detection have been employed. The first one involved image differencing and dilation or erosion. Exterior boundaries have been extracted using dilation and image differencing whereas difference of original image and eroded image offers interior edges. The former transformation involving dilation is more useful in case of remotely sensed images. Several structuring elements have been used but the acceptable results are found with plus shape element (3×3).

The second approach adopted for edge detection is Top hat transformation. Hexagonal structuring elements of size two are employed to enhance the edges in various directions like 0° , 60° , 120° , 30° , 90° and 150° . The edge output showed dark zones offering the impressions of relief. The discontinuities and lineaments are better perceived in these edge images than edge output generated in the Chapter 4 using digital filtering method. Edge output for various directions offer a promise for better delineation of edges if used jointly.

The third approach of edge detection included image superimposition as a modification to top hat transformation. Three structuring elements (45° , 135° and plus shape (3×3)) have been utilized. If size of structuring element is increased the blurring effect appeared in the edge output.

The output obtained using this process offered most encouraging edge image on which faults and lineaments could be easily identified. This method provided effi-

cient tool to distinguish between physical objects (roads, railway lines and builtup features) and geological structural features.

Chapter 6

LINEAMENT MAPPING AND ANALYSIS

6.1 Introduction

The image processing tools attempted in Chapters 4 and 5 have been utilized to evolve two lineament detection schemes. They are *Digitedge Scheme* and *Morphedge Scheme*. Based on these schemes, lineament maps are prepared and statistical analysis of the lineaments is performed. The results are compared with available published work. Based on the processed satellite data, geological map is prepared.

The methodology adopted is presented. The results are compared with existing maps and with limited field verifications. A land use / land cover map using FCC of *principal components* is prepared. The ecological impact of surface coal mining and massive industrialization in the study area is discussed.

6.2 Lineament Mapping

In earlier Chapters 4 and 5 an attempt has been made to digitally enhance the satellite images to reveal the maximum structural details of the study area. Based on the methodologies developed and discussions made two schemes of lineament enhancement are proposed. The first is *Digitedge Scheme* which is based on the techniques of Chapter 4. The other scheme is designated as *Morphedge Scheme* and is based on the morphological concepts described in Chapter 5.

In Digitedge Scheme the 512×512 image of IRS-LISS II Band 3 of the study area is smoothed using pseudomedian filtering. This image is further utilized for lineament enhancements. Frei-Chen operator is applied to this image to yield the

edge enhanced image which is further thresholded to eliminate insignificant edges. In order to fill the minute gaps, the operation of *edge linking* is performed. The output image obtained is presented in Fig. 4.20. This image has been utilized as the base image to map the lineaments. Robinson 5-level and 3×3 entropy operators are employed to generate the output images (Figs. 4.17 and 4.19). This is termed an auxiliary image set deemed necessary to assist the process of lineament identification. The geological maps and toposheets of the study area have been used for verification during the process of mapping. A flow chart illustrating the process involved in this scheme is shown in Fig. 6.1 and the lineament map prepared based on this scheme is presented in Fig. 6.2.

The Morphedge scheme of lineament mapping is based on the methods discussed in Chapter 5. Here, the same image is smoothed using morphological neighborhood relationship. This image (Fig. 5.3) is utilized for further edge enhancement procedures. The top hat transformations using various shape and size of structural elements have been performed. These transformations are categorized in three groups. The *top hat one* has used 3×3 size diagonal structural elements at 45° and 135° . The *top hat two* has utilized a 3×3 plus shape structural element. Images of this group are further modified by performing image superimposition as discussed in Chapter 5. This process yielded three final images which act as input set for mapping the lineaments.

The *top hat three* transformation has used hexagonal structuring element of size two. As discussed earlier this transformation is performed at 60° , 120° , 30° , 90° and 150° . This process yielded five images which acted as an auxiliary image set to assist the process of delineation of lineaments. Using the input image set and auxiliary image set, lineament mapping has been carried out.

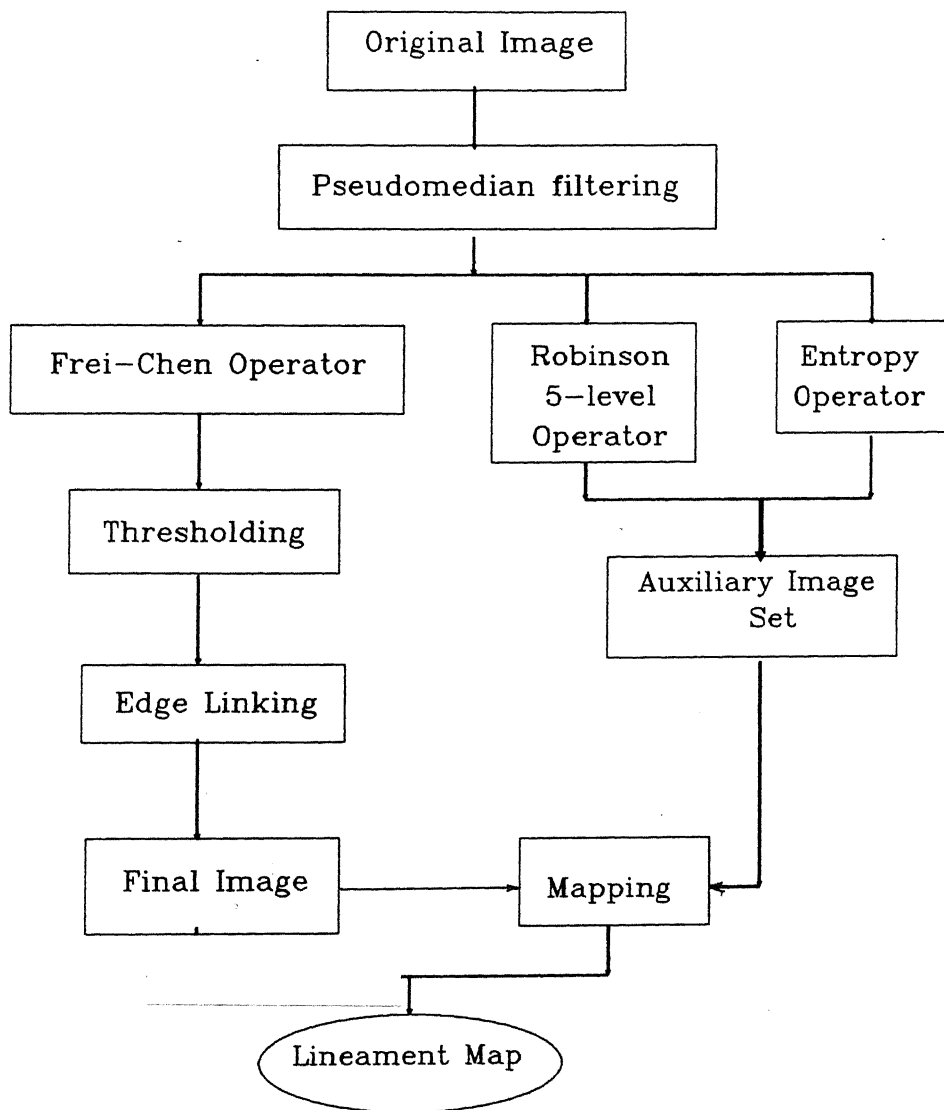


Fig. 6.1 Digtedge Scheme for lineament enhancement and mapping

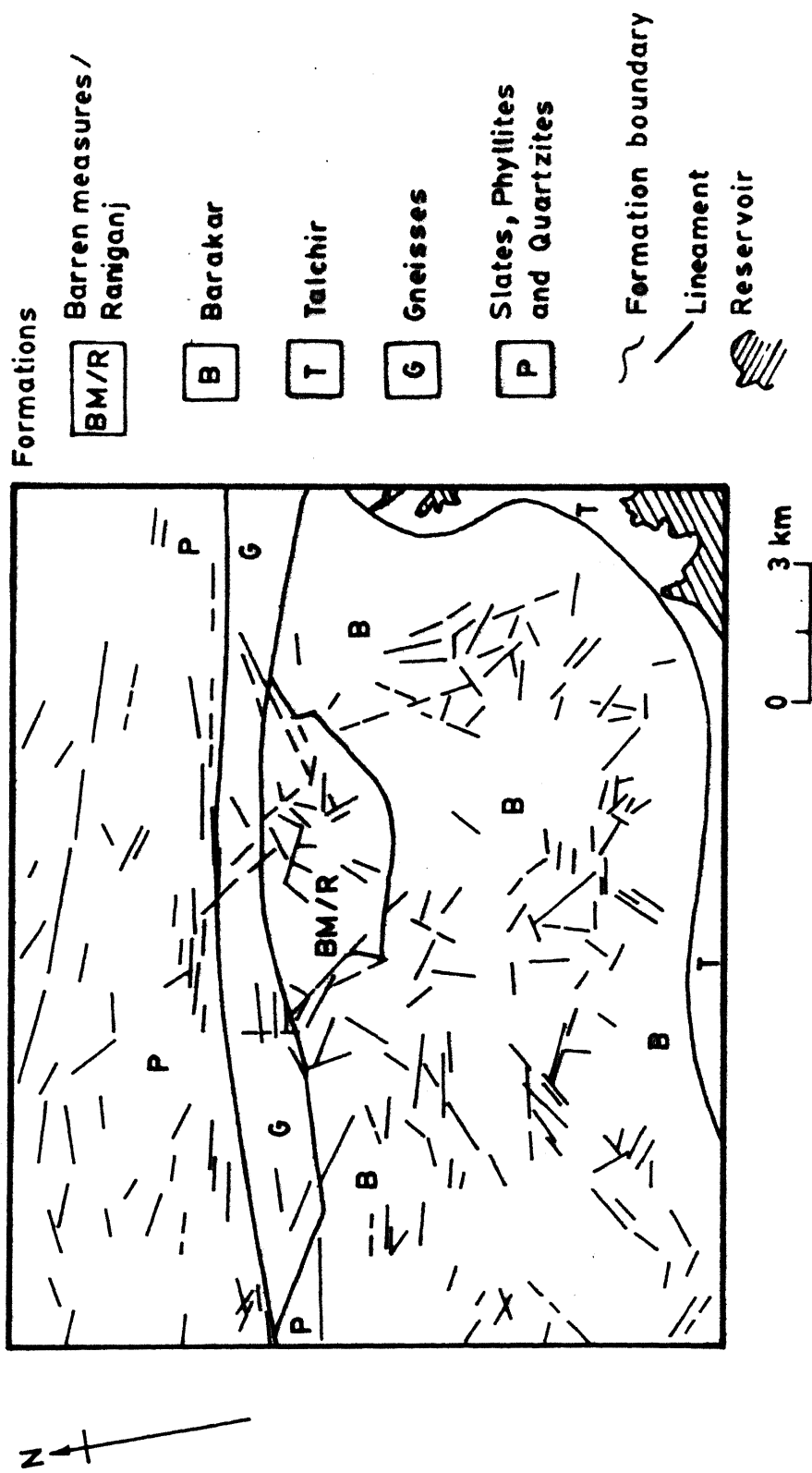


Fig. 6.2 Lineament map of study area prepared using Digitized Scheme

As in the earlier scheme, geological maps and toposheets of the study area are utilized for verification of interpretations. An outline of operations involved is presented as a flow chart in Fig. 6.3 and lineament map prepared using Morphedge scheme is illustrated in Fig. 6.4.

6.3 Lineament Analysis

Lineament map prepared by Digitedge scheme shows 186 lineaments as compared to 221 lineaments in the map prepared using Morphedge scheme. In these maps lineaments appear to be oriented in nature. Twelve zones identified indicating preferred orientation of lineaments are shown in the map (Fig. 6.5). These zones appear approximately similar to the geological divisions and coal mine blocks of the study area (Fig. 1.2).

To confirm the preferred orientation of lineaments in different zones, statistical analysis of the lineament data has been performed. The length of lineaments along with the angle from north is measured from both the maps. Considering lineaments as unit vectors and taking these angles, the *sines* and *cosines* of individual vectors have been computed and presented in a tabular form in Appendix-A.

Since each zone comprises a set of such unit vectors the dominant directions are computed from the vector resultants. The X and Y coordinates of the unit vector having the angle θ_i is computed as

$$X_i = \cos \theta_i$$

$$Y_i = \sin \theta_i.$$

The vector resultants in X and Y directions are

$$X_r = \sum_{i=1}^n \cos \theta_i$$

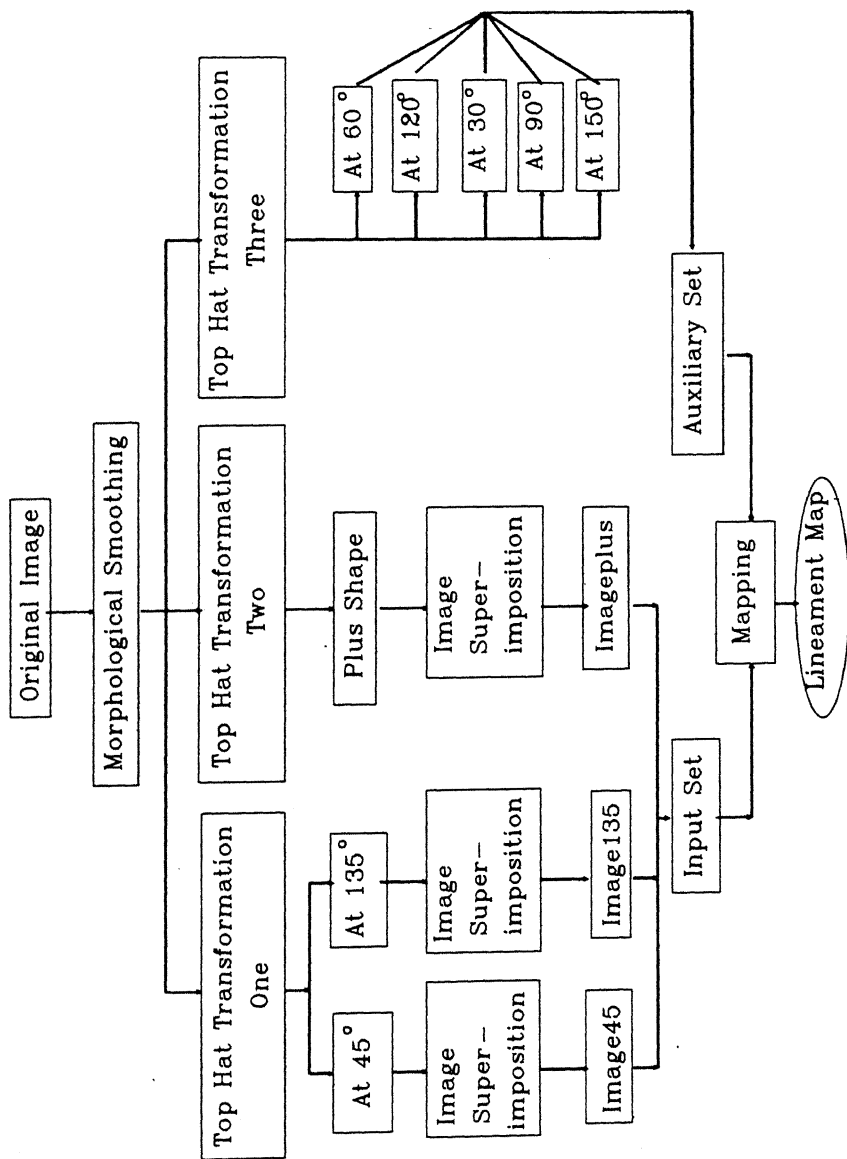


Fig. 6.3 Morphedge Scheme for lineament enhancement and mapping

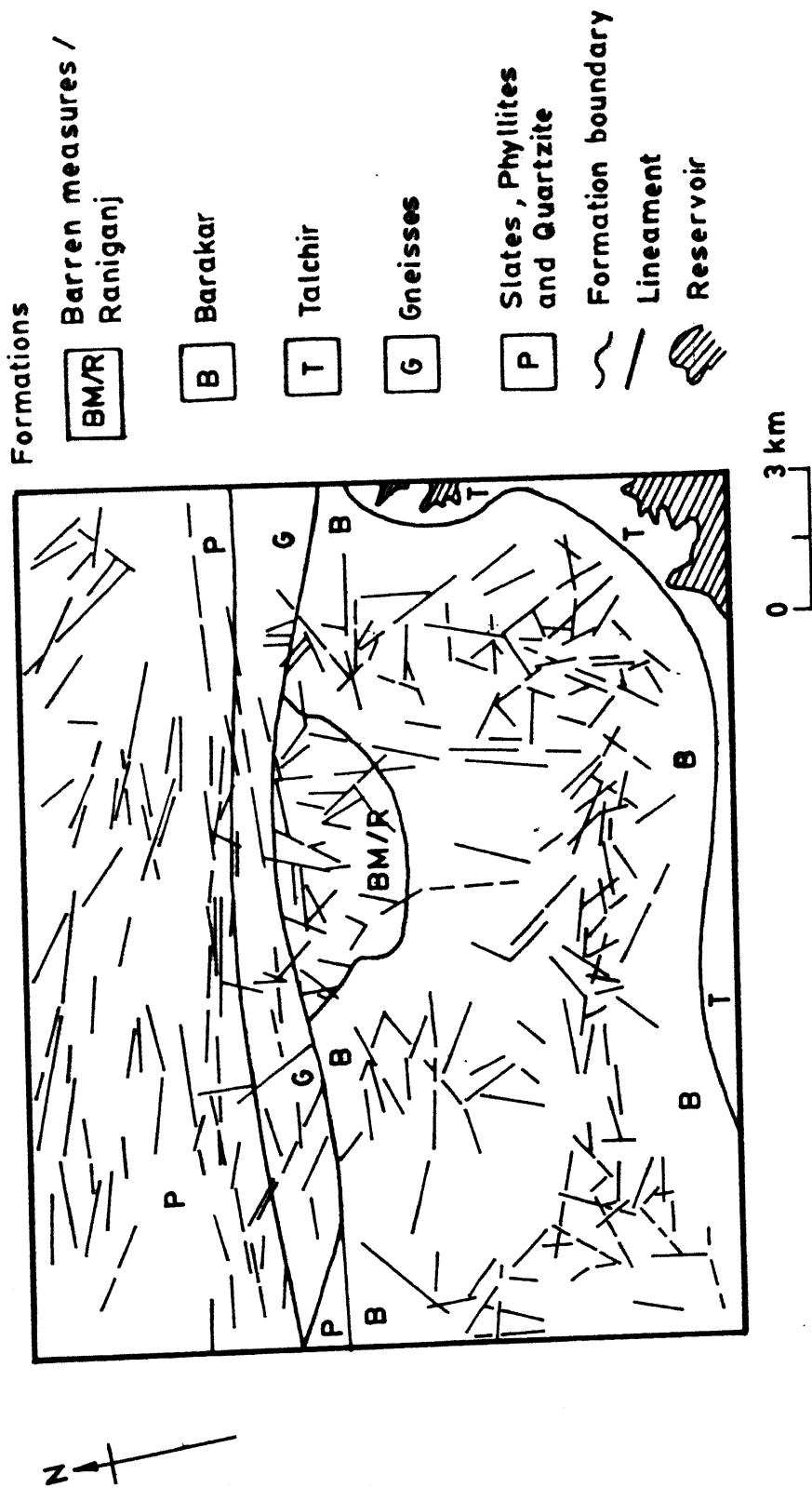


Fig.6.4 Lineament map of study area prepared using Morphedge Scheme

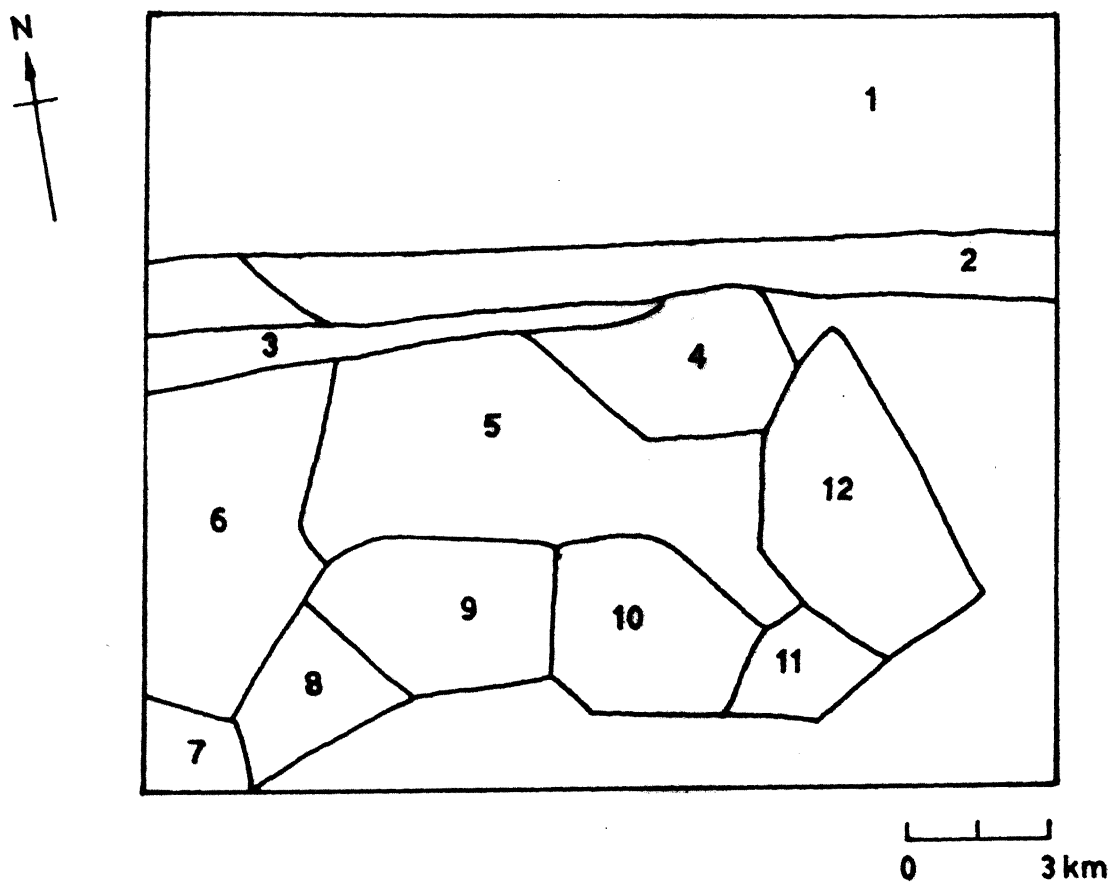


Fig. 6.5 Various zones demarcated based on visual interpretation for further analysis of lineaments

$$Y_r = \sum_{i=1}^n \sin \theta_i.$$

With the help of these resultants the mean direction is calculated as

$$\alpha = \tan^{-1} \frac{Y_r}{X_r}.$$

The magnitude of resultant is computed as

$$R = \sqrt{X_r^2 + Y_r^2}$$

The magnitude of resultant is standardized by dividing R by number of observations (n) thus obtaining mean resultant length (\bar{R}).

$$\bar{R} = R/n$$

The circular variance (S_o^2) is computed as

$$S_o^2 = 1 - \bar{R}.$$

With this information the circular standard deviation (σ_c) is estimated as

$$\sigma_c = [-2 \log_e(1 - S_o^2)]^{1/2}$$

Based on the mean resultant length (\bar{R}) concentration parameter (κ) for each zone is computed from chart (Batschelet, 1965).

The mean direction, orientation, mean resultant length, circular variance, circular standard deviation, concentration parameter and confidence angle as computed for both the lineament maps are presented in Tables 6.1 and 6.2.

(a) Test for dispersion

The mean resultant length (\bar{R}) generally ranges from 0 to 1. This produces a measure of dispersion. A large value of \bar{R} indicates that lineaments are tightly bunched with small dispersion.

Table 6.1: Statistical parameters for lineament analysis (Morphedge Scheme)

ZONE	Mean Direction (deg.)	Mean resultant length	Circular variance	Std. deviation	Conc. parameter (k)	Confidence angle (deg)
1	-73.65	0.95788	0.04	0.04	12.76610	2.27
2	89.30	0.78291	0.22	0.20	2.64613	9.38
3	81.45	0.91879	0.08	0.08	6.53940	8.26
4	54.60	0.59695	0.40	0.39	1.51574	15.55
5	-74.09	0.85469	0.15	0.14	3.91072	7.19
6	74.46	0.62386	0.38	0.36	1.60044	13.91
7	40.96	0.87015	0.13	0.12	4.17703	17.35
8	-83.09	0.76877	0.23	0.22	2.54686	11.36
9	83.00	0.74124	0.26	0.25	2.28930	10.67
10	-52.30	0.91276	0.09	0.08	5.85220	5.84
11	54.32	0.76120	0.24	0.23	2.45490	13.25
12	44.61	0.65529	0.34	0.33	1.78953	9.50

Table 6.2: Statistical parameters for lineament analysis (Digitedge Scheme)

ZONE	Mean Direction (deg.)	Mean resultant length	Circular variance	Std. deviation	Conc. parameter (k)	Confidence angle (deg)
1	-73.33	0.96137	0.04	0.04	12.76610	2.27
2	-69.34	0.88185	0.12	0.11	4.48876	10.88
3	-87.29	0.99797	0.00	0.00	50.24210	3.06
4	49.62	0.77259	0.23	0.21	2.54686	9.63
5	-86.07	0.76747	0.23	0.22	2.45490	9.33
6	-74.22	0.90537	0.09	0.09	5.30470	8.72
7	-55.48	0.98441	0.02	0.01	25.25220	5.75
8	-83.88	0.82597	0.17	0.16	3.14262	11.25
9	73.47	0.89212	0.11	0.10	4.85871	7.36
10	89.54	0.68895	0.31	0.30	1.95357	12.35
11	65.24	0.61215	0.39	0.38	1.55738	22.18
12	-55.70	0.74622	0.25	0.24	2.36930	9.19

It is obvious that values are high. This shows that the lineaments in all the zones are tightly bunched and have very small dispersion. Contrary to mean resultant length the circular variance has opposite meaning. A lower circular variance signifies lower dispersion and tightly bunched pattern. In the present case, it is evident that circular variance for all the zones in both the lineament maps are very nominal ranging from 0.002 to 0.403 (Tables 6.1 and 6.2). This implies that the lineaments are having minor dispersion.

The lineament density (λ) has been calculated from the following formula

$$\lambda = \frac{\sum l}{A}$$

where

$\sum l$ = total length of lineaments, and

A = area of the zone.

The results are shown graphically in Fig 6.6.

It is seen that lineament density is highest in zone 3 comprising of major boundary fault. In zones 4, 8, 9, 10, 11 and 12, the lineament density is quite high as compared to zones 1, 2 and 5. It is interesting to note that zones 4, 8, 9, 10, 11 and 12 are having huge coal deposits whereas later zones are barren of coal. Thus the coal bearing zones consist *larger density of lineaments* than the adjacent regions.

(b) Test of randomness of lineaments

Von Mises distribution is a circular equivalent to Gaussian distribution. This has two parameters, a mean direction (α) and a concentration parameter (κ). It is considered unimodal and symmetrical about the mean direction (Davis, 1986).

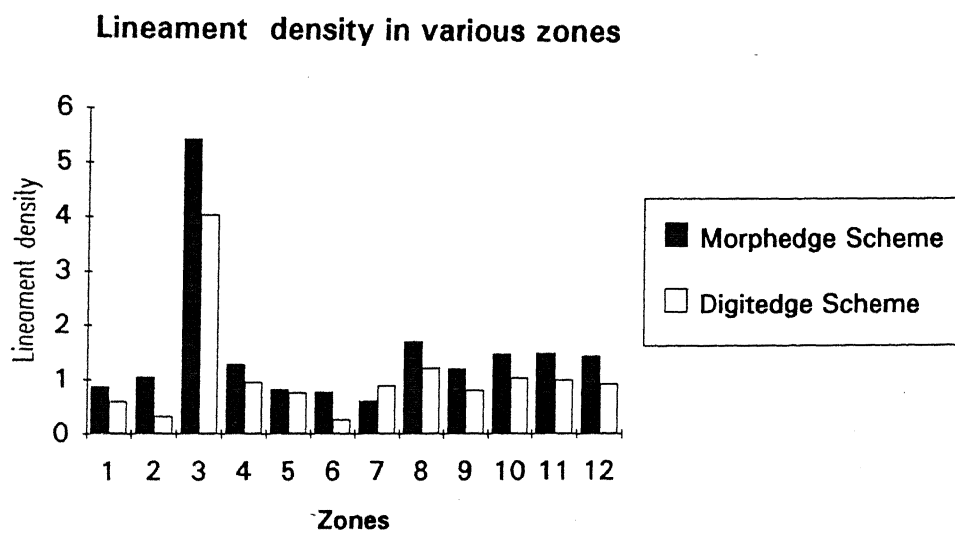


Fig. 6.6 Lineament density in various zones using Morphedge and Digitedge Scheme

As the concentration parameter increases, the probability of having directions of lineament very close to mean direction increases. This specifies a trend to the lineament pattern. On the other hand if concentration parameter is zero then all directions are possible and lineaments belong to a random phenomenon. Concentration parameters (κ) are listed in Tables 6.1 and 6.2.

This distribution is utilized to test the randomness of lineaments.

The null hypothesis is that

$$H_0 : \kappa = 0$$

$$H_1 : \kappa > 0,$$

ie if concentration parameter is zero then observations may have any direction and have no fixed trend, on the other hand $\kappa > 0$ specifies a trend or orientation. From Tables 6.1 and 6.2, it is evident that for all the zones in both the schemes, concentration parameter is not only greater than zero but also has high values thus indicating a *particular trend*.

Critical values of \bar{R} at 5% significance level for Rayleigh's test as computed from the chart (Mardia, 1972) are shown in Table 6.3.

The computed mean resultant length of lineaments are found more than the critical value of \bar{R} . Thus according to the Rayleigh's test the null hypothesis is rejected and a firm conclusion of having a preferred trend of lineament is established for all the zones.

(c) Test for a specified trend

In order to test that a population of vectors is characterized by a specified mean direction, Stephens (1969) proposed the use of extensive charts for determining critical values of direction. A simple approach is to determine confidence angle around the mean direction of samples and find if this interval encompasses the

Table 6.3 Critical orientation interval encompassing lineament directions

Zone	Critical orientation interval			
	Morphedge Scheme		Digitedge Scheme	
	Lower limit	Upper limit	Lower limit	Upper limit
1	-78.10	-69.20	-68.89	-77.78
2	70.91	107.69	-48.01	-90.68
3	65.25	97.65	-81.29	-93.28
4	24.12	85.08	68.49	30.75
5	-88.18	-59.99	-67.78	-104.37
6	47.20	101.71	-57.14	-91.30
7	6.95	74.97	-44.22	-66.74
8	-105.35	-60.84	-61.84	-105.92
9	62.09	103.91	87.88	59.05
10	-63.75	-40.85	113.74	65.34
11	28.34	80.3	108.71	21.77
12	25.98	63.24	-37.69	-73.71

hypothetical mean direction of samples (Davis, 1986).

Confidence angle (S_e), a parameter to evaluate the standard error of the mean direction is expressed in radians as

$$S_e = 1/\sqrt{n \bar{R} \kappa}$$

Using this parameter a probabilistic limit of population mean direction can be estimated. Here an assumption is made for the estimation, that errors are normally distributed and interval

$$\alpha \pm z_\beta S_e$$

should comprise of the true population mean direction β % of the times. To allow a 95% probability to have a population mean the interval is computed as

$$\alpha \pm 1.96 S_e$$

Here α and S_e are in degrees.

The values of confidence angles and the critical intervals encompassing lineament directions are illustrated in Table 6.3.

The strike direction of bedding planes in zone 1 is essentially WNW as depicted in geological maps. This is in conformity with the values shown in Table 6.3.

Zone 2, comprising of granite and gneisses, is having orientations in ESE and NE to ENE. This is also within the computed interval of orientation from the lineament map using Morphedge schemes. In Digitedge scheme the trend did not match as the number of observations (lineaments) were very little on the map produced using this scheme as compared to Morphedge scheme .

Zone 3 is mainly comprising of the major northern boundary fault between Barakars and metamorphics. It is having major trend in EW direction and deflects

ESE in the latter half (Raja Rao, 1983). This is in conformity with the inference made in Table 6.3.

Zone 4 essentially consists of Jingurdah area. This area is marked by number of faults in N-S, NNE and ENE directions. Directions obtained are 30.75° - 68.49° for Digitedge and 24.12° - 85° for Morphedge schemes (Table 6.4).

Zone 5 lies to the west of Jingurdah area. It has lineaments oriented in NW (59.99° - 88.17°) according to Morphedge scheme and NW (67.77° - 104.36°) according to Digitedge scheme.

Zones 6 and 7 have trend in NW and SE according to both the schemes of lineament mapping.

From earlier works in field (Raja Rao, 1983) it is found that beds in western part of study zone have a general NW - SE trend.

Zone 8 contains approximately Nigahi and Jayant blocks. The beds have NW and SE trend (Raja Rao, 1983). Values in Table 6.4 also indicate their mean directions as NW and SE.

Zones 9 and 10 are within the Dudhichua and Khadia blocks, and are having ENE trend along with critical values of direction being NE and SE (Table 6.4). This is supported by the field observations that general strike of beds is in NE - SW direction.

Zone 11 comprises a part of Khadia block having mean direction as 65.25° (Digitedge scheme) and 54.32° (Morphedge scheme). Earlier workers have found out that strike in eastern part of Khadia area is trending in NE direction which supports the above result.

Zone 12 comprises Bina, Kakri and Marrak coalfields. Here the mean direction of lineament is found as 44.61° in Morphedge scheme. The critical limit of angles ranges from 25.98° to 63.23° . The lineament patterns are governed by the strike of

beds and fractures which are having a NE orientation. The Bina block is having NS bed strike direction which changes to N and SW in Marrak region. Within the Kakri block, this takes a swing to NE (Raja Rao, 1983).

6.4 Geological Map from Digitally Processed Satellite Data

In Chapter 3, structural mapping of the study area has been carried out using FCCs and LANDSAT-TM Band 7 imagery. It has been realized that for better delineation of structural features, a dedicated approach of image processing is required. Based on the mathematical morphology, a scheme of enhancing structural features is proposed here.

Images generated by top hat transformations in Chapter 5 have been used in following scheme to map out the faults, joints, fractures etc. The procedure is outlined with the help of a flow chart in Fig 6.7.

The top hat images at 60° , 120° , 30° , 90° and 150° are the input images for delineation of faults. An *auxiliary image set* was utilized to confirm the fault and discriminate it from other linear cultural features. This set comprised *the top hat superimposed images* using plus shape structuring element and diagonal structuring elements at 45° and 135° . A map prepared based on these images is presented in Fig 6.8. As indicated in the map, a large number of faults within the coal mine zones could be delineated along with the structural lineaments in slate and phyllite zone in northern part of the study area. Since mining is in progress, extensive geological mapping is conducted in field for each of the mining blocks by CMPDI. The maps prepared by this organization show faults, joints etc. in detailed manner. The details indicated in Fig 6.8 are compared with available map (D.G./3535, CMPDI). It is found that most of the interpretations are correct.

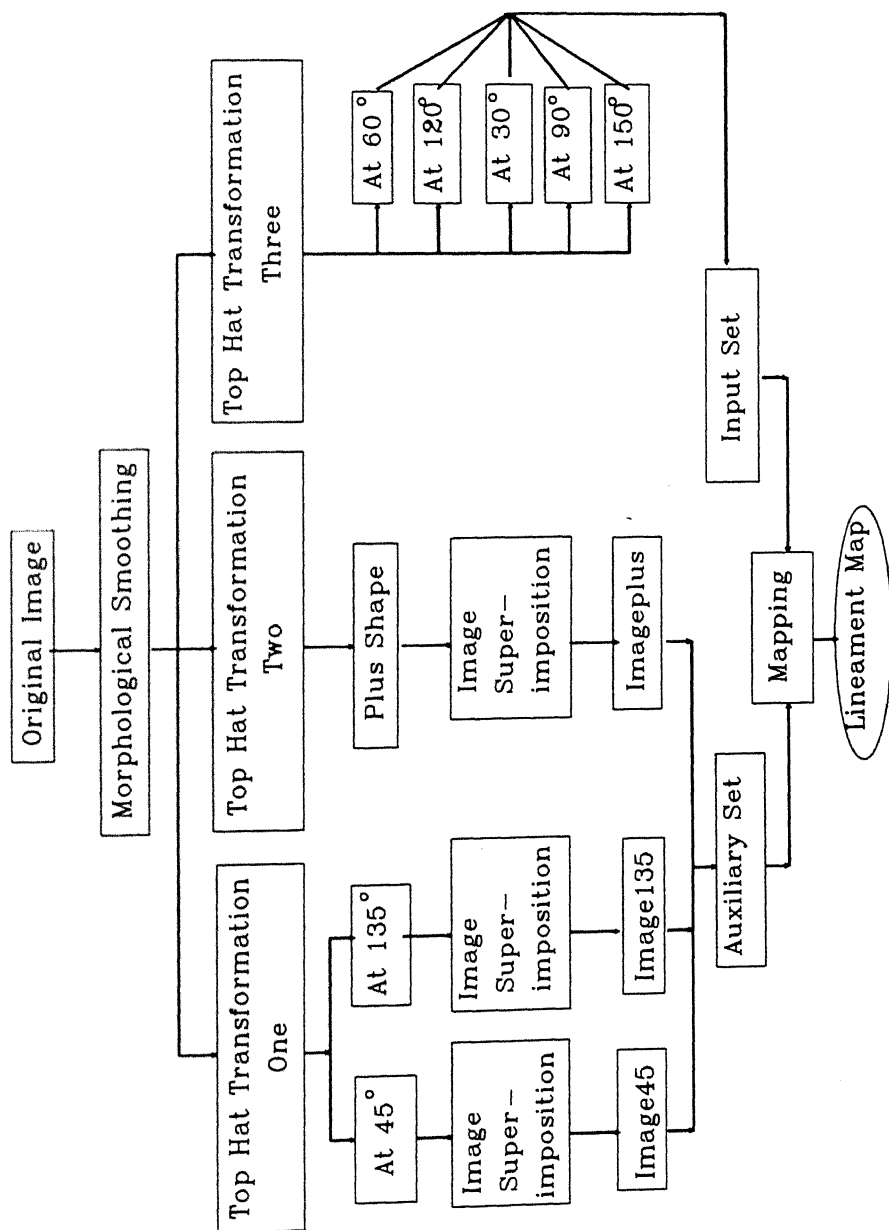


Fig. 6.7 Image processing scheme to map structural features

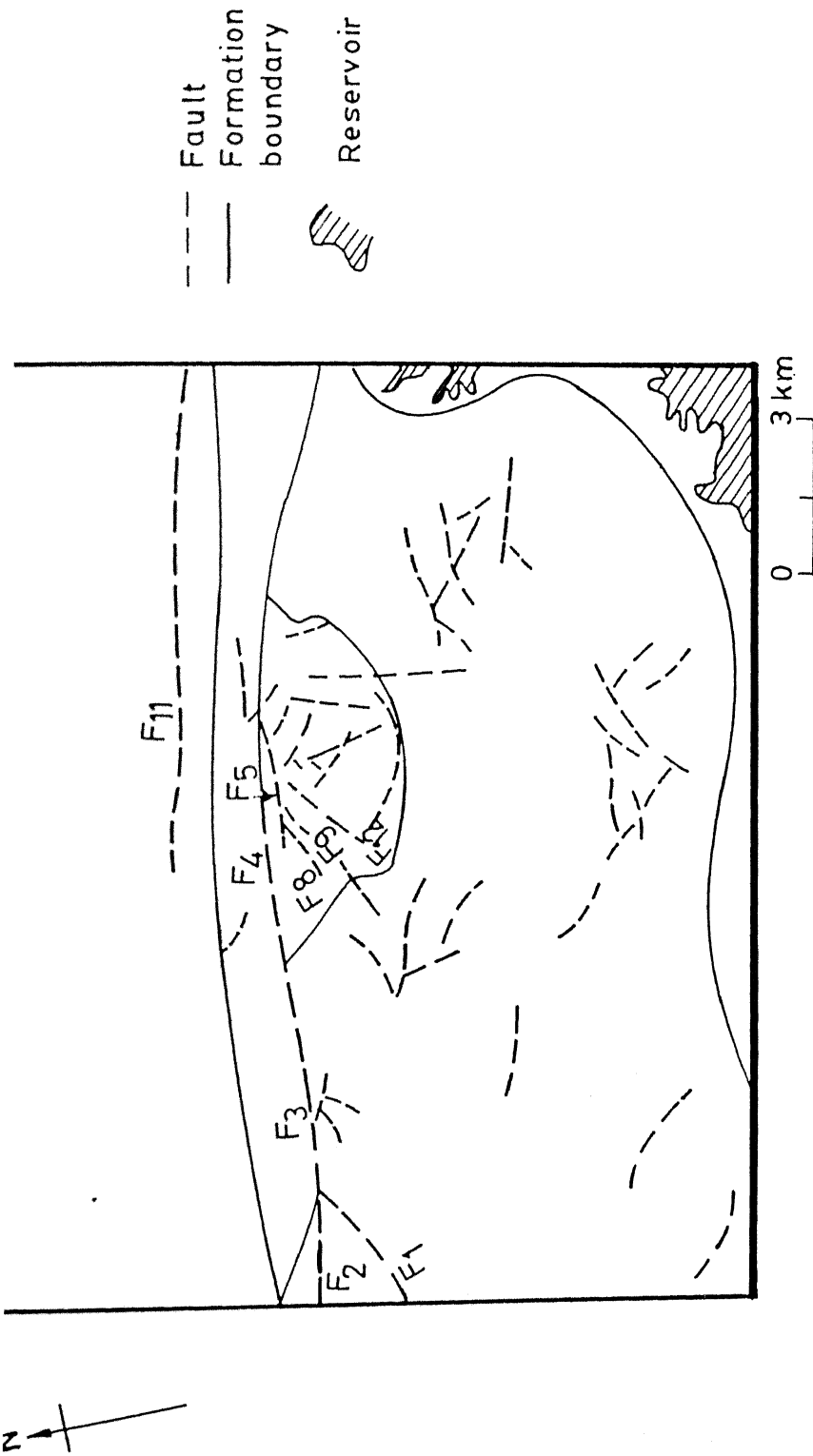


Fig. 6.8 Geostructural details of the study area using morphologically processed satellite images

6.5 Accuracy Estimation of the Geostructural Map

A statistical estimation of the accuracy of the *final geostructural map* shown in the Fig. 6.8 has been carried out in order to evaluate the usefulness of the proposed digital image processing techniques for lineament enhancement and delineation. The final map is compared and analysed with respect to the *base map of the area* (Fig. 1.2) taken as the *reference*.

The 12 faults present on the base map have been assigned identification numbers as F_1 , F_2 , F_3 , ..., F_{12} . These are also marked on the *final geostructural map*. The length of the faults and their orientation with respect to north in the base map as well as in the final map are listed in the Table 6.4. The percentage linear and angular accuracies of the observed faults on the *final geostructural map* as estimated with reference to the *base map of the area* using the following expressions are presented in Table 6.4.

$$\text{Absolute Linear Error, } \epsilon_L = | (L_B - L_F) / L_B |$$

$$\text{Percentage Linear Accuracy} = (1 - \epsilon_L) * 100$$

$$\text{Absolute Angular Error, } \epsilon_\theta = | (\theta_B - \theta_F) / \theta_B |$$

$$\text{Percentage Angular Accuracy} = (1 - \epsilon_\theta) * 100$$

where

L_B = the length of fault in the base map,

L_F = the length of fault in the final geostructural map,

θ_B = the orientation of the fault from the north in the base map, and

θ_F = the orientation of the fault from the north in the final geostructural map.

Table 6.4 Estimation of accuracy of the final geostructural map

Fault	Base Map		Final Map		Abs. Linear Error	Abs. Angular Error	Linear Accuracy	Angular Accuracy
	L_B (m)	θ_B (deg)	L_F (m)	θ_F (deg)	ϵ_L	ϵ_θ	%	%
F_1	3240	71	2850	62	0.12	0.13	88	87
F_2	2268	102	2250	100.5	0.10	0.10	90	90
F_3	6372	92	4950	92	0.22	0.00	78	100
F_4	3780	102	3150	95	0.17	0.07	83	93
F_5	2160	94	2550	91	0.18	0.03	82	97
F_6^*	2160	2	-	-	-	-	-	-
F_7^*	1836	173	-	-	-	-	-	-
F_8	1188	66	1350	66	0.14	0.00	86	100
F_9	1088	40	1050	51	0.03	0.28	97	72
F_{10}^*	1188	52	-	-	-	-	-	-
F_{11}	6480	91	7950	100	0.23	0.10	77	90

* *not present in the final geostructural map*

It is observed that out of the 12 faults indicated in base map, only 9 could be demarcated in the final map. In the case of fault F_{12} (Fig. 6.8), its orientation $N 50^\circ$ as delineated in the final map tallies with its orientation indicated in the base map. The angular accuracy thus works out as 100 percent. However, the length of this fault as inferred in the present work and indicated on the final map is 2250 m while in the base map it was shown as 1080 m in length. It may be noted that this fault F_{12} is located in Jingurdah coal mine area which has undergone intensive opencast mining since 1982 (when the reference base map was prepared) resulting in the additional exposed length of the fault. In general, the faults (F_5 , F_8 , F_{12}) located in the Jingurdah coal mine area have been inferred to have enhanced lengths on the final map compared to plots on the base map.

Using the proposed *morphedge* scheme for lineament detection, 36 additional new faults have been delineated which were not present on the reference map. Field checks in selected areas have confirmed their presence.

Chapter 7

SUMMARY AND CONCLUSIONS

The study area forms a part of the Singrauli coal field. Typical of the Gondwana coal basins, the Singrauli basin exhibits distinct tectonic setting. The northern boundary is a faulted one bringing the Precambrian metamorphic formations in juxtaposition with the Barakar and Raniganj formations (Permian) of the lower Gondwana sequence. Besides this boundary fault, several other intrabasinal normal faults of varying magnitude and with a discernible pattern are recognized. These are, in general, aligned along NW - SE, NE - SW and E - W trends. According to Verma and Singh (1980), there is a genetic relation between the faults and the basement structure in the Gondwana basins. In the Singrauli coal basin, the tilt of the sediments towards the boundary fault in the north is very clearly observed from the nature of the dips of the formations. Thus, in the study area, structural setting is complex resulting in diverse directional features.

While choosing the digital image processing techniques for evaluation in the present study as tools for structural mapping, the structural setting of the coal field was kept in mind especially in regard to the directional trends of the linear features which necessitate directional and nonlinear filtering.

In the present study, data from four bands of IRS 1B - LISS- and band 7 of LANDSAT-TM have been utilized. Since the data belong to the two different satellites, preprocessing has been performed to establish compatibility. Geometric rectification of the data has been conducted using quadratic mapping function. Image resampling of LANDSAT-TM data was carried out using nearest neighbourhood technique. In order to reduce the dimensionality of dataset and to preserve

the maximum information content, principal component analysis is performed. The data distributed in five bands could be compressed into three components (1, 2 and 4) containing 94.16 percent information.

Two false colour composites using IRS DATA (Bands 1,2,4 and 1,3,4) are generated. In addition, principal components 1,2 and 4 were used for the generation of FCC. These FCC's have enabled the preparation of lithological- structural map and the geomorphological map of the area. The formation boundaries, as also the EW trending major boundary fault along with several intraformational faults, could be located visually.

Several geomorphic units are identified such as the structural ridges in the Precambrian terrain, mesa and butte features within the Barakars along with pediment zones and pediplains. Structural control of the drainage is confirmed.

To bring out the structural features clearly, an extensive study of tools of digital image processing was undertaken based on which a Digitedge scheme for lineament detection is proposed. This scheme involves image smoothing, edge detection and edge linking operation. Pseudomedian filtering for image smoothing was found to be efficient in the removal of sporadic noises and in preserving the edges. Moving average and sigma filtering did not yield satisfactory results. Median filtering rendered equally good result as of pseudomedian filtering but involved more computational time. Edges are extracted using Frei-Chen operator. This operator has detected edges equally well in horizontal, vertical and inclined directions. Prewitt operator could not detect several edges in inclined directions while Sobel operator failed to detect some edges in horizontal / vertical directions. Edges produced by both these operators were thick compared to those with Frei-Chen operator which yielded fine edges, facilitating mapping of the lineaments. Laplacian and entropy- based filters did not yield desirable result. Edge image produced by Laplacian is useful only

for preliminary assessment of edges. This operator fails in the case of ramp edges commonly evidenced in an imagery due to shadow effects. Entropy- based filter could not be used in the present study as it yielded limited edges. Edge linking operation is performed on edge output obtained using Frei-Chen operator for connecting the minor discontinuities in edges. The final edge linked output is used for lineament mapping. A lineament map has been prepared using this scheme. It has been observed that limited fault demarcation could be achieved with this scheme.

Morphedge scheme, based on morphological transformation has been adopted. Morphological transformation for image smoothing and edge detection have been used. Image smoothing used was based on neighbourhood criterion. Edges were preserved and noise content was reduced. The smoothed output obtained has been used for edge detection. Top hat transformations using hexagonal structuring elements in various directions (0° , 30° , 60° , 90° , 120° and 150°) have been used for extracting edges. The results obtained were found to be remarkably efficient for mapping of lineaments and faults.

This transformation was further modified by including image superimposition technique. The output obtained using this method was better suited for locating structural features and discriminating them with the physical objects since vegetation, surface water bodies and moisture zones have been superimposed on top hat transformed image output.

The lineaments map prepared using the Morphedge scheme has indicated higher density of lineaments. In the present study, the lineament density is more in coal mine areas.

A statistical analysis of lineaments obtained on these maps has been carried out. The results of test for dispersion showed that lineaments in all the zones are tightly bunched as evidenced from the range of circular variance (0.002 - 0.403). A

preferred trend of lineaments has also been evidenced from the randomness test.

The trend of lineaments, as obtained in the statistical analysis are in conformity with the trends reported earlier (Raja Rao, 1983). It is seen that the strike direction of rocks in various zones is confirming within the interval of critical orientations. Faults delineated using the morphological transformations are indicated in a map prepared during the study.

The present work has, thus, brought out the superiority of pseudomedian filtering for image smoothing over other smoothing techniques and the suitability of morphological image transformation for fault and lineament delineation compared to the digital filtering technique.

REFERENCES

- Barrett, E. C. and Curtis, L. F. *Introduction to Environmental Remote Sensing*, Third edition, Chapman and Hall, 1992.
- Basu, T. N. and Shrivastava, B. B. P. Structure and tectonics of Gondwana basins of peninsular India, *Proc. Fifth International Gondwana Symposium*, Wellington, New Zealand, 1980.
- Batschelet, E. *Statistical methods for the analysis of problems in animal orientation and certain biological rhythms: American Institute of Biological Sciences Monograph*, Washington, D. C., 57 p., 1965.
- Coal Mining in India, *Report of the 12th World Mining Congress*, New Delhi, India, Central Mine Planning and Design Institute, Ranchi, Bihar, India, Nov. 1984.
- Data Users Handbook (Revision 1)*, Indian Remote Sensing Satellite, Department of Space, Government of India, Dec. 1989. Davis, J. C. *Statistical and Data Analysis in Geology*, John Wiley, New York, 1986.
- Duda, R. O. and Hart, P. E. *Pattern Classification and Scene Analysis*, Wiley, New York, 1973.
- Dutta, K. K. and Mukherjee, K. N. Paleoslope control of differential deposition of coal in two adjacent sub-basins in the Singrauli coalfield, India, *Proc. IV International Gondwana Symposium*, Vol. 1, pp. 278-285., 1979.
- Frei, W. and Chen, C. C. Fast boundary detection: a generalization and a new algorithm, *IEEE Trans. on Computers*, Vol. C-26, No. 10, pp. 988-997, 1977.

- Ganesha Raj, K. and Gupta, A. K. Hydrogeomorphological mapping of Kasaragod district using LISS-II, *Bhu-Jal News*, Vol. 5, No. 4, pp. 28-31, 1990.
- Giardina, C. R. and Dougherty, E. R. *Morphological Methods in Image and Signal Processing*, Prentice Hall, New Jersey, 1988.
- Gonzalez, R. C. and Wintz, P. *Digital Image Processing*, Addison Wesley, Massachusetts, 1977.
- Heurtas, A. and Medioni, G. Detection of intensity changes using Laplacian-Gaussian masks, *IEEE Trans. on Pattern Analysis and Machine Intelligence*, PAMI-8, No. 5, pp. 651-664, 1986.
- Huang, T. S. *Two-Dimensional Digital Signal Processing-II*, Springer-Verlag, Berlin, 1981.
- Jensen, J. R. *Introductory Digital Image Processing*, Prentice-Hall, New Jersey, 1986.
- Jolliffe, I. T. (ed.) *Principal Component Analysis*, Springer-Verlag, New York, 1986.
- Joshi, K. C. and Pant, A. Coal resources of India, *Memoirs Geological Survey of India*, Vol. 8, pp.291-298, 1971.
- Kirsch, R. Computer determination of constituent Structure of Biomedical Images, *Computers and Biomedical Research*, Vol. 4, No. 3, pp. 315-328, 1971.
- Klein, J. C. and Serra, J. The texture analyser, *Journal of Micr.*, 95, part 2, pp. 349-356, 1973.
- Krishnamurthy, J. Delineation of Deccan Trap outcrop extensions using satellite

- Nagao, M. and Matsuyama, T. Edge preserving smoothing, *Computer Graphics and Image Processing*, 9, pp. 394-407, 1979.
- Newton, A. R. and Boyle, T. P. Discriminating rock and surface types with multispectral satellite data in the Richtersveld, NW Cape Province, South Africa, *International Journal of Remote Sensing*, Vol. 14, No. 5, pp. 943-959, 1993.
- Paine, S. H., Lodwick G. D. Edge detection and processing of remotely sensed digital images, *Photogrammetria (PRS)*, 43, pp. 323-336, 1989.
- Pant, A. and Basu, A. Geology of Northern part of Singrauli Coalfield, District Sidhi, Madhya Pradesh, *Prog. Rept. Geol. Surv. Ind.*, 1965-66, 1967. Pant, A. and Shome, S. K. Geology of the northern part of the singrauli Coalfield, District Sidhi, M. P., *Prog. Rept. Geol. Surv. Ind.*, 1961-62, 1963
- Peli, T. and Malah, D. A study of edge detection algorithms, *Computer Graphics and Image Processing*, Vol. 20, pp. 1-21, 1982.
- Pratt, W. K. *Digital Image Processing*, II ed., John Wiley, New York, 1991.
- Pratt, W. K. *Digital Image Processing*, John Wiley, New York, 1978.
- Pratt, W. K. Cooper, T.J, and Kabir, I. Pseudomedian filter, Proc. SPIE conference, Los Angeles, CA, 1984.
- Prewitt, J. M. S. Object enhancement and extraction, *Picture Processing and Psychopictorics*, B. S. Lipkin and A. Rosenfield (eds.), Academic Press, New York, 1970.
- Raja Rao, C. S. (ed.) Coalfields of India, Vol. III, coal resources of M. P., J and K, *Bulletins of the Geological Survey of India*, 1983

- Ramakrishnan, R., Kumar, S., and Bhatt, IRS data products system. *User CCT formats for IRS data products*, SAC, Ahmedabad, IRS/SAC, DP/TN-08/88, 1988.
- Robinson, G. S. Edge detection by compass gradient mask, *Computer Graphics and Image Processing*, 6, pp. 492-501, 1977.
- Rosenfield, A and Kak, A. C. *Digital Picture Processing*, II ed., Academic press, New York, 1982.
- Salim, M. Some aspects of morphological operations for image analysis, *M. Tech. Thesis, I. I. T. Kanpur, India*, 1991.
- Serra, J. Image Analysis and Mathematical Morphology, Academic Press Inc. (London) Ltd., 1982.
- Serra, J. Introduction to mathematical morphology, *Computer Vision Graphics and Image Processing*, Vol. 35, pp. 283-305, 1986.
- Shiozaki, A. Image enhancement in a dethereed picture, *Computer Vision Graphics and Image Processing*, 24, pp. 107-113, 1983.
- Sinha, A. K., Srivastava, V.C., and Nagar, M. Land degradation around Singrauli-an observation, *Proc. IV Congress International Association of Engg. Geology*, Vol. 1, pp. I.57 to I.68, 1982.
- Smith, M. W. and Davis, W. A. A new algorithm for edge detection, *Computer Graphics and Image Processing*, 4, pp. 55-62, 1975.
- Stephens, M. A. Tests for randomness of directions against two circular alternatives, *Journal of American statistical association*, Vol. 64, No. 325, pp. 280-289, 1969.

Sternberg S. R. Grayscale morphology, *Computer Vision Graphics and Image Processing*, 35, pp. 333-355, 1986.

Tukey, J. W. *Exploratory Data Analysis*, Addison-Wesley, Reading, Mass., 1971.

Verma, R.N.P. and Singh, V. K. Fold tectonics in Gondwana formations of India, *Fifth International Gondwana Symposium*, Wellington, New Zealand, 1980.

Wang, David C. C., Vagnucci, A. H., and Li, C. C. Image enhancement by gradient inverse weighted smoothing scheme, *Computer Graphics and Image Processing*, 15, pp. 167-181, 1981.

BIBLIOGRAPHY

- Abdou, I. E. and Pratt, W. K. Quantitative design and evolution of enhancement / thresholding edge detectors, *Proc. IEEE*, Vol. 67, No. 5, pp. 753-763, 1979.
- Blodget, H. W., Gunther, F. J., and Podwysocki, M. H. Discrimination of rock classes and alteration products in south western Saudi Arabia with computer - enhanced Landsat data, *NASA Technical paper*, 1327 p., 1978.
- Brooks, M. J. Rationalizing edge detectors, *Computer Graphics and Image Processing*, 8, pp. 277-285, 1978.
- Carrere, V. Dev. of multiple source data processing for structural analysis at a regional scale, *Photogrammetric Engineering and Remote Sensing*, Vol. 56, pp. 587-595, 1990.
- Carrol, S. and Robinson J. E. Homomorphic processing of LANDSAT data, *Canadian Journal of Remote Sensing*, Vol. 3, No. 1, pp. 66-75, 1977.
- Chavez, P. and Bauer, B. An automatic optimum kernel-size selection technique for edge enhancement, *Remote Sensing of Environment*, Vol. 12, pp. 23-38, 1982.
- Chittineni, C. B. Edge and line detection in multidimensional noisy imagery data, *IEEE Trans. on Geoscience and Remote Sensing*, GE-21, No. 2, pp. 163-174, 1983.
- Chorowicz, J. Dip and strike measured systematically on digitized 3-D geological maps, *Photogrammetric Engineering and Remote Sensing*, Vol. 57, No. 4, pp. 431-436, 1991.

- Choubey, V. D. and Shankarnarayana, I. Evaluation of aquifer behavior and characteristics in the Singrauli coalfield, Central India, *Ground Water*, Vol. 28, No. 6, pp. 893-899, 1990.
- Cumani, A. Edge detection in multispectral images, *Computer Vision Graphics and Image Processing: Graphical Models and Image Processing*, Vol. 53, No. 1, pp. 40-51, 1991.
- Davies, E. R. Circularity - a new principle underlying the design of accurate edge orientation operators, *Image and Vision Computing*, Vol. 2, No. 3, pp. 134-142, 1984.
- Davis, L. S. A survey of edge detection techniques, *Computer Graphics and Image Processing*, 4, pp. 248-270, 1975.
- Defee, I. and Neuvo, Y. Median based zero-crossing edge detectors for closely spaced edges, *Computer Vision Graphics and Image Processing*, Vol. 53, No. 2, pp. 196-203, 1991.
- Deutsh, M. A quantitative study of the orientation bias of some edge detector schemes, *IEEE Trans. on Geoscience and Remote Sensing*, 3, pp. 205-213, 1978.
- Eberlein, R. B. An iterative gradient Edge detection algorithm, *Computer Graphics and Image Processing*, 5, pp. 245-253, 1976.
- Gilmour, T. Image smoothing as an aid to classification, *Proc. of 13th annual conference of the Remote sensing soc. of Nottingham*, pp. 56-68, 1987.
- Haralick, S. *Digital Image Processing*, D. Reidel, Holland, 1980.
- Ikonopolous, A. An approach to edge detection based on the direction of edge

- element, *Computer Graphics and Image Processing*, Vol. 19, pp. 179-195, 1982.
- Jeng-Jong Pan Spectral analysis and filtering technique in digital spatial data processing, *Photogrammetric Engineering and Remote Sensing*, Vol. 55, No. 8, pp. 1203-1207, Aug. 1989.
- Justusson, B. I. Median filtering: Statistical Properties, *Two-Dimensional Signal Processing-II*, T. S. Huang (ed.), Springer-Verlag, Berlin, pp. 161-195, 1981.
- Jutz, S. L. and Chorowicz, J. Geological mapping and detection of oblique extensional structures in the Kenyan rift valley with SPOT/LANDSAT-TM data merge, *International Journal of Remote Sensing*, Vol. 14, No. 9, pp. 1677-1688, 1993.
- Karpuz, M. R., Olesen, O., Roberts, D., Gabrielsen, R. H., and Herrevold, T. Application of multiple data sets to structural studies on varanger Peninsula, Northern Norway, *International Journal of Remote Sensing*, Vol. 14, No. 5, pp. 979-1003, 1993.
- Levialdi, S. Edge extraction techniques, *Fundamentals on computer vision: an advanced course*, O.D. Faugeras (ed.), Cambridge Univ. Press., Cambridge, 1983.
- Lyberis, N. Geological features of Sptisbergen region obtained from multispectral SPOT data and field radiometer measurements, *International Journal of Remote Sensing*, Vol. 11, No. 2, pp. 253-265, 1990.
- Mather, P. M. *Computer Processing of Remotely-Sensed Images*, John Wiley, New York, 1987.
- Mering, C. and Debaine, F. Analysis of satellite image applied to archaeological research in north-west India : Delineation of linear networks, *Proc. of Ninth Asian Conf. on Remote Sensing*, Bangkok, Thailand, pp. B-2-1 to B-2-8, 1988.

- O'Gorman, L. $K \times K$ Thinning, *Computer Vision Graphics and Image Processing*, 51, pp. 195-215, 1990.
- Peddle, D. R. and Franklin, S. E. Gedemon: a Fortran-77 program for restoration and derivative processing of digital image data, *Computers and Geosciences*, Vol. 16, No. 5, pp. 669-696, 1990.
- Persoon, E. A new detection algorithm and its application in picture processing, *Computer Graphics and Image Processing*, 5, pp. 425-446, 1976.
- Qari, M. Y. H. T. Application of LANDSAT-TM data to geological studies, Al Khabt area, Southern Arabian shield, *Photogrammetric Engineering and Remote Sensing*, Vol. 57, No. 4, pp. 421- 429, 1991.
- Qari, M. Y. H. T. Lithological mapping and structural analysis of Proterozoic rocks in part of the southern Arabian shield using LANDSAT images, *International Journal of Remote Sensing*, Vol. 10, No. 3, pp. 499-503, 1989.
- Rathore, C. S. and Wright, R. Monitoring environmental impacts of surface coal mining, *International Journal of Remote Sensing*, Vol. 14, No. 6, pp. 1021-1042, 1993.
- Riaza, A. Study of precambrian detritic rocks for structural analysis in the visible and near-infrared, *International Journal of Remote Sensing*, Vol. 14, No. 5, pp. 927-942, 1993.
- Roberts, J. L. *Introduction to geological maps and structures*, Pergamon Press, 1982.
- Rothary, D. A. Improved discrimination of rock units using Landsat thematic mapper imagery of the Oman ophiolite, *J. Geol. Soc. London*, 144: pp. 587-597,

1987.

Rothary, D. A. Decorrelation stretching and related techniques as an aid to image interpretation in geology, *Proc. of 13th annual conference of the remote sensing soc.*, Univ. of Nottingham., pp. 194-203, 1992.

Shaw, G. B. Local and regional edge detectors: some comparisons, *Computer Graphics and Image Processing*, 9, pp. 135-149, 1979.

Shiozaki A. Edge extraction using entropy operator, *Computer Vision Graphics and Image Processing*, 36, PP. 1-9, 1986.

Tabatabai, A. J. Edge location to subpixel values in digital imagery, *IEEE Trans. on Pattern Analysis and Machine Intelligence*, PAMI-6, No.2, pp. 188-201, 1984.

Verma, P. K. Tectonic inferences from the statistical treatment of the remote sensing lineament fabric data associated with the great boundary fault of Rajasthan, India, *Journal of Indian Soc. of Remote Sensing*, Vol. 21, No. 2, pp. 67-74, 1993.

Wang, David, C. C., Vagnucci, A. H., and Li, C. C. Digital Image enhancement: A survey, *Computer Vision Graphics and Image Processing*, 24, pp. 363-381, 1983.

White, K. Image processing of Thematic Mapper data for discriminating piedmont surficial materials in the Tunisian Southern Atlas, *International Journal of Remote Sensing*, Vol. 14, No. 5, pp. 961-977, 1993.

APPENDIX - A

Table A-1 : Statistical details of lineaments extracted using Morphedge Scheme

Precambrian Formations			
ZONE # 1 (Slate and Phyllite)			
length (m)	angle (θ) ^o	cos θ	sin θ
600	122	-0.52992	0.84805
900	122	-0.52992	0.84805
1650	100	-0.17365	0.98481
1050	100	-0.17365	0.98481
1200	100	-0.17365	0.98481
1200	100	-0.17365	0.98481
2400	100	-0.17365	0.98481
1200	100	-0.17365	0.98481
1950	90	0.00000	1.00000
900	90	0.00000	1.00000
1050	90	0.00000	1.00000
1050	90	0.00000	1.00000
1650	110	-0.34202	0.93969
3000	110	-0.34202	0.93969
3300	110	-0.34202	0.93969
900	110	-0.34202	0.93969
750	110	-0.34202	0.93969
1200	104	-0.24192	0.97030
1200	104	-0.24192	0.97030
1200	104	-0.24192	0.97030
600	104	-0.24192	0.97030
1650	108	-0.30902	0.95106
1200	108	-0.30902	0.95106
1350	108	-0.30902	0.95106
1050	108	-0.30902	0.95106
900	108	-0.30902	0.95106
1050	101	-0.19081	0.98163
1650	101	-0.19081	0.98163
2400	101	-0.19081	0.98163
1200	101	-0.19081	0.98163
1200	96	-0.10453	0.99452
750	96	-0.10453	0.99452
2550	96	-0.10453	0.99452
1350	96	-0.10453	0.99452
1050	84	0.10453	0.99452
1500	84	0.10453	0.99452

3000	91	-0.01745	0.99985
1200	91	-0.01745	0.99985
900	112	-0.37461	0.92718
750	112	-0.37461	0.92718
1050	112	-0.37461	0.92718
900	120	-0.50000	0.86603
2400	94	-0.06976	0.99756
450	94	-0.06976	0.99756
1350	94	-0.06976	0.99756
1500	86	0.06976	0.99756
3150	146	-0.82904	0.55919
900	152	-0.88295	0.46947
1050	160	-0.93969	0.34202
1050	138	-0.74314	0.66913
1050	138	-0.74314	0.66913
1050	142	-0.78801	0.61566

ZONE # 2 (Gneisses)

1650	154	-0.89879	0.43837
1500	102	-0.20791	0.97815
450	102	-0.20791	0.97815
1050	126	-0.58779	0.80902
1050	126	-0.58779	0.80902
600	126	-0.58779	0.80902
1050	126	-0.58779	0.80902
1050	96	-0.10453	0.99452
1500	96	-0.10453	0.99452
1200	84	0.10453	0.99452
900	84	0.10453	0.99452
1500	84	0.10453	0.99452
5400	89	0.01745	0.99985
600	26	0.89879	0.43837
450	26	0.89879	0.43837
450	26	0.89879	0.43837
450	10	0.98481	0.17365
900	88	0.03490	0.99939

ZONE # 3 (Boundary fault)

2400	96	-0.10453	0.99452
750	96	-0.10453	0.99452
1950	90	0.00000	1.00000
1350	96	-0.10453	0.99452
900	96	-0.10453	0.99452
1950	90	0.00000	1.00000
1050	34	0.82904	0.55919
750	47	0.68200	0.73135

Gondwana Formations

ZONE # 4 Raniganj Formations

900	114	-0.40674	0.91355
1050	30	0.86603	0.50000
1050	24	0.91355	0.40674
750	24	0.91355	0.40674
450	24	0.91355	0.40674
750	32	0.84805	0.52992
750	32	0.84805	0.52992
1200	90	0.00000	1.00000
750	2	0.99939	0.03490
900	2	0.99939	0.03490
750	2	0.99939	0.03490
1050	118	-0.46947	0.88295
1050	160	-0.93969	0.34202
900	160	-0.93969	0.34202
1200	111	-0.35837	0.93358

ZONE # 5 (Barren Measures and Barakars)

1650	121	-0.51504	0.85717
1050	121	-0.51504	0.85717
750	70	0.34202	0.93969
750	58	0.52992	0.84805
600	94	-0.06976	0.99756
1500	90	0.00000	1.00000
750	156	-0.91355	0.40674
600	140	-0.76604	0.64279
600	154	-0.89879	0.43837
600	112	-0.37461	0.92718
1050	91	-0.01745	0.99985
600	92	-0.03490	0.99939
750	102	-0.20791	0.97815
750	86	0.06976	0.99756
750	110	-0.34202	0.93969
1500	32	0.84805	0.52992
1200	156	-0.91355	0.40674
1050	100	-0.17365	0.98481
1500	120	-0.50000	0.86603

ZONE # 6 (Barakars)

2250	50	0.64279	0.76604
750	114	-0.40674	0.91355
750	108	-0.30902	0.95106
1200	8	0.99027	0.13917
600	8	0.99027	0.13917
1050	24	0.91355	0.40674
900	102	-0.20791	0.97815

450	102	-0.20791	0.97815
1350	137	-0.73135	0.68200
450	137	-0.73135	0.68200
1050	137	-0.73135	0.68200
1050	106	-0.27564	0.96126
900	6	0.99452	0.10453
600	140	-0.76604	0.64279
600	10	0.98481	0.17365
900	40	0.76604	0.64279
600	22	0.92718	0.37461

ZONE # 7 (Barakars)

1050	84	0.10453	0.99452
600	22	0.92718	0.37461
300	20	0.93969	0.34202

ZONE # 8 (Barakars)

300	58	0.52992	0.84805
450	58	0.52992	0.84805
450	58	0.52992	0.84805
600	58	0.52992	0.84805
1050	100	-0.17365	0.98481
900	100	-0.17365	0.98481
1500	98	-0.13917	0.99027
1050	120	-0.50000	0.86603
600	142	-0.78801	0.61566
450	142	-0.78801	0.61566
1500	24	0.91355	0.40674
600	155	-0.90631	0.42262
450	140	-0.76604	0.64279

ZONE # 9 (Barakars)

750	58	0.52992	0.84805
1200	58	0.52992	0.84805
1350	2	0.99939	0.03490
600	128	-0.61566	0.78801
750	128	-0.61566	0.78801
1200	90	0.00000	1.00000
900	91	-0.01745	0.99985
1800	90	0.00000	1.00000
750	98	-0.13917	0.99027
1200	110	-0.34202	0.93969
1200	120	-0.50000	0.86603
750	46	0.69466	0.71934
750	46	0.69466	0.71934
600	118	-0.46947	0.88295
750	42	0.74315	0.66913
600	6	0.99452	0.10453

900	162	-0.95106	0.30902
-----	-----	----------	---------

ZONE #10 (Barakars)			
750	142	-0.78801	0.61566
750	142	-0.78801	0.61566
1200	142	-0.78801	0.61566
900	152	-0.88295	0.46947
1200	152	-0.88295	0.46947
600	138	-0.74314	0.66913
1050	95	-0.08716	0.99620
600	94	-0.06976	0.99756
1050	94	-0.06976	0.99756
1050	152	-0.88295	0.46947
1050	142	-0.78801	0.61566
1800	122	-0.52992	0.84805
1050	90	0.00000	1.00000
750	90	0.00000	1.00000
1200	128	-0.61566	0.78801
1200	152	-0.88295	0.46947
900	110	-0.34202	0.93969
900	155	-0.90631	0.42262

ZONE # 11 (Barakars)			
450	47	0.68200	0.73135
750	47	0.68200	0.73135
900	121	-0.51504	0.85717
900	138	-0.74314	0.66913
900	38	0.78801	0.61566
450	38	0.78801	0.61566
600	38	0.78801	0.61566
750	90	0.00000	1.00000
450	10	0.98481	0.17365
750	10	0.98481	0.17365

ZONE #12 (Barakars)			
450	36	0.80902	0.58779
300	36	0.80902	0.58779
600	26	0.89879	0.43837
600	26	0.89879	0.43837
300	26	0.89879	0.43837
300	26	0.89879	0.43837
600	100	-0.17365	0.98481
900	100	-0.17365	0.98481
2100	152	-0.88295	0.46947
450	152	-0.88295	0.46947
1200	114	-0.40674	0.91355
900	20	0.93969	0.34202
1800	20	0.93969	0.34202

600	20	0.93969	0.34202
600	14	0.97030	0.24192
450	14	0.97030	0.24192
450	14	0.97030	0.24192
300	14	0.97030	0.24192
1200	166	-0.97030	0.24192
600	106	-0.27564	0.96126
1050	94	-0.06976	0.99756
1800	160	-0.93969	0.34202
1050	0	1.00000	0.00000
300	0	1.00000	0.00000
450	8	0.99027	0.13917
900	38	0.78801	0.61566
600	38	0.78801	0.61566
1500	10	0.98481	0.17365
600	10	0.98481	0.17365
1650	16	0.96126	0.27564
600	100	-0.17365	0.98481

Table A-2 : Statistical details of lineaments extracted using Digitedge Scheme

Precambrian Formations

ZONE # 1 (Slate and Phyllite)			
length (m)	angle (θ) ^o	cos θ	sin θ
600	109	-0.32557	0.94552
900	109	-0.32557	0.94552
300	109	-0.32557	0.94552
300	109	-0.32557	0.94552
450	109	-0.32557	0.94552
450	109	-0.32557	0.94552
750	104	-0.24192	0.97030
2100	114	-0.40674	0.91355
300	114	-0.40674	0.91355
2700	109	-0.32557	0.94552
900	109	-0.32557	0.94552
600	79	0.19081	0.98163
900	80	0.17365	0.98481
1350	104	-0.24192	0.97030
1650	104	-0.24192	0.97030
450	104	-0.24192	0.97030
2400	106	-0.27564	0.96126
450	106	-0.27564	0.96126
750	101	-0.19081	0.98163
450	101	-0.19081	0.98163
900	101	-0.19081	0.98163
1050	101	-0.19081	0.98163
1200	101	-0.19081	0.98163
1200	101	-0.19081	0.98163
1500	101	-0.19081	0.98163
1200	120	-0.50000	0.86603
1050	130	-0.64279	0.76604
600	130	-0.64279	0.76604
750	130	-0.64279	0.76604
750	130	-0.64279	0.76604
750	130	-0.64279	0.76604
450	130	-0.64279	0.76604
1200	90	0.00000	1.00000
600	90	0.00000	1.00000
1350	90	0.00000	1.00000
750	89	0.01745	0.99985
750	89	0.01745	0.99985
750	89	0.01745	0.99985
1050	89	0.01745	0.99985
600	90	0.00000	1.00000
1200	150	-0.86603	0.50000

900	118	-0.46947	0.88295
900	122	-0.52992	0.84805
600	122	-0.52992	0.84805
900	82	0.13917	0.99027
750	156	-0.91355	0.40674
1500	100	-0.17365	0.98481
1200	100	-0.17365	0.98481
600	99	-0.15643	0.98769
750	99	-0.15643	0.98769
750	99	-0.15643	0.98769
1200	99	-0.15643	0.98769

ZONE # 2 (Gneisses)

900	90	0.00000	1.00000
1350	91	-0.01745	0.99985
1050	98	-0.13917	0.99027
1200	142	-0.78801	0.61566
750	144	-0.80902	0.58779
600	140	-0.76604	0.64279
750	70	0.34202	0.93969

ZONE # 3 (Boundary fault)

2250	94	-0.06976	0.99756
600	89	0.01745	0.99985
1350	90	0.00000	1.00000
900	90	0.00000	1.00000
750	90	0.00000	1.00000
900	98	-0.13917	0.99027
1500	98	-0.13917	0.99027

Gondwana Formations

ZONE # 4 Raniganj Formations			
1350	114	-0.40674	0.91355
600	48	0.66913	0.74314
600	50	0.64279	0.76604
450	30	0.86603	0.50000
300	30	0.86603	0.50000
450	30	0.86603	0.50000
450	30	0.86603	0.50000
600	26	0.89879	0.43837
600	26	0.89879	0.43837
600	50	0.64279	0.76604
600	40	0.76604	0.64279
600	30	0.86603	0.50000
300	30	0.86603	0.50000
900	159	-0.93358	0.35837
300	159	-0.93358	0.35837
450	20	0.93969	0.34202
600	56	0.55919	0.82904
300	86	0.06976	0.99756
ZONE # 6 (Barakars)			
1200	120	-0.50000	0.86603
1350	124	-0.55919	0.82904
1200	166	-0.97030	0.24192
1200	128	-0.61566	0.78801
750	170	-0.98481	0.17365
600	146	-0.82904	0.55919
900	12	0.97815	0.20791
900	46	0.69466	0.71934
450	54	0.58779	0.80902
600	108	-0.30902	0.95106
450	108	-0.30902	0.95106
1500	106	-0.27564	0.96126
450	106	-0.27564	0.96126
450	74	0.27564	0.96126
750	74	0.27564	0.96126
1800	69	0.35837	0.93358
450	46	0.69466	0.71934
750	46	0.69466	0.71934
450	89	0.01745	0.99985
450	90	0.00000	1.00000
ZONE # 7 (Barakars)			
900	134	-0.69466	0.71934
900	134	-0.69466	0.71934

600	120	-0.50000	0.86603
450	110	-0.34202	0.93969

ZONE # 8 (Barakars)

600	56	0.55919	0.82904
600	50	0.64279	0.76604
1050	122	-0.52992	0.84805
900	66	0.40674	0.91355
750	154	-0.89879	0.43837
900	126	-0.58778	0.80902
600	126	-0.58778	0.80902
450	98	-0.13917	0.99027
450	58	0.52992	0.84805
750	106	-0.27564	0.96126

ZONE # 9 (Barakars)

600	86	0.06976	0.99756
750	86	0.06976	0.99756
450	58	0.52992	0.84805
1050	68	0.37461	0.92718
1500	54	0.58779	0.80902
600	59	0.51504	0.85717
750	59	0.51504	0.85717
900	59	0.51504	0.85717
1200	110	-0.34202	0.93969
750	116	-0.43837	0.89879
450	114	-0.40674	0.91355
600	14	0.97030	0.24192
450	56	0.55919	0.82904
750	88	0.03490	0.99939

ZONE #10 (Barakars)

600	132	-0.66913	0.74315
1500	150	-0.86603	0.50000
750	150	-0.86603	0.50000
750	44	0.71934	0.69466
900	42	0.74314	0.66913
600	42	0.74314	0.66913
900	42	0.74314	0.66913
900	24	0.91355	0.40674
750	14	0.97030	0.24192
750	132	-0.66913	0.74315
750	86	0.06976	0.99756
450	86	0.06976	0.99756
300	86	0.06976	0.99756
600	112	-0.37461	0.92718
600	150	-0.86603	0.50000
1500	130	-0.64279	0.76604

ZONE # 11 (Barakars)			
1200	144	-0.80902	0.58779
750	134	-0.69466	0.71934
900	20	0.93969	0.34202
450	10	0.98481	0.17365
450	96	-0.10453	0.99452
450	12	0.97815	0.20791
450	60	0.50000	0.86603

ZONE # 12 (Barakars)			
900	138	-0.74314	0.66913
300	138	-0.74314	0.66913
300	138	-0.74314	0.66913
600	135	-0.70711	0.70711
600	104	-0.24192	0.97030
600	104	-0.24192	0.97030
600	76	0.24192	0.97030
450	82	0.13917	0.99027
600	102	-0.20791	0.97815
900	148	-0.84805	0.52992
600	148	-0.84805	0.52992
600	166	-0.97030	0.24192
750	168	-0.97815	0.20791
450	168	-0.97815	0.20791
1350	178	-0.99939	0.03490
900	6	0.99452	0.10453
1950	174	-0.99452	0.10453
1200	118	-0.46947	0.88295
900	120	-0.50000	0.86603
600	120	-0.50000	0.86603
450	80	0.17365	0.98481
600	24	0.91355	0.40674